

Merger rate density of Population III binary black holes below, above, and in the pair-instability mass gap

ATARU TANIKAWA,¹ HAJIME SUSU,² TAKASHI YOSHIDA,³ ALESSANDRO A. TRANI,¹ AND TOMOYA KINUGAWA⁴

¹*Department of Earth Science and Astronomy, College of Arts and Sciences, The University of Tokyo, 3-8-1 Komaba, Meguro-ku, Tokyo 153-8902, Japan*

²*Department of Physics, Konan University, Kobe, Japan*

³*Department of Astronomy, Graduate School of Science, The University of Tokyo, Bunkyo-ku, Tokyo, Japan*

⁴*Institute for Cosmic Ray Research, The University of Tokyo, Kashiwa, Chiba*

ABSTRACT

We present the merger rate density of Population (Pop.) III binary black holes (BHs) by means of a widely-used binary population synthesis code **BSE** with extensions to very massive and extreme metal-poor stars. We consider not only low-mass BHs (lBHs: $5 - 50M_{\odot}$) but also high-mass BHs (hBHs: $130 - 200M_{\odot}$), where lBHs and hBHs are below and above the pair-instability mass gap ($50 - 130M_{\odot}$), respectively. Pop. III BH-BHs can be categorized into three subpopulations: BH-BHs without hBHs (hBH0s: $m_{\text{tot}} \lesssim 100M_{\odot}$), with one hBH (hBH1s: $m_{\text{tot}} \sim 130 - 260M_{\odot}$), and with two hBHs (hBH2s: $m_{\text{tot}} \sim 270 - 400M_{\odot}$), where m_{tot} is the total mass of a BH-BH. Their merger rate densities at the current universe are $\sim 0.1 \text{ yr}^{-1} \text{ Gpc}^{-3}$ for hBH0s, and $\sim 0.01 \text{ yr}^{-1} \text{ Gpc}^{-3}$ for the sum of hBH1s and hBH2s, provided that the mass density of Pop. III stars is $\sim 10^{13}M_{\odot} \text{ Gpc}^{-3}$. These rates are modestly insensitive to initial conditions and single star models. The hBH1 and hBH2 mergers can dominate BH-BHs with hBHs discovered in near future. They have low effective spins $\lesssim 0.2$ in the current universe. The number ratio of the hBH2s to the hBH1s is high, $\gtrsim 0.1$. We also find BHs in the mass gap (up to $\sim 85M_{\odot}$) merge. These merger rates can be reduced to nearly zero if Pop. III binaries are always wide ($\gtrsim 100R_{\odot}$), and if Pop. III stars always enter into chemically homogeneous evolution. The presence of close Pop. III binaries ($\sim 10R_{\odot}$) are crucial for avoiding the worst scenario.

Keywords: stars: binaries: close – stars: black holes – stars: Population III – gravitational waves

1. INTRODUCTION

In 2015, gravitational wave (GW) observatories, LIGO, have first detected GWs, and the GWs have come from a merger of two black holes (BHs) (Abbott et al. 2016). Since then, GW observatories, LIGO and Virgo, have continuously discovered a large number of BH-BH mergers, and have published ~ 50 BH-BH mergers with detail information, such as their masses, distances, spin magnitudes, and spin-orbit misalignments as of December 2020 (Abbott et al. 2019, 2020a,c,b,d; The LIGO Scientific Collaboration et al. 2020). Moreover, research groups other than the LIGO-Virgo collaboration have found other BH-BHs (Zackay et al. 2019; Venumadhav et al. 2020). Many of them contain BHs with $\sim 30M_{\odot}$, significantly more massive than BHs in X-ray binaries discovered previously, $\lesssim 15M_{\odot}$ (e.g. Casares et al.

2017). Thus, the origin(s) of merging BH-BHs have been controversial.

Many formation scenarios of merging BH-BHs have been currently suggested. Population (Pop.) I/II binaries evolve to merging BH-BHs through common envelope evolution (Bethe & Brown 1998; Belczynski et al. 2002, 2014, 2016a, 2020a; Dominik et al. 2012, 2013; Mennekens & Vanbeveren 2014; Spera et al. 2015, 2019; Eldridge & Stanway 2016; Eldridge et al. 2017, 2019; Mapelli et al. 2017; Mapelli & Giacobbo 2018; Mapelli et al. 2019; Stevenson et al. 2017; Giacobbo & Mapelli 2018; Kruckow et al. 2018). Close binaries can also form merging BH-BHs through chemically homogeneous evolution (CHE) (de Mink et al. 2009; Mandel & de Mink 2016; Marchant et al. 2016; du Buisson et al. 2020; Riley et al. 2020; Hong et al. 2020). Dynamical interactions in globular clusters (GCs) raise merging BH-BHs (Portegies Zwart & McMillan 2000; Downing et al. 2010; Tanikawa 2013; Rodriguez et al. 2016a; Bae et al. 2014; Rodriguez et al. 2016b, 2018b,a; Fujii et al. 2017; Askar

et al. 2017; Park et al. 2017; Samsing & Ramirez-Ruiz 2017; Samsing 2018; Samsing et al. 2018; Hong et al. 2018). In open clusters, merging BH-BHs are formed by combination of common envelope evolution and dynamical interactions (Ziosi et al. 2014; Mapelli 2016; Banerjee 2017, 2018a,b; Kumamoto et al. 2019, 2020; Di Carlo et al. 2019, 2020a,b; Rastello et al. 2019). Dynamical interactions can form merging BH-BHs also in galactic centers (O’Leary et al. 2009; Antonini & Perets 2012; VanLandingham et al. 2016; Antonini & Rasio 2016; Bartos et al. 2017; Petrovich & Antonini 2017; Stone et al. 2017; Hoang et al. 2018; Hamers et al. 2018; McKernan et al. 2018; Leigh et al. 2018; Yang et al. 2019; Rasskazov & Kocsis 2019; Trani et al. 2019; Tagawa et al. 2020b,a; McKernan et al. 2020; Arca Sedda 2020; Mapelli et al. 2020). Merging BH-BHs can emerge through secular evolution in stable triple systems (TSs), and quadruple systems (QSs) (Antonini et al. 2014; Silsbee & Tremaine 2017; Antonini et al. 2017; Rodriguez & Antonini 2018; Liu & Lai 2019; Fragione & Kocsis 2019; Hamers & Safarzadeh 2020; Fragione et al. 2020). Although merging BH-BHs originate from astrophysical objects in the above scenarios, even primordial BHs, made from dark matter, can generate merging BH-BHs (Sasaki et al. 2016).

Pop. III binary stars, which are formed from primordial gas at the high-redshift universe, can also raise merging BH-BHs. The typical BH mass is $\sim 30M_{\odot}$, larger than Pop. I/II BH-BHs (Kinugawa et al. 2014). This is not because Pop. III stars have a top-heavy initial mass function (IMF), but because Pop. III binaries tend to experience stable mass transfer owing to their radiative envelopes (Kinugawa et al. 2016a; Inayoshi et al. 2017). This argument is also robust against uncertainties of binary evolutions, such as efficiencies of mass transfer, mass accretion, common envelope, and tidal interaction (Kinugawa et al. 2020a). Since the typical BH mass is consistent with observed BH-BH masses, Pop. III binaries can be one of their promising origins.

It is uncertain whether Pop. III BH-BHs are a dominant origin of observed BH-BHs (Hartwig et al. 2016; Belczynski et al. 2017; Kinugawa et al. 2020a). Moreover, observed BH-BHs may be mainly formed through dynamical interactions (Callister et al. 2020). However, even if Pop. III BH-BHs are not dominant, it should be worth while to identify Pop. III BH-BHs from observed BH-BHs. Pop. III stars are key ingredients of the cosmic dawn, the reionization of the universe, the beginning of stellar nucleosynthesis, and so on. Despite of their importance, Pop. III stars are not directly observed (Rydberg et al. 2013). Since Pop. III stars are typically massive stars, $10 - 1000M_{\odot}$ (Omukai & Nishi 1998; Abel

et al. 2002; Bromm & Larson 2004; Yoshida et al. 2008; Hosokawa et al. 2011; Stacy et al. 2011, 2012; Bromm 2013; Susa 2013; Susa et al. 2014; Hirano et al. 2015), they are short-lived, and located at the high-redshift universe. They can be observed only by ultimately large telescopes (e.g. Schauer et al. 2020). Although some of Pop. III stars can be formed as low-mass and long-lived stars (Nakamura & Umemura 2001; Machida et al. 2008; Clark et al. 2011a,b; Greif et al. 2011, 2012; Machida & Doi 2013; Susa et al. 2014; Chiaki et al. 2016), they have not yet been observed (Frebel & Norris 2015; Magg et al. 2018, 2019). Although extreme metal-poor (EMP) stars might be Pop. III stars metal-polluted by accreting interstellar medium (Komiya et al. 2015), many studies have suggested EMP stars are not polluted Pop. III stars, since such accretion can be blocked by stellar winds of low-mass Pop. III stars (Tanaka et al. 2017; Suzuki 2018). Interstellar asteroids cannot pollute Pop. III stars up to EMP stars (Tanikawa et al. 2018; Kirihaara et al. 2019).

In this paper, we predict properties of Pop. III BH-BHs to identify them from BH-BHs observed by current and future GW observatories. Although the current GW observatories can observe BH-BHs within redshift (z) of $\lesssim 1$, future ground-based GW observatories, such as Einstein telescope (Punturo et al. 2010; Maggiore et al. 2020) and Cosmic explorer (Reitze et al. 2019), will detect BH-BHs up to $z \sim 10$. A future space-borne GW observatory LISA (Amaro-Seoane et al. 2017) is expected to catch Pop. III BH-BHs (e.g. Sesana et al. 2009). Another space-borne GW observatory DECIGO (Kawamura et al. 2006) can follow the cosmic evolution of BH-BHs, and distinguish Pop. III BH-BHs (Nakamura et al. 2016).

So far, Kinugawa et al. (2014) have shown that Pop. III BH-BHs have typically $\sim 30M_{\odot}$, and Kinugawa et al. (2020a) have shown its robustness against binary star evolution models. In this paper, we focus on the dependence of Pop. III BH-BHs on initial conditions and single star evolution models. Previous studies have assumed that Pop. III binaries can have initial separations comparable to their stellar radii at their zero-age main-sequence (ZAMS) times. As well as this case, we also consider Pop. III binaries with the minimum separation of $\sim 100R_{\odot}$. Pop. III binaries may not be initially compact, since Pop. III stars can expand to $\gtrsim 100R_{\odot}$ at their protostellar phases (Stahler et al. 1986; Omukai & Palla 2001, 2003). Although previous studies have not taken into account stellar winds, we account for stellar winds, which are excited by stellar rotations (Yoon et al. 2012). Moreover, we set the maximum ZAMS mass to $300M_{\odot}$, while previous studies do to $150M_{\odot}$.

This maximum mass is reasonable according to recent numerical simulations (Susa et al. 2014; Hirano et al. 2014, 2015). Since such massive stars can overcome pair instability supernovae (PISNe) (Barkat et al. 1967; Fryer 1968; Bond et al. 1984; El Eid & Langer 1986; Fryer et al. 2001; Heger & Woosley 2002; Umeda & Nomoto 2002), we can get BHs with $\gtrsim 100M_{\odot}$. Eventually, we show properties of Pop. III BH-BHs with several 10 and $100M_{\odot}$, and discuss how to identify them from other BH-BHs by current and future GW observatories.

Belczynski et al. (2004) have investigated the formation of BH-BHs from Pop. III stars with $100 - 500M_{\odot}$. Due to the IMF, they have not investigated a BH-BH consisting of a BH overcoming PISN, and a BH not overcoming PISN. Moreover, studies of Pop. III stars have rapidly developed in this decade (see Dayal & Ferrara 2018, for review). We can reflect these achievements. Liu & Bromm (2020a) and Liu et al. (2020a) have studied Pop. III BH-BHs formed by dynamical interactions. On the other hand, we focus on Pop. III BH-BHs formed through binary evolution. These studies should be complementary.

The structure of this paper is as follows. In section 2, we describe our method. In section 3, we show the calculation results. In section 4, we consider how to identify Pop. III BH-BHs from other BH-BHs observed by current and future GW observatories. In section 5, we discuss about effects we do not examine in section 3. In section 6, we summarize this paper.

2. METHOD

We perform calculations of binary population synthesis by means of the BSE code (Hurley et al. 2000, 2002) with extensions to very massive and EMP stars including Pop. III stars. In sections 2.1 and 2.2, we present single and binary star models in our BSE code, respectively. In section 2.3, we show our initial conditions of binaries. In section 2.4, we describe parameter sets of our calculation runs. In section 2.5, we give our Pop. III formation model to derive the merger rate of Pop. III BH-BHs.

2.1. Single star model

We use fitting formulae for stars with stellar metallicity $Z = 10^{-8}Z_{\odot}$ incorporated into BSE (Tanikawa et al. 2020c). The fitting formulae are based on simulation results of $Z = 10^{-8}Z_{\odot}$ stars from $8M_{\odot}$ to $1280M_{\odot}$ by means of the HOSHI code (Takahashi et al. 2016, 2018, 2019; Yoshida et al. 2019). They consist of luminosity (L), radius (R), helium (He) core mass ($M_{c,\text{He}}$), and carbon-oxygen (CO) core mass ($M_{c,\text{CO}}$) as functions of time and stellar mass (M). They follow stel-

lar evolutions from the ZAMS time to the carbon ignition time during which stars experience main-sequence (MS), core He-burning (CHeB), and shell He-burning (ShHeB) phases. If stars lose their hydrogen (H) envelopes through stellar wind mass loss and binary interactions, we adopt fitting formulae of naked He (nHe) stars derived in Hurley et al. (2000) for their luminosities, and set $R = 0.2239(M_{c,\text{He}}/M_{\odot})^{0.62}R_{\odot}$ for their radii (Tout et al. 1997). Figure 1 shows Hertzsprung-Russell diagram of $10^{-8}Z_{\odot}$ stars with $M = 10 - 1280M_{\odot}$ at intervals of $2^{1/2}$, where we do not account for stellar winds. Stars with $10 \lesssim M/M_{\odot} \lesssim 50$ end their lives with blue-supergiant (BSG) stars with temperature of $\gtrsim 10^{3.65}$ K. Stars with $50 \lesssim M/M_{\odot} \lesssim 640$ become red-supergiant (RSG) stars when they are in their CHeB/ShHeB (or post-MS) phases. Stars with $M/M_{\odot} \gtrsim 640$ are still in their MS phases, when they become RSG stars.

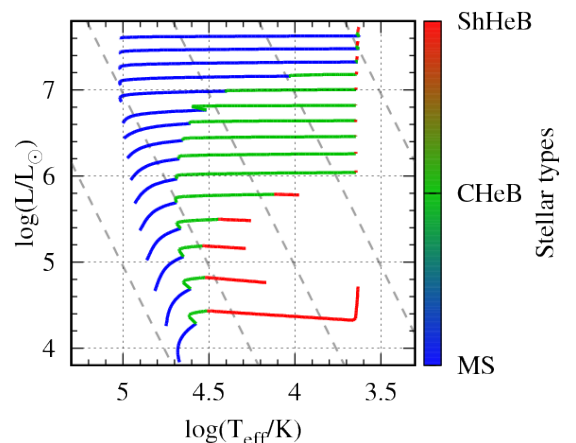


Figure 1. Hertzsprung-Russell diagram of $10^{-8}Z_{\odot}$ stars with $M = 10 - 1280M_{\odot}$ at intervals of $2^{1/2}$ from bottom to top. Stellar winds are not taken into account. Gray dashed lines indicate stellar radii of 1, 10, 10^2 , 10^3 , and 10^4R_{\odot} from left to right. Colors indicate stellar phases: MS (blue), CHeB (green), and ShHeB (red).

Tanikawa et al. (2020c) have devised the fitting formulae of stars with $M \leq 160M_{\odot}$, and have compared the fitting formulae with detail simulation results obtained by the HOSHI code. Here, we make similar comparisons for $M/M_{\odot} = 320, 640$, and 1280 in Figure 2. The luminosities and He core masses are in good agreement with each other. The He core masses of the fitting formulae grow later than those of the simulation results. This is because we assume the He core masses are zero when stars are in their MS phases. The radii of the fitting formulae deviate from those of the simulation results in the middle of the evolution. However, these deviations should have small effects on binary evolutions, since the

minimum and maximum radii for each MS, CHeB and ShHeB phase are consistent with each other. In particular, it is important that the maximum radii of stars (i.e. the maximum radii of ShHeB phases) are consistent between the fitting formulae and simulation results. The maximum radii decide whether binary stars interact with each other, or not.

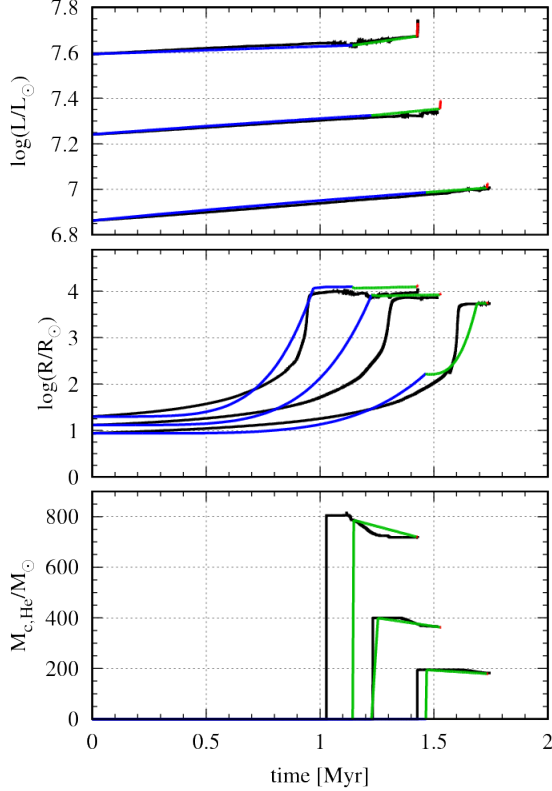


Figure 2. Time evolution of luminosities, radii, and He core masses for stars with $M = 320, 640$, and $1280 M_{\odot}$. Black curves indicate data of detail simulations, and colored curves indicate our fitting formulae. The color codes are the same as in Figure 1. More massive stars have larger values for all the quantities.

We take into account stellar wind mass loss in a post-processing way. The wind model is based on Belczynski et al. (2010) with modification of luminous-blue-variable (LBV) wind, and enhancement through stellar rotations. For no rotating stars, the stellar wind mass loss is expressed as

$$\dot{M}_{\text{wind}} = \begin{cases} \max(\dot{M}_{\text{NJ}}, \dot{M}_{\text{OB}}) & (\text{MS}) \\ \max(\dot{M}_{\text{NJ}}, \dot{M}_{\text{OB}}, \dot{M}_{\text{R}}, \dot{M}_{\text{WR}}, \dot{M}_{\text{LBV}}) & (\text{CHeB}) \\ \max(\dot{M}_{\text{NJ}}, \dot{M}_{\text{OB}}, \dot{M}_{\text{R}}, \dot{M}_{\text{WR}}, \dot{M}_{\text{LBV}}, \dot{M}_{\text{VW}}) & (\text{ShHeB}) \\ \max(\dot{M}_{\text{R}}, \dot{M}_{\text{WR}}) & (\text{nHe}) \end{cases}, \quad (1)$$

where $\dot{M}_{\text{NJ}}, \dot{M}_{\text{OB}}, \dot{M}_{\text{R}}, \dot{M}_{\text{WR}}, \dot{M}_{\text{LBV}}$, and \dot{M}_{VW} are mass loss of luminous stars (Nieuwenhuijzen & de Jager 1990; Kudritzki et al. 1989), hot massive H-rich stars (Vink et al. 2001), giant-branch stars (Kudritzki & Reimers 1978; Iben & Renzini 1983), Wolf-Rayet stars (Hamann & Koesterke 1998; Vink & de Koter 2005), LBV stars (Humphreys & Davidson 1994), and asymptotic giant branch (AGB) stars (Vassiliadis & Wood 1993). The expressions of $\dot{M}_{\text{NJ}}, \dot{M}_{\text{OB}}, \dot{M}_{\text{R}}, \dot{M}_{\text{WR}}$, and \dot{M}_{VW} are the same as Eqs. (56), (57), (58), (59), and (61) in Tanikawa et al. (2020c). We modify the expression of \dot{M}_{LBV} as

$$\frac{\dot{M}_{\text{LBV}}}{M_{\odot} \text{ yr}^{-1}} = \begin{cases} 1.5 \times 10^{-4} (Z/Z_{\odot})^{0.86} & (L > 6 \times 10^5 L_{\odot}, \text{ and } x_{\text{LBV}} > 1) \\ 0 & (\text{otherwise}), \end{cases}, \quad (2)$$

where $x_{\text{LBV}} = 10^{-5} (R/R_{\odot}) (L/L_{\odot})^{0.5}$. The expression is the same as Belczynski et al. (2010) except for the metallicity dependence, and the metallicity dependence is the same as MOBSE2 (Giacobbo et al. 2018).

The stellar wind can be enhanced by stellar rotation. We include the enhancement as follows:

$$\dot{M}_{\text{wind,rot}} = \min \left[\dot{M}_{\text{wind}} (1 - v_{\text{rot}}/v_{\text{crit}})^{-0.43}, 0.1 M/t_{\text{KH}} \right] \quad (3)$$

$$v_{\text{crit}} = \sqrt{GM(1 - L/L_{\text{Edd}})/R} \quad (4)$$

(Yoon et al. 2010, 2012; Takahashi et al. 2018), where G , v_{rot} , t_{KH} , and L_{Edd} are the gravitational constant, the stellar surface rotation velocity, Kelvin-Helmholtz timescale, and Eddington luminosity, respectively. We adopt $L_{\text{Edd}} = 3.7 \times 10^4 (M/M_{\odot}) L_{\odot}$ for stars in MS, CHeB, and ShHeB phases. We put an upper limit on L for nHe stars, such that $L \leq 0.99 L_{\text{Edd}}$, where we adopt $L_{\text{Edd}} = 6.3 \times 10^4 (M/M_{\odot}) L_{\odot}$ for nHe stars. Note that L_{Edd} of nHe stars is larger than those of MS, CHeB, and ShHeB stars due to smaller opacity of electron scattering.

We put such an upper limit on luminosities of nHe stars for the following reason. We infer luminosity of nHe stars from our fitting formulae of ShHeB stars. Since a ShHeB star with $M = 320 M_{\odot}$ has a He core with $180 M_{\odot}$, and its luminosity is at most $10^7 L_{\odot}$ (see Figure 2), a nHe star with $180 M_{\odot}$ should have luminosity of $10^7 L_{\odot}$. Thus, this nHe star should not exceed the Eddington luminosity of nHe stars. When we apply this inference to stars with various M , we find that nHe stars with $\lesssim 300 M_{\odot}$ do not exceed the Eddington luminosity according to our fitting formulae. We have confirmed this inference by performing simulations of non-rotating

nHe stars with 50, 100, 200, and $320M_\odot$ and a $200M_\odot$ star with the initial rotating velocity of $0.1v_k$, where $v_k = \sqrt{GM/R}$ is the Kepler velocity, with the HOSHI code. These stars do not exceed their Eddington limits, and lose little mass through rotationally enhanced stellar winds. On the other hand, the fitting formulae of nHe stars in Hurley et al. (2000) are made from nHe star models with $M = 0.32 - 10M_\odot$, and nHe stars with $\gtrsim 100M_\odot$ exceed their Eddington luminosity. If we adopt this luminosity, we overestimate the rotationally enhanced mass loss. Hence, we constrain luminosity of nHe stars, such that $L \leq 0.99L_{\text{Edd}}$.

Stars are assumed to experience supernovae or direct collapse immediately after the carbon ignition, and leave stellar remnants like NSs and BHs, or no remnants. We adopt the rapid model in Fryer et al. (2012) modified by pulsational pair instability (PPI) (Heger & Woosley 2002; Woosley et al. 2007; Yoshida et al. 2016; Woosley 2017; Leung et al. 2019) and pair instability supernovae (PISNe) (Barkat et al. 1967; Fraley 1968; Bond et al. 1984; El Eid & Langer 1986; Fryer et al. 2001; Heger & Woosley 2002; Umeda & Nomoto 2002). Then, stellar remnant masses can be written as

$$M_{\text{rem}} = \begin{cases} M_{\text{rapid}} & (M_{\text{c,He}} \leq M_{\text{c,He,PPI}}) \\ M_{\text{c,He,PPI}} & (M_{\text{c,He,PPI}} < M_{\text{c,He}} \leq M_{\text{c,He,PISN}}) \\ 0 & (M_{\text{c,He,PISN}} < M_{\text{c,He}} \leq M_{\text{c,He,DC}}) \\ M_{\text{rapid}} & (M_{\text{c,He}} > M_{\text{c,He,DC}}) \end{cases}, \quad (5)$$

and

$$\frac{M_{\text{rapid}}}{M_\odot} = \begin{cases} 1.2 & (M_{\text{c,CO}}/M_\odot \leq 2.5) \\ 0.286M_{\text{c,CO}} + 0.486 & (2.5 < M_{\text{c,CO}}/M_\odot \leq 6) \\ M_t & (6 < M_{\text{c,CO}}/M_\odot \leq 7) \\ M_t - M_{\text{ej}} & (7 < M_{\text{c,CO}}/M_\odot \leq 11) \\ M_t & (M_{\text{c,CO}}/M_\odot > 11) \end{cases} \quad (6)$$

$$\frac{M_{\text{ej}}}{M_\odot} = [0.25(M_t - 1) - 1.275](11 - M_{\text{c,CO}}). \quad (7)$$

Here, Eq. (5) indicates PPI/PISN corrections. The PPI/PISN corrections consist of four regimes: core-collapse supernovae (or direct collapse), PPI, PISNe, and direct collapse in the ascending order of He core mass. We adopt the boundaries of these regimes, such that the minimum He core mass of PPI ($M_{\text{c,He,PPI}} = 45M_\odot$), the minimum He core mass of PISN ($M_{\text{c,He,PISN}} =$

$65M_\odot$), and the minimum He core mass of direct collapse ($M_{\text{c,He,DC}} = 135M_\odot$) in the same way as Belczynski et al. (2016b). We assume stars undergoing PPI leave BHs with masses of $M_{\text{c,He,PPI}}$. Eqs. (6) and (7) show the rapid model, where M_t is the total stellar mass. We regard stellar remnants as NSs and BHs if their masses are below and above $3M_\odot$, respectively. The lower mass limit of NSs is defined to be $1.2M_\odot$. If a stellar remnant has its mass of $< 1.2M_\odot$, it is a white dwarf, however such a stellar remnant does not appear in this paper.

We account for a natal kick when massive stars leave NSs and BHs. The natal kicks are randomly oriented, and have Maxwellian velocity distribution with σ_k . We assume that σ_k does not depend on the remnant mass, contrary to the often used prescription which attributes to higher mass remnant a lower kick velocity. In this paper, NSs and BHs acquire the same kick as motivated in section 2.4.

We model BH spins as follows. BH progenitors get and lose their spin angular momenta through single and binary evolutions, such as stellar winds, wind accretion, tidal interactions, Roche lobe overflow, and so on. Then, the spin vectors are always parallel to the binary orbit vectors. BH progenitors keep their spin angular momenta when they become BHs, except that they experience PPI. If BH progenitors experience PPI, we force the spins of their remnants to be zero, since these progenitors lose large amounts of masses. Frequently, the BH progenitors have spin angular momenta larger than those of extreme Kerr BHs. In this case, we force the spin parameters of their remnants to be unity, and assume that the BH masses are equal to their progenitor masses. Although BHs can get spin angular momenta through mass transfer, we do not account for this process. In summary, we can express a normalized BH spin vector as follows:

$$\vec{\chi} = \begin{cases} \vec{0} & \text{if PPI} \\ \min(|\vec{S}|/(GM^2/c), 1) \vec{L}/|\vec{L}| & \text{otherwise} \end{cases}, \quad (8)$$

where c is the speed of light, \vec{S} is the spin angular momentum of a BH progenitor just before its collapse, and \vec{L} is the binary orbit vector. Natal kicks can tilt $\vec{\chi}$ from \vec{L} as described in section 2.2.

2.2. Binary star model

Since we use the BSE code, our binary star model is basically similar to that of Hurley et al. (2002) with some modifications. In this section, we briefly describe our binary star model.

Before describing our binary star model, we define names of binary members. We call the heavier and lighter stars at their ZAMS times “1st-evolving star” and “2nd-evolving star”, respectively, since the former evolves earlier than the latter. We attach subscripts of 1 and 2 with quantities indicating 1st- and 2nd-evolving stars, respectively. For example, masses of 1st- and 2nd-evolving stars are m_1 and m_2 . We define the 1st and 2nd BHs as BHs which the 1st- and 2nd-evolving stars leave, respectively. The 1st BH is not always heavier than the 2nd BH. We call the heavier and lighter BHs “primary BH” and “secondary BH”, respectively. We attach subscripts of “p” and “s” with quantities indicating primary and secondary BHs. Thus, masses of primary and secondary BHs are $m_{b,p}$ and $m_{b,s}$, respectively.

We take into account wind accretion through which a star gets mass outflowing from its companion through stellar winds. In the original BSE code, the accretion rate is estimated as a Bondi-Hoyle mechanism (Bondi & Hoyle 1944) with an upper limit of a fraction of the mass loss rate of the stellar winds. We find that the accretion rate sometimes exceeds the Eddington limit due to the presence of massive stellar winds and massive BHs. Thus, we put an upper limit on the wind accretion rate, and set the limit to the Eddington limit expressed by Cameron & Mock (1967). Through stellar winds and wind accretion, stars lose and gain their spin angular momenta, and binaries change their semi-major axes and eccentricities. Our treatment for these processes is the same as that of the original BSE code.

Our prescriptions for tidal evolution are the same as the original BSE code. We adopt the equilibrium tide with convective damping for stars with convective envelopes, and the dynamical tide with radiative damping for stars with radiative envelopes. However, the difference between the original BSE code and our binary star model is which post-MS stars (here, CHeB and ShHeB stars) have which types of envelopes. In the original BSE code, CHeB and ShHeB stars have radiative and convective envelopes, respectively, where ShHeB stars are called AGB stars in the original BSE code. In our binary model, stars with $\log(T_{\text{eff}}/\text{K}) \geq 3.65$ and < 3.65 have radiative and convective envelopes, respectively. We need the above treatment, since CHeB stars can have convective envelopes, and ShHeB stars can have radiative envelopes in our single star model.

We also treat mass transfer in the same way as the original BSE code. If mass transfer is stable, a binary experiences stable mass transfer (or stable Roche-lobe overflow), and otherwise common envelope evolution. Its stability strongly depends on whether a donor star has radiative or convective envelopes. If a donor star has

a radiative (convective) envelope, mass transfer tends to be stable (unstable). We determine which post-MS stars have which types of envelopes in the same way as the case of tidal evolution described above. The common envelope evolution is modeled as the α formalism (e.g. Webbink 1984). Thus, we have to decide the common envelope efficiency α_{CE} , and the structural binding energy parameter of a star λ_{CE} . We set $\alpha_{\text{CE}} = 1$ and $\lambda_{\text{CE}} = 1$, if unspecified.

We consider orbital decay through GW radiation in the same way as the original BSE code. On the other hand, we switch off magnetic braking. It is difficult to expect the B-field configuration of Pop III binaries. In the state-of-art Pop III formation simulation (Sharda et al. 2020), the dominant component of the magnetic field is tangled. In such a case, the effect of magnetic braking is weak, so we omit the process.

BH spin vectors can be misaligned to binary orbit vectors due to the natal kicks. We record angles between BH spin and binary orbit vectors, where the binary orbit vectors are the ones when BH-BHs are formed. The angle between the 2nd BH spin and binary orbit vectors (θ_2) can be decided only by the kick vector and binary parameters at the birth time. On the other hand, to determine the angle between the 1st BH spin and binary orbit vectors (θ_1), we need to know differences between binary phases at the birth times of the 1st and 2nd BHs. Although we can know them, we choose the differences by Monte Carlo technique. Since binary periods are generally much smaller than time intervals between the birth times, it is good approximation to choose the differences of phases randomly. Then, the angles θ_1 and θ_2 can be given by

$$\cos \theta_1 = \vec{\chi}_1 \cdot \vec{L} / |\vec{L}| \quad (9)$$

$$\cos \theta_2 = \vec{\chi}_2 \cdot \vec{L} / |\vec{L}|, \quad (10)$$

where the “ \cdot ” operator means the inner product, $\vec{\chi}_1$ and $\vec{\chi}_2$ are normalized BH spin vectors of the 1st and 2nd BHs, respectively, and \vec{L} is the binary orbit vector of the final BH-BHs. Note that \vec{L} can be obtained from the natal kick velocity of the 2nd BH and the binary parameter at its birth time as described above. We suppose the coordinate in which z -axis is parallel to the binary orbit vector just before the 2nd BH is born. Then, $\vec{\chi}_1$ and $\vec{\chi}_2$ can be written as

$$\vec{\chi}_1 = (\sin \theta'_1 \cos \phi'_1, \sin \theta'_1 \sin \phi'_1, \cos \theta'_1) \quad (11)$$

$$\vec{\chi}_2 = (0, 0, 1), \quad (12)$$

where θ'_1 is the angle between the 1st BH spin vector and binary orbit vector just before the 2nd BH is born, and ϕ'_1 is randomly chosen between 0 and 2π . The spin

vector of the 2nd BH should be parallel to the binary orbit vector just before its birth, since we do not account for spin-orbit misalignment mechanism other than natal kicks. Note that θ'_1 can be determined by the natal kick vector of the 1st BH and binary parameters at the birth time of the 1st BH.

2.3. Initial conditions

To generate a bunch of binaries, we set distribution of 1st-evolving star's masses ($m_{1,i}$), mass ratios of 2nd-evolving stars to 1st-evolving stars ($q_i = m_{2,i}/m_{1,i}$), semi-major axes (a_i), and eccentricities (e_i) at the initial time as follows. The distribution of $m_{1,i}$ is given by

$$f(m_{1,i}) \propto m_{1,i}^{-1} \quad (10 \leq m_{1,i}/M_\odot \leq 300). \quad (13)$$

This is based on logarithmically flat mass distribution of Pop. III stars in the range from about $10M_\odot$ to several $100M_\odot$ (Susa et al. 2014; Hirano et al. 2014, 2015). Note that although we set the maximum mass to $300M_\odot$, the maximum mass can be smaller (e.g. Tarumi et al. 2020).

We set the distribution of q_i , such that

$$f(q_i) \propto \text{const} \quad (q'_{\min} \leq q_i \leq 1) \quad (14)$$

$$q'_{\min} = \max(q_{\min}, 10M_\odot/m_{1,i}). \quad (15)$$

The second equation means the minimum 2nd-evolving star's mass is $10M_\odot$, the same as the minimum mass of 1st-evolving stars. We determine q_{\min} in section 2.4.

The average mass of binaries at the initial time, $\langle m_{\text{bin},i} \rangle$, can be calculated as

$$\begin{aligned} \frac{\langle m_{\text{bin},i} \rangle}{M_\odot} &= \int_{10}^{300} dm_{1,i} f(m_{1,i}) \int_{q_{\min}}^1 dq_i f(q_i) m_{1,i} (1 + q_i) \\ &\sim 43(3 + q_{\min}). \end{aligned} \quad (16)$$

The semi-major axis distribution can be written as

$$f(a_i) \propto a_i^{-1} \quad (a'_{\min} \leq a_i/R_\odot \leq 2000) \quad (17)$$

$$a'_{\min} = \max \left[a_{\min}, \frac{0.6q_i^{2/3} + \log(1 + q_i^{1/3})}{0.49q_i^{2/3}} R_{1,i}/R_\odot \right], \quad (18)$$

where $R_{1,i}$ is the initial radius of the 1st-evolving star. The maximum value $2000R_\odot$ can be obtained from the simulation results of Figure 5 in Arimoto et al. (2020) in preparation. The maximal final semi-major axis of the binaries at $\gtrsim 2 \times 10^4$ yr is ~ 10 AU, after which the radiative feedback quenches further gas accretion. This is a spatially coarse calculation, thus this could be used as the upper bound of the separation of Pop III binaries. Owing to the second equation, binaries can avoid Roche-lobe overflow from the beginning time. We choose a_{\min} in section 2.4.

The eccentricity distribution is the thermal distribution with modification as

$$f(e_i) \propto e_i \quad (0 \leq e_i \leq e_{\max}) \quad (19)$$

$$e_{\max} = 1 - a'_{\min}/a_i \quad (20)$$

The modification makes pericenter distance larger than a'_{\min} at the initial time. Note that $e_{\max} = 1$ if the eccentricity distribution is completely thermal.

Each star has nearly no rotation at the initial time.

2.4. Parameter sets

We prepare a bunch of parameter sets summarized in Table 1. We mainly focus on 16 parameter sets (hereafter, the main 16 models) in which we consider non- and $Z = 10^{-3}Z_\odot$ stellar winds, and $\sigma_k = 0, 265 \text{ km s}^{-1}$, $q_{\min} = 0.0, 0.9$, and $a_{\min} = 10, 200R_\odot$. We suppose that these stellar winds are weak and strong extremes. The natal kick velocities of $\sigma_k = 0$ and 265 km s^{-1} are also weak and strong extremes. We adopt $\sigma_k = 265 \text{ km s}^{-1}$ obtained in Hobbs et al. (2005). We set $q_{\min} = 0.0$ and 0.9 . We can get variety of mass combinations for $q_{\min} = 0.0$, while we restrict the mass combinations for $q_{\min} = 0.9$ due to the fact that the mass ratios of binaries tend to be close to unity (Susa 2019). We use $a_{\min} = 200R_\odot$, since Pop. III stars can expand to $\gtrsim 100R_\odot$ at their protostellar phases (Stahler et al. 1986; Omukai & Palla 2001, 2003), and binaries with $a \lesssim 100R_\odot$ can merge before they enter into their MS phases. Nevertheless, we also choose $a_{\min} = 10R_\odot$. This is because they may avoid their mergers for unknown reasons. In fact, the evolution of the protostellar radius in the proto-binary system is not known, although only a single star evolution has been investigated so far assuming spherically symmetric mass accretion (Stahler et al. 1986; Omukai & Palla 2001, 2003). It is also worth noting that such close binaries with $a \lesssim 100R_\odot$ may be formed through dynamical processes after they enter into their MS phases. The model names are named after w/ and w/o wind, w/ and w/o kick, and the values of q_{\min} and a_{\min} . The “opti” and “pess” stand for “optimistic” and “pessimistic”, respectively. The “opti” and “pess” models are thought to form large and small numbers of merging BH-BHs, respectively.

Note that the natal kick velocities are smaller for larger remnant masses in the prescription that is usually adopted in the literature. However, we do not adopt here this prescription. In the commonly used prescription, kick velocities are set to $\sigma_k(M_{\text{rem}}/M_{\text{rem},0})^{-1}$, where $\sigma_k = 265 \text{ km s}^{-1}$ and $M_{\text{rem},0} = 3.0M_\odot$ (e.g. Wang et al. 2016). BHs with $\sim 10M_\odot$ receive kick velocities of $\sim 80 \text{ km s}^{-1}$. On the other hand, BH-BHs with two $\sim 10M_\odot$ BHs have orbital velocities of

Table 1. Summary of parameter sets.

Model	Wind	σ_k	q_{\min}	a_{\min}
optiq0.0a1e1	w/o	0	0.0	10
optiq0.0a2e2	w/o	0	0.0	200
optiq0.9a1e1	w/o	0	0.9	10
optiq0.9a2e2	w/o	0	0.9	200
kickq0.0a1e1	w/o	265	0.0	10
kickq0.0a2e2	w/o	265	0.0	200
kickq0.9a1e1	w/o	265	0.9	10
kickq0.9a2e2	w/o	265	0.9	200
windq0.0a1e1	$10^{-3} Z_{\odot}$	0	0.0	10
windq0.0a2e2	$10^{-3} Z_{\odot}$	0	0.0	200
windq0.9a1e1	$10^{-3} Z_{\odot}$	0	0.9	10
windq0.9a2e2	$10^{-3} Z_{\odot}$	0	0.9	200
pessq0.0a1e1	$10^{-3} Z_{\odot}$	265	0.0	10
pessq0.0a2e2	$10^{-3} Z_{\odot}$	265	0.0	200
pessq0.9a1e1	$10^{-3} Z_{\odot}$	265	0.9	10
pessq0.9a2e2	$10^{-3} Z_{\odot}$	265	0.9	200
half-kick	w/o	130	0.0	10
weak-wind	$10^{-5} Z_{\odot}$	0	0.0	10
no-rot-wind	$10^{-3} Z_{\odot}$	0	0.0	10
K14	w/o	0	0.0	0

NOTE—The units of σ_k and a_{\min} are km s^{-1} and R_{\odot} , respectively. In the wind column, metallicity adopted for our wind model is described. In the “no-rot-wind” model, we do not account for rotationally enhanced stellar winds, $\dot{M}_{\text{wind,rot}}$. In the “K14” model, we set the $m_{1,i}$ distribution as $f(m_{1,i}) \propto \text{const}$ ($10 \leq m_{1,i}/M_{\odot} \leq 100$), and do not take into account PPI effects.

$\gtrsim 400 \text{ km s}^{-1}$ if they merge within the Hubble time. Thus, such BH natal kicks have small effects on merging BH-BHs within the Hubble time. The effects becomes smaller for more massive BHs. Even if we adopt the usual prescription, we will get similar results to those of models without BH natal kicks. Moreover, the usual prescription may be hard to explain several X-ray binaries with BHs (Willems et al. 2005; Wong et al. 2012; Repetto & Nelemans 2015; Repetto et al. 2017; Mandel 2016; Gandhi et al. 2019, 2020). The spin-orbit misalignment of GW 190412 needs natal kicks of several 100 km s^{-1} , if GW 190412 is formed through binary evolution (Olejak et al. 2020; Safarzadeh & Hotokezaka 2020). There are several theoretical studies for natal kicks with high velocities (Batta & Ramirez-Ruiz 2019; Barkov & Komissarov 2010).

Additionally, we make 4 parameter sets. For the “half-kick” model, we investigate the dependence of BH-BH populations on natal kick velocities. We examine effects of metallicity and rotational enhancement on stellar winds, investigating the “weak-wind” and “no-rot-wind” models, respectively. In order to compare our results with results in Kinugawa et al. (2020a), we prepare the K14 model, which has initial condition and single/binary star models similar to the K14 model in Kinugawa et al. (2020a).

For each parameter set, we follow time evolutions of 10^6 binaries until 100 Gyr. The initial conditions of 10^6 binaries are the same if q_{\min} and a_{\min} are identical. For each parameter set, we spend 1–2 hours calculating on 1 CPU core of Intel Core i9-7980XE CPU with turbo boost enabled.

2.5. Pop. III formation model

In this paper, we adopt Pop. III formation model as follows. All Pop. III stars are formed in minihalos at the same time. Only one Pop. III binary is born in one minihalo, $\eta_{\text{bin}} = 1$. The number density of the minihalos is $n_{\text{DM}} = 10^{11} \text{ Gpc}^{-3}$. Then, the number density of Pop. III binaries is 10^{11} Gpc^{-3} . Using Eq. (16), we can obtain the mass density of Pop. III binaries as $1.3 \times 10^{13} M_{\odot} \text{ Gpc}^{-3}$ for $q_{\min} = 0.0$ and $1.7 \times 10^{13} M_{\odot} \text{ Gpc}^{-3}$ for $q_{\min} = 0.9$. Our mass density is a fraction of the Pop. III star density of $\sim 10^{14} M_{\odot} \text{ Gpc}^{-3}$ (see Figure 2 of Magg et al. (2016)), and $\sim 3 \times 10^{13} M_{\odot} \text{ Gpc}^{-3}$ (see Figure 4 of Skinner & Wise (2020)). On the other hand, our mass density is smaller than in Kinugawa et al. (2020a) by 2 orders of magnitude. They have estimated Pop. III mass density from results of de Souza et al. (2011) modified by the argument of Inayoshi et al. (2016). We can interpret that our formation rate is the lower limit.

According to Magg et al. (2016), Pop. III stars stop forming at $z \sim 5$, or at the lookback time of ~ 12.5 Gyr. Thus, Pop. III BH-BHs which merge in the local universe should have the delay time of ~ 12.5 –13.8 Gyr. Note that the upper bound should be less than 13.8 Gyr, since Pop. III stars are not formed at the beginning of the universe. However, we assume that Pop. III BH-BHs with the delay time of ~ 10 –15 Gyr merge in the local universe. This assumption enables us to obtain many Pop. III BH-BHs from our binary population synthesis calculations, and investigate their mass and spin distributions in the local universe.

3. RESULTS

We describe the results of binary population synthesis calculations. In section 3.1, we show the relation

between ZAMS and remnant masses through single star evolution. It is instructive to investigate the dependence of the relation on stellar winds. In section 3.2, we compare our results with those of Kinugawa et al. (2020a), examining the K14 model. In section 3.3, we present populations of merging Pop. III BH-BHs.

3.1. Single star evolution

In Figure 3, we show the relation between ZAMS and remnant masses. The maximum ZAMS mass is $600M_\odot$, which is the possible maximum mass of binaries in our calculations. Moreover, a star with this maximum ZAMS mass creates a He core with $\sim 300M_\odot$, and can form a nHe star with $\sim 300M_\odot$. As described in section 2.1, we confirm that our stellar wind model is valid for nHe stars with $\lesssim 300M_\odot$. We can see the metallicity dependence without $\dot{M}_{\text{wind,rot}}$ in the top panel, and the dependence on stellar rotation speeds for $Z = 10^{-3}$ and $10^{-5}Z_\odot$ in the middle and bottom panels, respectively. We forcibly fix stellar rotation periods for stars in the middle and bottom panels. There are two reasons for this treatment. First, we simply attempt to investigate effects of stellar rotations on stellar wind mass loss. Second, stars could keep their rotation periods when they are synchronized with binary motions.

We first focus on the top panel. For any winds without $\dot{M}_{\text{wind,rot}}$, stars with $M_{\text{ZAMS}} \lesssim 20M_\odot$ and $\gtrsim 20M_\odot$ leave NSs and BHs, respectively. We can see that BH masses once decrease at $M_{\text{ZAMS}} \sim 25M_\odot$, which is a feature of the rapid model we adopt (see Eq. (6) in detail). Stars with $M_{\text{ZAMS}} \sim 90 - 120M_\odot$ have $45M_\odot$ BHs due to the PPI effect, stars with $M_{\text{ZAMS}} \sim 120 - 250M_\odot$ leave no remnant due to the PISN effect, and stars with $M_{\text{ZAMS}} \gtrsim 250M_\odot$ undergo direct collapse to BHs. PPI/PISN effects make “the pair-instability (PI) mass gap” from $45M_\odot$ to $135M_\odot$. Nevertheless, some of stars can have BHs in the PI mass gap. Their maximum mass is $\sim 85M_\odot$. They can avoid PPI/PISN effects due to small He core masses, and can grow to $> 45M_\odot$ owing to massive H envelopes. For $M_{\text{ZAMS}} \lesssim 250M_\odot$, the relations has weak dependence on metallicity. For $M_{\text{ZAMS}} \gtrsim 250M_\odot$, stars receiving $10^{-3}Z_\odot$ winds leave BHs with distinctly smaller masses than the other cases. This is due to luminous-star winds (\dot{M}_{NJ}).

In the middle panel, we can find that the boundary between NSs and BHs as well as the PPI/PISN effects are similar to the case of winds without $\dot{M}_{\text{wind,rot}}$. For $M_{\text{ZAMS}} \lesssim 120M_\odot$, BH masses become smaller with rotation periods smaller. Stars with rotation periods of 10^4 days keep their H envelopes to the ends of their lives. On the other hand, stars with rotation periods of 1 and 100 days become nHe stars when their ZAMS masses

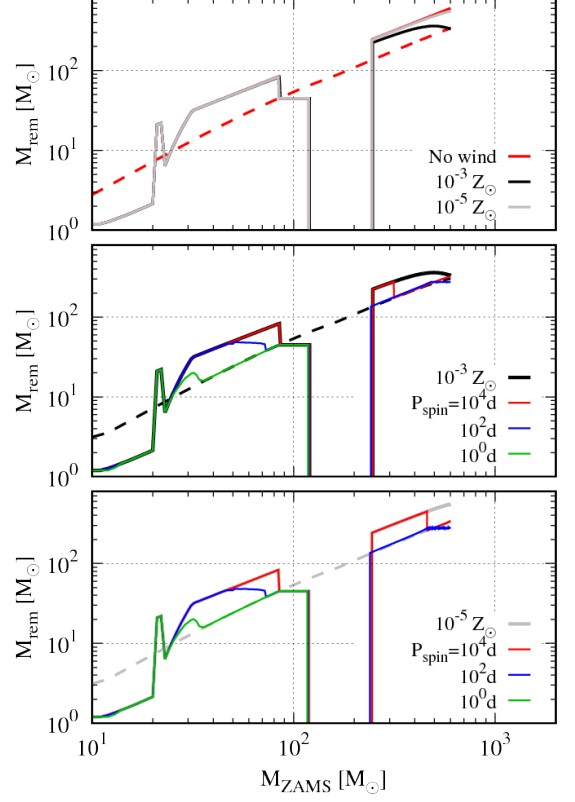


Figure 3. Relation between ZAMS and remnant masses. In the top panel, stars receive no wind (red), $10^{-3}Z_\odot$ winds (black), and $10^{-5}Z_\odot$ winds (gray). The stars receive no wind, or winds without $\dot{M}_{\text{wind,rot}}$. In the middle and bottom panels, stars receive winds with $Z = 10^{-3}$ and $10^{-5}Z_\odot$, respectively. The black and gray curves in the middle and bottom panels are identical with those in the top panel, respectively. In the middle and bottom panels, stars receive winds with $\dot{M}_{\text{wind,rot}}$ except for stars indicated by the black and gray curves. They are forced to keep stellar rotations with periods of 10^4 (red), 10^2 (blue), and 1 days (green). As guides, He core masses are indicated by dashed curves in stars receiving no wind (top), $10^{-3}Z_\odot$ winds without $\dot{M}_{\text{wind,rot}}$ (middle), and $10^{-5}Z_\odot$ winds without $\dot{M}_{\text{wind,rot}}$ (bottom).

are $M_{\text{ZAMS}} \gtrsim 35M_\odot$ and $\gtrsim 70M_\odot$, respectively. For $M_{\text{ZAMS}} \gtrsim 250M_\odot$, stars with smaller periods also leave BHs with smaller masses. For periods of 1 day, stars undergo PISNe, and leave no remnants, since they lose large amounts of masses in their MS phases, and create their He core with $65 - 135M_\odot$ entering into their CHeB phases. For periods of 10^2 days, they become nHe stars. For periods of 10^4 days, BH masses are suddenly decreased at $M_{\text{ZAMS}} \sim 300M_\odot$. Stars with $M_{\text{ZAMS}} \lesssim 300M_\odot$ keep their H envelopes, while those with $M_{\text{ZAMS}} \gtrsim 300M_\odot$ become nHe stars. This is because luminosities of the latter stars exceed their Eddington limit in the middle of their evolution. Thus,

they lose large amounts of their masses, and become nHe stars.

In many cases, we can see that stars lose large amounts of masses in MS, CHeB, and ShHeB phases, and stop losing masses in nHe phases. This is because the Eddington luminosity is increased from the former phases to the latter phase. Then, rotationally enhanced mass loss becomes inactive when stars reach to nHe stars.

We find that the relations are weakly dependent on metallicity when $\dot{M}_{\text{wind,rot}}$ is taken into account (see the middle and bottom panels). Nevertheless, for rotation periods of 10^4 days, BH masses are suddenly decreased at different M_{ZAMS} : $M_{\text{ZAMS}} \sim 300M_{\odot}$ for $Z = 10^{-3}Z_{\odot}$, and $M_{\text{ZAMS}} \sim 450M_{\odot}$ for $Z = 10^{-5}Z_{\odot}$. Stars with $Z = 10^{-5}Z_{\odot}$ are harder to lose mass than those with $Z = 10^{-3}Z_{\odot}$, since they have larger masses, i.e. larger Eddington limit, owing to slightly weaker stellar winds.

3.2. Comparison with K14

We describe calculation results of our K14 model to compare them with the K14 model in Kinugawa et al. (2020a) (hereafter, the original K14 model). Figure 4 shows the chirp mass distribution of merging BH-BHs within 15 Gyr in our K14 model. Hereafter, we use 15 Gyr as the Hubble time, since it's just a round number. The chirp mass of BH-BHs can be expressed as

$$m_{\text{chirp}} = \frac{(m_{\text{b,p}}m_{\text{b,s}})^{3/5}}{(m_{\text{b,p}} + m_{\text{b,s}})^{1/5}}, \quad (21)$$

where $m_{\text{b,p}}$ and $m_{\text{b,s}}$ are the primary and secondary BH masses of BH-BHs. We find that it is quite consistent with the results of the original K14 model (see the purple curve in their Figure 3). Both the K14 models have sharp peaks at $m_{\text{chirp}} \sim 30M_{\odot}$. Our K14 model has sharp drop at $m_{\text{chirp}} \sim 60M_{\odot}$, while the original K14 model do so at $m_{\text{chirp}} \sim 80M_{\odot}$. This comes from different treatments of H envelopes of post-MS stars whose H envelopes are almost stripped. If the treatments are the same, the sharp drop is at $m_{\text{chirp}} \sim 60M_{\odot}$ even in the original K14 model (see the light-blue curve of Figure 1 in Kinugawa et al. (2016a)). We emphasize these agreements are very surprising. This is because they and we use fitting formulae of Pop. III stars based on different stellar evolution models (Marigo et al. 2001; Tanikawa et al. 2020c, respectively). These results reinforce the argument of Kinugawa et al. (2014) that typical Pop. III BH-BH mergers have $\sim 30M_{\odot}$ BHs.

We can see the delay time (t_d) distribution of BH-BHs in our K14 model in Figure 5, where t_d is delay time, or defined as time interval from the ZAMS time to the BH-BH merger time. The black curve indicates the distribution of all the BH-BHs, while the other curves

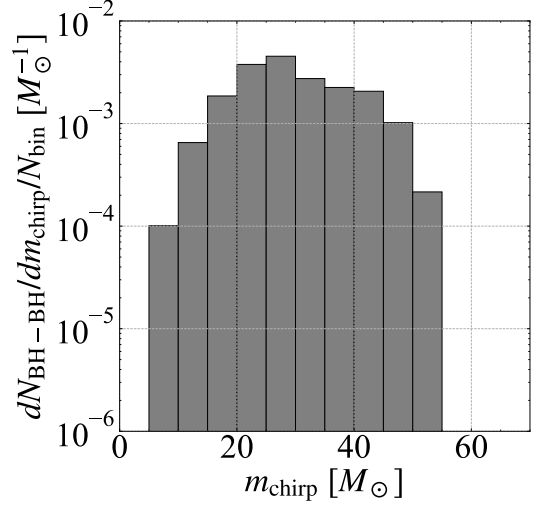


Figure 4. Chirp mass distribution of merging BH-BHs within 15 Gyr in our K14 model. The number of merging BH-BHs ($N_{\text{BH-BH}}$) is normalized by the total number of binaries, $N_{\text{bin}} = 10^6$.

indicates the distribution of BH-BHs formed through channels of CE0, CE1, CE2, CE3, and CE4. In the CE0 channel, binary systems experience no common envelope evolution. In the CE1 and CE2 channels, they undergo common envelope evolution, ejecting H envelopes of the 1st- and 2nd-evolving stars, respectively. In the CE3 channel, they have both the CE1 and CE2 channels. In the CE4 channel, they go through common envelope evolution, ejecting H envelopes of both the 1st- and 2nd-evolving stars at the same time.

The delay time distribution of all the BH-BHs is similar to the original K14 model (see the purple curve in their Figure 4). Note that their values in the vertical axis are 6 digits larger than ours, since they do not normalize the number of BH-BHs by the total number of binaries. The number of mergers are sharply increased at several Myr, and are gradually decreased until several 10 Myr. After that, the number turns to rise, and reaches to a few 10^{-3} at 10 Gyr.

We recognize common and different features, comparing the delay time distribution of BH-BHs formed through each channel (see their Figure 5(e)). The common feature is that the dominant channels are CE4 and CE0 at earlier and later times than a few 10 Myr, respectively. Another common feature is the distribution of BH-BHs formed through the CE1 channel. The BH-BHs start formed from $\sim 10^2$ Myr, and keep the number $\sim 10^{-3}$ after that.

The numbers of BH-BHs formed through the CE2 and CE3 channels in our K14 model are much smaller than in the original K14 model. This is because our

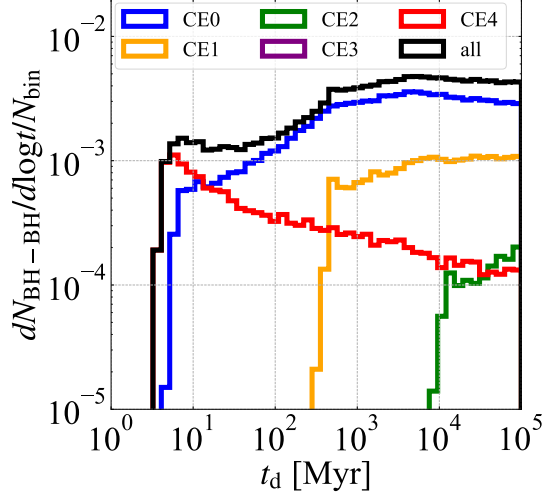


Figure 5. Delay time distribution of BH-BHs in our K14 model. The normalization is the same as in Figure 4. The black curve indicates the distribution of all the BH-BHs. All colored curves indicates BH-BHs formed through channels related to common envelope evolutions defined in the main text. There is no BH-BH formed through the CE3 channel.

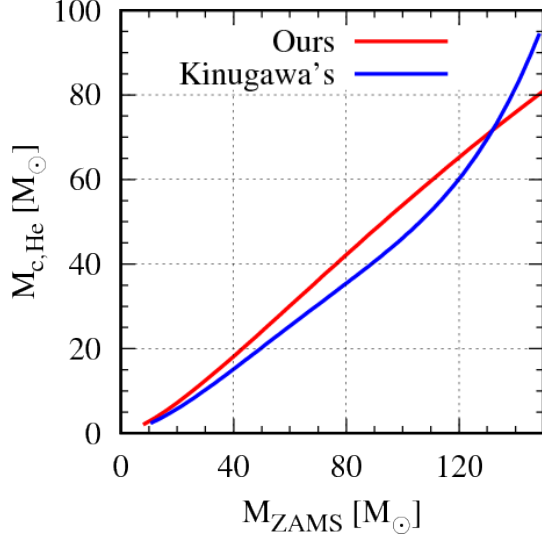


Figure 6. Relation between ZAMS and He core masses at the carbon ignition time in fitting formulae of Kinugawa et al. (2020a) (blue) and Tanikawa et al. (2020c) (red).

fitting formulae of single star models have larger He core masses than theirs (see Figure 6). As the ratios of He core masses to the stellar masses become larger, common envelope evolution is harder to happen. Although He core masses in our fitting formulae are smaller than Kinugawa's ones for $M_{\text{ZAMS}} \gtrsim 130 M_{\odot}$, stars with $M_{\text{ZAMS}} \gtrsim 130 M_{\odot}$ have small chance to undergo the CE2 and CE3 channels in both the K14 models.

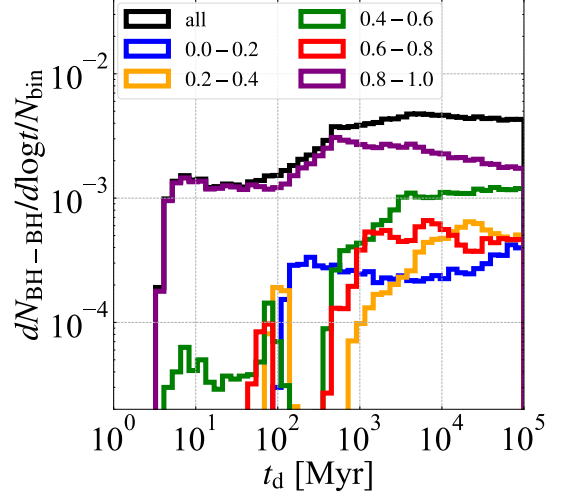


Figure 7. Delay time distribution of BH-BHs in our K14 model. The normalization is the same as in Figure 4. The black curve indicates the distribution of all the BH-BHs. Other curves indicate the distribution of BH-BHs with effective spins (χ_{eff}) described in the legend. The definition of χ_{eff} is in the main text.

Figure 7 shows the delay time distribution of BH-BHs with effective spins, χ_{eff} . The definition of χ_{eff} is given by

$$\chi_{\text{eff}} = \left(\frac{m_{\text{b,p}} \vec{\chi}_{\text{p}} + m_{\text{b,s}} \vec{\chi}_{\text{s}}}{m_{\text{b,p}} + m_{\text{b,s}}} \right) \cdot \frac{\vec{L}}{|\vec{L}|}, \quad (22)$$

where $\vec{\chi}_{\text{p}}$ and $\vec{\chi}_{\text{s}}$ are normalized spin vectors of the primary and secondary BHs. We are going to making comparison between χ_{eff} evolution in both the K14 models. However, we should note that we cannot strictly compare Figure 7 with χ_{eff} evolution shown in the original K14 model (see their Figure 7(e)). We assume that all the stars are instantaneously born at $t = 0$, while they adopt a Pop. III star formation history in which Pop. III stars have a width of their formation times. In addition, the horizontal axes of our and their figures are time and redshift, respectively.

There are several common features. We find BH-BHs with $0.8 < \chi_{\text{eff}} < 1.0$ are always dominant in both the results. When we compare the numbers at 10 Gyr in our K14 model with those at $z = 0$ in the original K14 model, BH-BHs with $\chi_{\text{eff}} < 0.8$ have significant contributions to the numbers in both the K14 models. However, the numbers are quite different at an early time. In our K14 model, only BH-BHs with $0.8 < \chi_{\text{eff}} < 1.0$ merge at time $< 10^2$ Myr. On the other hand, BH-BHs with $0.4 < \chi_{\text{eff}} < 0.6$ and $0.8 < \chi_{\text{eff}} < 1.0$ have comparable contributions in the original K14 model. These differences can be explained by the difference between

spin models. In our model, BHs keep their spin angular momenta even when they lose their masses at their collapse. On the other hand, in the original K14 model, BHs lose their spin angular momenta. Nevertheless, spin distributions in both the K14 models are consistent in the current universe.

3.3. Merging BH-BHs

Figure 8 shows the average merger rate density of BH-BHs for $t_d = 0 - 15$ Gyr in the optiq0.0a1e1 model. We define the merger rate density as

$$\Gamma = \frac{d(N_{\text{BH-BH}}/N_{\text{bin}})}{dt_d} \left(\frac{\eta_{\text{bin}}}{1} \right) \left(\frac{n_{\text{DM}}}{10^{11} \text{Gpc}^{-3}} \right) [\text{yr}^{-1} \text{Gpc}^{-3}]. \quad (23)$$

As seen in the above formula, the average merger rate density is defined in the local comoving volume at the source frame time. Using Eq. (23), we can express the average merger rate density as

$$\bar{\Gamma} = \frac{1}{t_{d,f} - t_{d,i}} \int_{t_{d,i}}^{t_{d,f}} \Gamma dt_d, \quad (24)$$

where $t_{d,i}$ and $t_{d,f}$ are the beginning and ending times for the averaging.

We can clearly see there are three subpopulations of BH-BHs: those with two low-mass BHs (lBHs), those with one lBH and one high-mass BH (hBH), and those with two hBHs, where we call BHs with $\lesssim 50 M_\odot$ “lBHs”, and BHs with $\gtrsim 130 M_\odot$ “hBHs”. There is a large mass gap between lBHs and hBHs due to PPI/PISN effects, the PI mass gap, as seen also in Figure 3. The mass gap ranges from $\sim 50 M_\odot$ to $\sim 130 M_\odot$. Hereafter, we name BH-BHs with two lBHs, those with one lBH and one hBH, and those with two hBHs “hBH0”, “hBH1”, and “hBH2”, respectively, after the numbers of hBHs. The mass ranges of lBHs and hBHs are quite different; the maximum mass of lBHs is $\sim 50 M_\odot$, and the minimum mass of hBHs is $\sim 135 M_\odot$. Stars with $M_{\text{c,He}} < 45 M_\odot$ and H envelopes can leave $> 45 M_\odot$ BHs avoiding PPI, and leave BHs with $\sim 50 M_\odot$ at most. Thus, we can identify hBH0, hBH1, and hBH2 as distinct subpopulations.

In Figure 9, we show the merger rate density of hBH0, hBH1, and hBH2 as a function of t_d in the main 16 models. The merger rate densities are not necessarily proportional to t_d^{-1} . Some of merger rate densities suddenly increase, since the dominant formation channels of BH-BHs are switched. For example, for the hBH2s of the optiq0.0a2e2 model, the dominant formation channels are switched from CE4 to CE0 at $t_d \sim 10$ Gyr. For $t_d \lesssim 0.1$ Gyr, some of merger rate densities decrease more slowly than t_d^{-1} . This is because a part of BH-BH

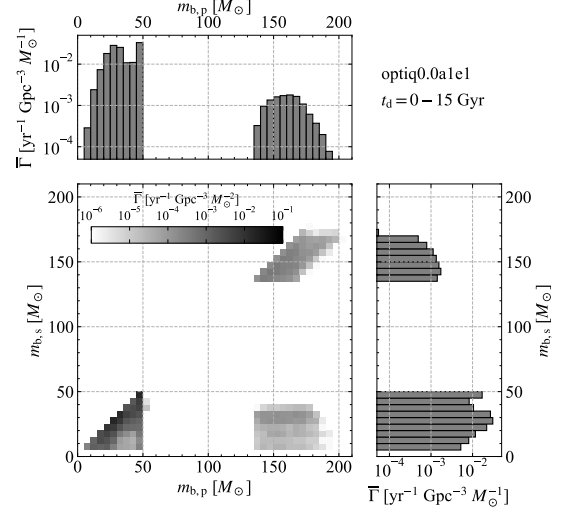


Figure 8. Average merger rate density of BH-BHs for $t_d = 0 - 15$ Gyr.

progenitors with $t_d \gtrsim 0.1$ Gyr shrink their orbits due to mechanisms other than common envelope evolutions. One mechanism is BH natal kicks. We can see that the BH natal kicks yield hBH1s with $t_d \lesssim 0.1$ Gyr, comparing merger rate densities of hBH1s in the optiq0.0a1e1 and kickq0.0a1e1 models. Another mechanism is stable mass transfer in which the mass ratio of a donor star to an accretor star is sufficiently larger than unity. This can sometimes strip H envelopes of post-MS stars. This can be seen in hBH0s of the optiq0.0a1e1 model.

In the present day (~ 10 Gyr), the merger rates of hBH0s are $\sim 0.1 \text{ yr}^{-1} \text{Gpc}^{-3}$, independently of single star models, q_{min} , and a_{min} . This is much smaller than the merger rate density inferred by LIGO/Virgo observations, $\sim 10 - 100 \text{ yr}^{-1} \text{Gpc}^{-3}$ (Abbott et al. 2019). Although this is smaller than estimated by Kinugawa et al. (2020a) by 2 orders of magnitude, this is consistent with their results, since the total Pop. III mass in our model is smaller than theirs by 2 orders of magnitude (see section 2.5). If our formation model is close to the actual formation rate, we may not expect that Pop. III hBH0 are a dominant origin of GW sources discovered currently. However, it should be worth examining properties of Pop. III hBH0s for the following reason. It is important to identify Pop. III hBH0s with respect to the star formation history in the universe, and moreover future GW observatories, such as Einstein telescope (Punturo et al. 2010; Maggiore et al. 2020) and Cosmic explorer (Reitze et al. 2019), may detect a large number of Pop. III hBH0s.

We also inspect hBH1s and hBH2s for the following reason. María Ezquiaga & Holz (2020) have shown

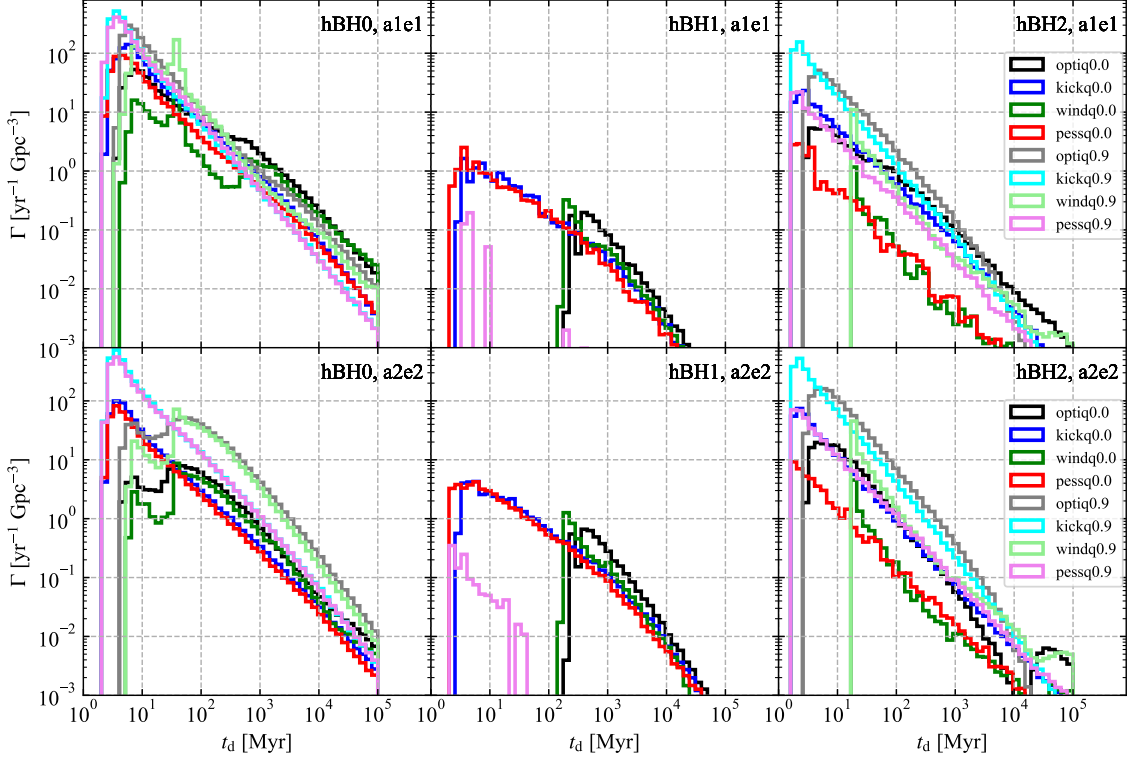


Figure 9. Merger rate densities of hBH0, hBH1, and hBH2 as a function of the delay time in the main 16 models. The left, middle, and right panels indicate the distributions of hBH0s, hBH1s, and hBH2s, respectively. The top and bottom panels indicate models with $a_{\min} = 10$ and $200R_{\odot}$, respectively. Colors of the curves show single star models and q_{\min} .

that hBH1s and hBH2s can be detected by the current GW observatories if they merge within detectable distances, although they have not yet been detected. Moreover, space-borne GW observatories, such as LISA and DECIGO (Amaro-Seoane et al. 2017; Kawamura et al. 2006, respectively), may be helpful for searching merging hBHs. Especially, LISA will detect hBHs months to years before hBH mergers in the local universe (Sesana 2016).

Before we examine hBH0s, hBH1s, and hBH2s separately, we investigate their initial conditions and formation channels. By this, we make clear the reason why the merger rates of hBH0s and the sum of hBH1s and hBH2s do not depend on initial conditions and single star models. First, we mainly focus on the dependence on initial conditions. Second, we mention the dependence on single star models.

Figure 10 shows initial conditions of Pop. III binaries which form BH-BHs merging within 15 Gyr for the optiq0.0a1e1 model. We separate the initial conditions into two panels by whether $q_i < 0.9$ or $q_i \geq 0.9$, and mark an initial pericenter distance ($r_{p,i}$) of $200R_{\odot}$ by vertical dashed lines, so as to imagine results of models with $q_{\min} = 0.9$ and $a_{\min} = 200R_{\odot}$. We can see a gap between $m_{1,i} \sim 120 - 250M_{\odot}$ in which BH-BHs are not

formed. This is due to PISN effects. All hBH0s are under this gap, and all hBH1s and hBH2s are above this gap. In other words, binaries with 1st-evolving stars with $m_{1,i} \lesssim 120M_{\odot}$ can form only hBH0s, and binaries with 1st-evolving stars with $m_{1,i} \gtrsim 250M_{\odot}$ can form only hBH1s and hBH2s. In both the panels, there is no BH-BH on the top-left and right-bottom corners. The reason for their absence on the top-left corner is that binaries merge before they form BH-BHs, and the reason for their absence on the bottom-right corner is that BH-BHs have too wide separation to merge within 15 Gyr.

Even binaries with $r_{p,i} \sim 10^3R_{\odot}$ can form hBH0s, hBH1s, and hBH2s. This is because Pop. III stars with $M \gtrsim 50M_{\odot}$ expand to $\gtrsim 10^3R_{\odot}$ (see Figure 1), and interact with their companions. Thus, the merger rates of hBH0s, hBH1s, and hBH2s in models with $a_{\min} = 200R_{\odot}$ are comparable to those in models with $a_{\min} = 10R_{\odot}$ as seen in Figure 9.

There is no hBH1 in the bottom panel. Binaries with high q_i can not form a hBH1, since their members have similar masses. This is consistent with the merger rate density as a function of t_d in the middle panels of Figure 9. The merger rate of hBH1s is nearly zero in models with $q_{\min} = 0.9$. Nevertheless, the sums of the merger rates of hBH1s and hBH2s are independent of q_{\min} , since

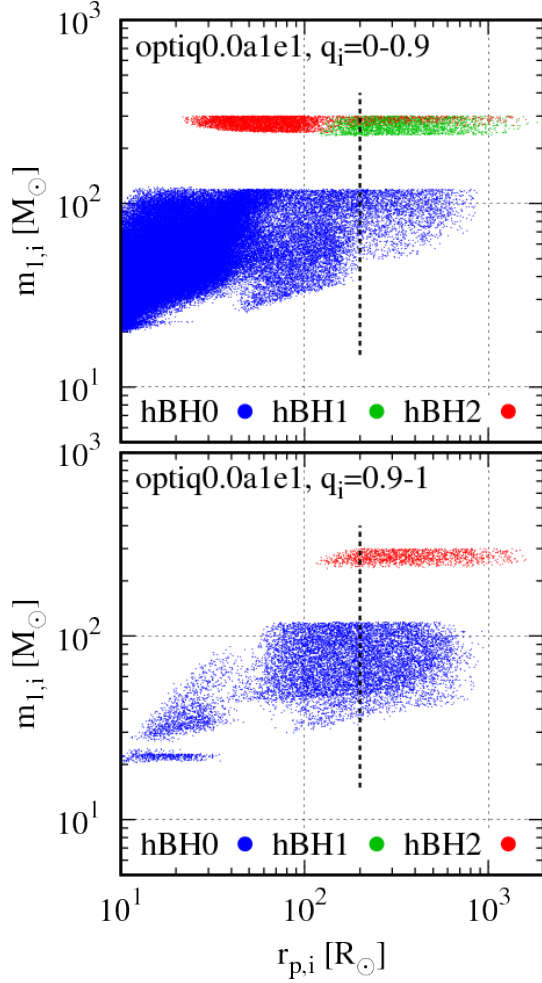


Figure 10. Initial pericenter distances ($r_{p,i}$) and 1st-evolving star’s masses ($m_{1,i}$) of BH-BHs with $t_d = 0-15$ Gyr in the optiq0.0a1e1 model. In the top and bottom panels, the initial mass ratios (q_i) are $0-0.9$ and $0.9-1$, respectively. The vertical dashed lines indicate $r_{p,i} = 200R_\odot$. The color codes show hBH0, hBH1, and hBH2.

the increase of the hBH2 merger rate compensates for the decrease of the hBH1 merger rate in the case of $q_{\min} = 0.9$.

We have to keep in mind that, although the merger rates of hBH0s and the sum of hBH1s and hBH2s are insensitive to a_{\min} and q_{\min} , their formation channels can depend on a_{\min} and q_{\min} . Figure 11 is the same plot as Figure 10, except for color codes that indicate CE channels forming BH-BHs. We can see that hBH0s are formed from binaries with $r_{p,i} \lesssim 50R_\odot$ and $\gtrsim 50R_\odot$ through stable mass transfer (the CE0 channel), and common envelope evolution (the CE1, CE2, and CE4 channels), respectively. The boundary of $r_{p,i}$ increases with $m_{1,i}$, since BSG stars can have larger radii with $m_{1,i}$. The reason for the absence of the CE3 channel is described in section 3.2. Thus, only the CE1, CE2, and

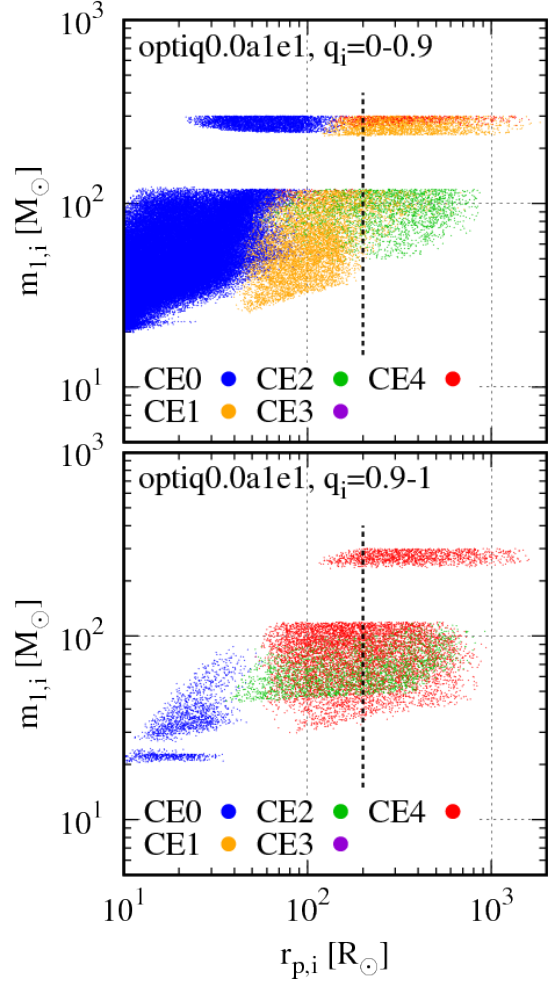


Figure 11. The same as in Figure 10, except for color codes that indicate CE channels forming BH-BHs.

CE4 channels work for forming hBH0s in the cases of $a_{\min} = 200R_\odot$.

All the hBH1s are formed from binaries with $r_{p,i} \gtrsim 10^2 R_\odot$ through the CE1 channel. We draw an example binary evolution leading to one hBH1 in Figure 12. To form hBH1s, binaries should have a small q_i . Due to the small q_i , a binary experiences merger or common envelope evolution when the 1st-evolving star fills its Roche lobe. If the 1st-evolving star is in its MS and CHEB/ShHeB phases, the binary experiences merger and common envelope evolution, respectively. The common envelope evolution reduces the binary separation down to several $10R_\odot$. Then, the 2nd-evolving star expands to $\sim 10R_\odot$, fills its Roche lobe, and drives stable mass transfer, since it is a BSG star, and the mass ratio of it to the 1st BH is small. Eventually, binaries forming hBH1s experience common envelope evolution driven by the 1st-evolving star, i.e. the CE1 channel.

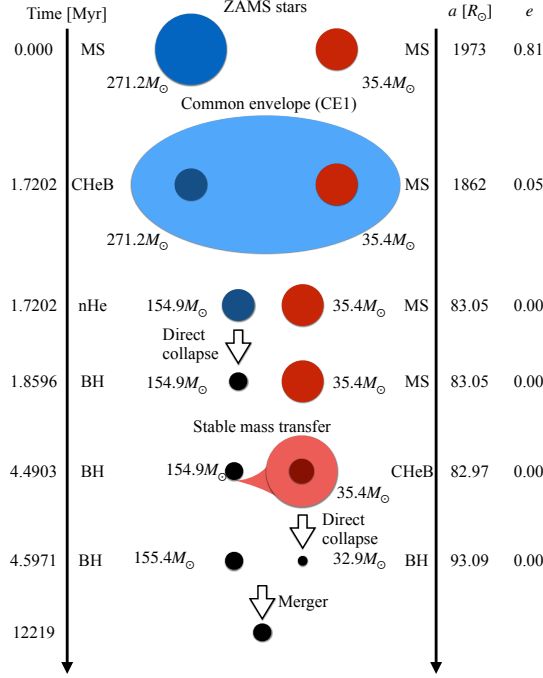


Figure 12. Example binary evolution leading to one hBH1 through the CE1 channel.

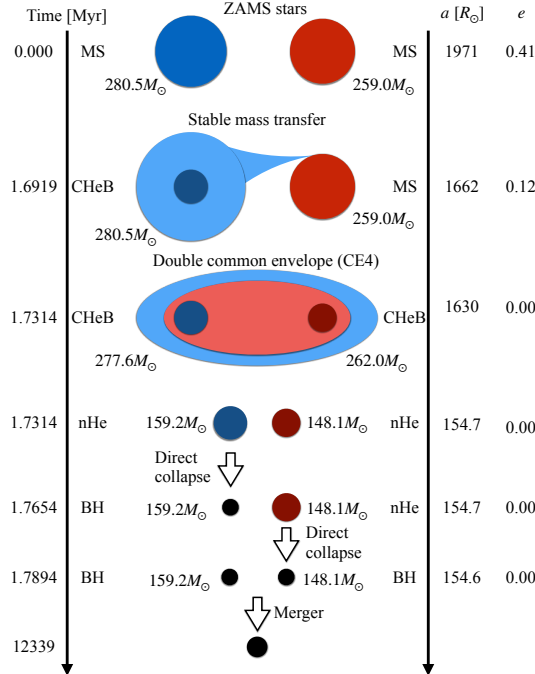


Figure 13. Example binary evolution leading to one hBH2 through the CE4 channel.

A part of hBH2s are formed from binaries with $r_{p,i} \lesssim 10^2 R_\odot$ through the CE0 channel, and the rest of them from binaries with $r_{p,i} \gtrsim 10^2 R_\odot$ through the CE4 channel. For binaries with $r_{p,i} \lesssim 10^2 R_\odot$, both the 1st- and 2nd-evolving stars fill their Roche lobes when they are BSG stars. Then, they drive stable mass transfer, i.e. the CE0 channel. For binaries with $r_{p,i} \gtrsim 10^2 R_\odot$, they enter into their CHeB/ShHeB phases almost at the same time due to their similar masses, and fill their Roche lobes. Then, the binaries experience the CE4 channel. We draw an example binary evolution leading to one hBH2 through the CE4 channel in Figure 13, which can occur regardless of q_{\min} and q_{\min} as seen in Figure 10.

The merger rates of hBH0s, hBH1s, and hBH2s are insensitive to single star models for the following reasons. Natal kicks have small effects on binary parameters of BH-BHs. This is because the natal kick velocities are comparable to or smaller than internal velocities of BH-BHs with $t_d < 15$ Gyr. Stellar winds do not prevent stars from filling their Roche lobe and interacting with their companions. Since they are driven by stellar rotations, they are active only when stars nearly fill their Roche lobe. They can strip H envelopes from stars, and decrease stellar masses (see Figure 3). Nevertheless, stars also lose their H envelopes through common envelope evolution (see Figure 10) even if stellar winds are switched off. Thus, stellar winds do not have dominant roles in stripping H envelopes from stars.

In the following sections, we investigate in detail hBH0, hBH1, and hBH2 in sections 3.3.1, 3.3.2, and 3.3.3, respectively. In advance, Figure 14 summarizes their features, and Figure 15 shows their characteristic features that have weak dependences on initial conditions (q_{\min} and a_{\min}) and stellar evolution models (stellar winds and natal kicks). They will help reading the following sections.

3.3.1. Binaries with two low-mass BHs (hBH0s)

We investigate first the optiq0.0a1e1 model, and next the other main models. This is because hBH0s in the optiq0.0a1e1 model have all the features the other models have, and those in the other models have a subset of them, as revealed later.

Figure 16 shows the merger rate density of hBH0s for each t_d in the optiq0.0a1e1 model. We can find two peaks in the $m_{b,p}$ and $m_{b,s}$ distributions for $t_d = 0.1 - 15$ Gyr. One peak is at $m_{b,p} \sim m_{b,s} \sim 45 - 50 M_\odot$. We call this peak “the higher-mass peak”. The higher-mass peak appears for all t_d (including $t_d = 0 - 0.1$ Gyr). The other peak is at $m_{b,p} \sim m_{b,s} \sim 20 - 35 M_\odot$ and for $t_d = 0.1 - 15$ Gyr, named “the lower-mass peak”. We do not regard that a population of $m_{b,p} = 15 - 20 M_\odot$

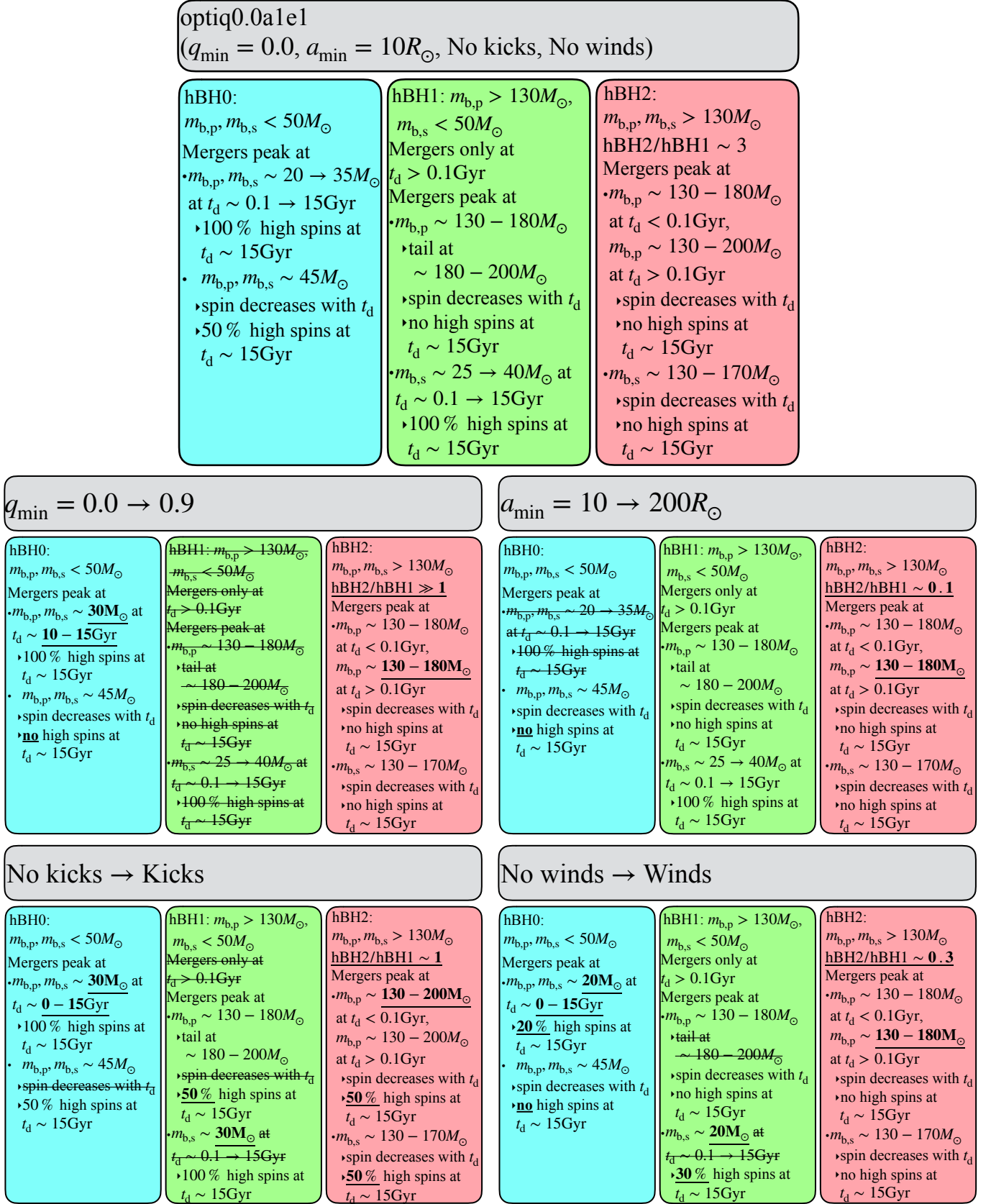


Figure 14. Features of hBH0s, hBH1s, and hBH2s for the optiq0.0a1e1 model, and their variations with initial conditions and stellar evolution models. We regard spin magnitude of ~ 0.3 as the boundary between high and low spins. The ratio of hBH2s to hBH1s is indicated by hBH2/hBH1. We cross out disappearing features, and emphasize changed values with bold font and underline. For hBH2s, $m_{b,p} \lesssim 200$ and $\lesssim 180M_{\odot}$ indicate the parallelogram and triangle shapes in 2D mass distribution, respectively. Note that these features consider only cases where only one of initial conditions and stellar models are changed.

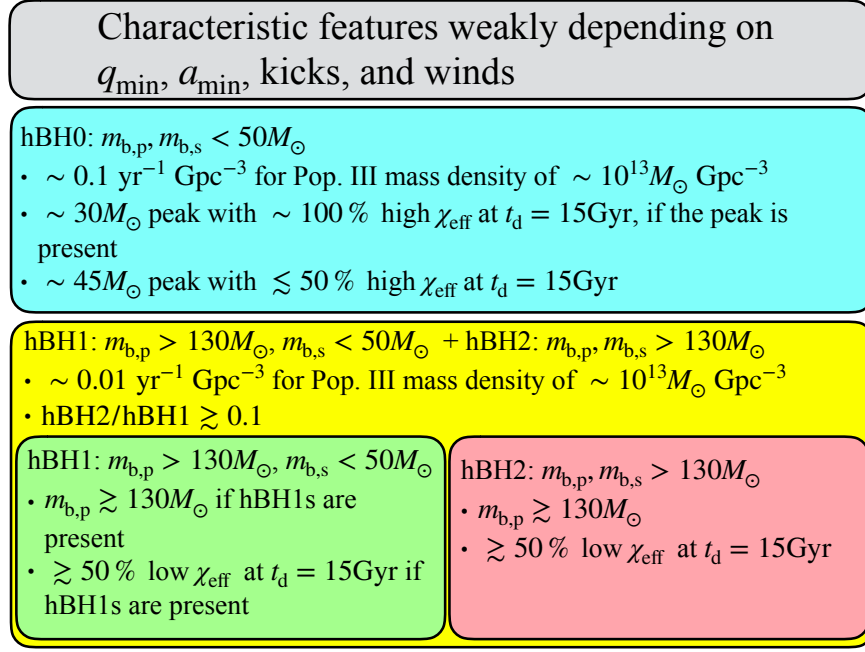


Figure 15. Characteristic features weakly depending on initial conditions (q_{\min} and a_{\min}) and stellar evolution models (stellar winds and natal kicks).

for $t_d = 0 - 0.1 \text{ Gyr}$ is associated with the lower-mass peak, since it is too weak. The lower-mass peak shifts from $(m_{b,p}, m_{b,s}) \sim (20M_{\odot}, 20M_{\odot})$ to $(m_{b,p}, m_{b,s}) \sim (35M_{\odot}, 35M_{\odot})$ with t_d . The merger rate density is decreased sharply at both the ends of ~ 5 and $50M_{\odot}$. There is no $3 - 5M_{\odot}$ BHs, the so-called “lower mass gap”, since the rapid model never forms BHs in the lower mass gap. The number of BHs in the PI mass gap is quite small due to PPI/PISN effects. A few BHs in the PI mass gap can be formed from stars with light He cores and heavy H envelopes (see Figure 3), or through accretion from their companion stars. These BHs have at most $55M_{\odot}$, while BHs can have $\sim 85M_{\odot}$ if they evolve as single stars (see Figure 3). This is because BH progenitors in binaries are easy to lose their H envelopes through binary interactions.

The higher-mass peak appears due to PPI effects. This peak is not observed in the K14 model which does not account for PPI effects. Stars with He core masses of $45 - 65M_{\odot}$ experience PPI, and are thus swept up together to BHs with $45M_{\odot}$. Since PPI effects are independent of binary star evolution, the higher-mass peak always appears regardless of t_d .

The lower-mass peak has two features; it shifts from $\sim 20M_{\odot}$ to $\sim 35M_{\odot}$, and the mass ratio favors nearly unity. The reasons for the two features can be explained by their formation channels. Here, we first explain the formation channel, and next the reasons for the features. The lower-mass peak is formed through the same mech-

anism as the peak of $\sim 30M_{\odot}$ in the K14 model, i.e. the CE0 channel. The detail processes are as follow. The 1st-evolving star enters into its CHeB phase, fills its Roche lobe, and starts stable mass transfer to the 2nd-evolving star. The mass transfer can keep stable, since a Pop. III star with $M_{\text{ZAMS}} = 10 - 50M_{\odot}$ ends its life with a BSG star (see Figure 1). Subsequently, the 1st-evolving star collapses to a BH. After that, the 2nd-evolving star also fills its Roche lobe, and begins stable mass transfer. Finally, the 2nd-evolving star collapses to a BH.

The reason for the mass ratio of unity is as follows. The 1st mass transfer makes the 2nd-evolving star heavier than the 1st BH. Since mass transfer is more efficient when the donor star is heavier than the accreting star, the 2nd mass transfer continues until the mass ratio of the 2nd-evolving star to the 1st BH becomes close to unity. After that, the 2nd-evolving star collapses to a BH with a similar mass to the 1st BH. Thus, these BH-BHs tend to have the mass ratio of unity.

The reason for the time shift of the lower-mass peak is as follows. The merging timescale through GW radiation is expressed as

$$t_{\text{GW}} = \frac{5}{256} \frac{c^5}{G^3} \frac{a^4}{m_{b,p} m_{b,s} (m_{b,p} + m_{b,s})} g(e) \quad (25)$$

$$g(e) = \frac{(1 - e^2)^{3.5}}{1 + (73/24)e^2 + (37/96)e^4}, \quad (26)$$

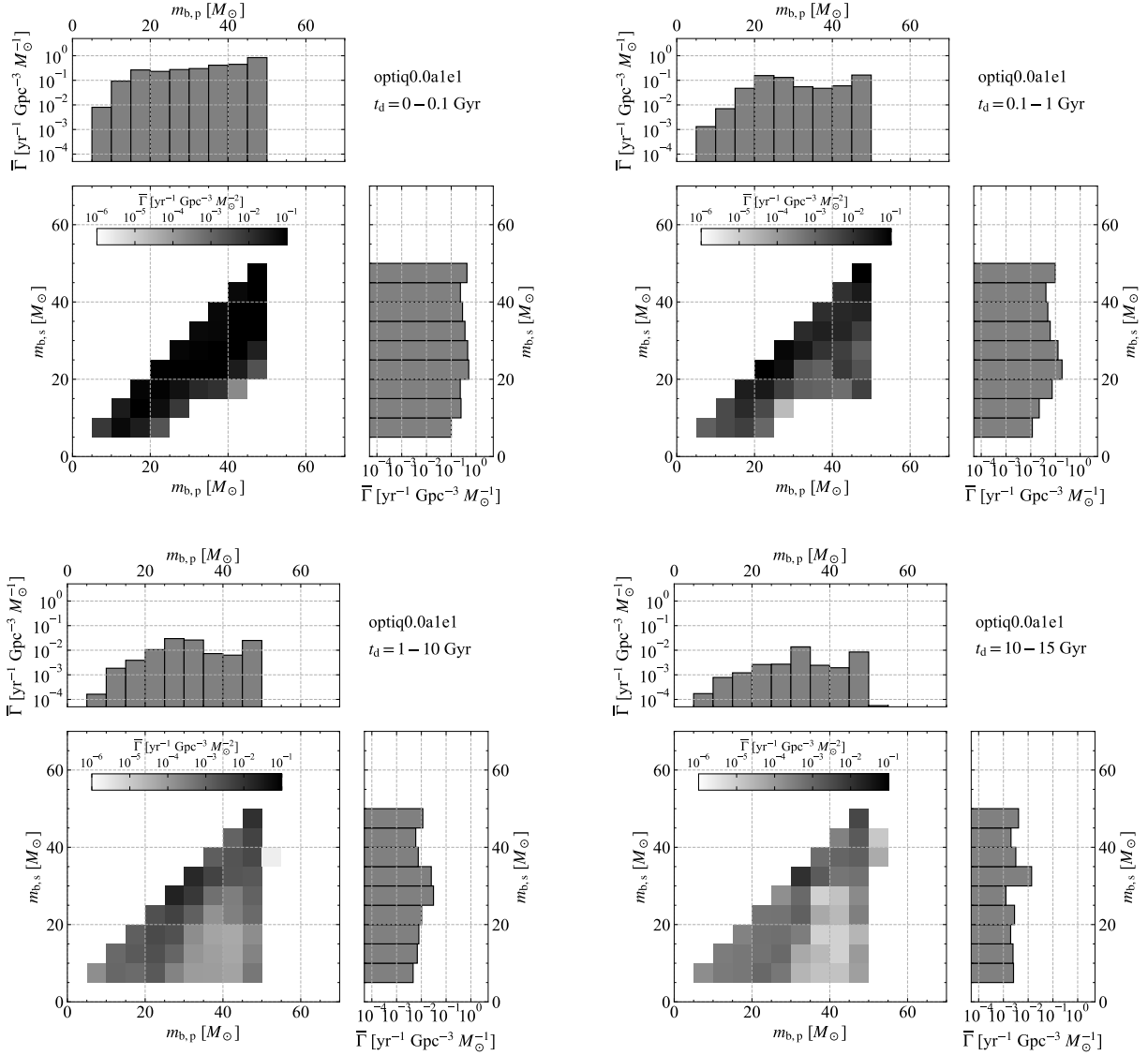


Figure 16. Merger rate densities of hBH0s for $t_d = 0 - 0.1$ (top left), $0.1 - 1$ (top right), $1 - 10$ (bottom left), and $10 - 15$ Gyr (bottom right) in the optiq0.0a1e1 model.

where a and e are the semi-major axis and eccentricity of a BH-BH. Since $m_{b,p} \sim m_{b,s}$ and $e \sim 0$ here, we reduce these equations to $t_{\text{GW}} \propto a^4 m^{-3}$, where we use m instead of $m_{b,p}$ and $m_{b,s}$. The semi-major axis is proportional to the radius of the 2nd-evolving star, $a \propto R_2$, when the 2nd mass transfer occurs. Since $R_2 \propto L_2^{1/2}$, and nearly $L_2 \propto m^2$ for stars with $10 - 50 M_\odot$ in CHeB and ShHeB phases (see Figure 1), $a \propto m$. Finally, $t_{\text{GW}} \propto m$. We now assume that the 2nd-evolving star with different m has the same effective temperature. If we relax this assumption, the 2nd-evolving star with larger m tends to have lower effective temperature for $m \gtrsim 20 M_\odot$ (see Figure 1). Then, t_{GW} can depend on

m more strongly. Thus, the time shift of the lower-mass peak appears.

Figure 17 shows the spin distributions of primary and secondary BHs of hBH0s in the optiq0.0a1e1 model. We can regard that hBH0s with $0 \leq m_{b,p}/M_\odot < 40$ and $40 \leq m_{b,p}/M_\odot < 100$ are associated with populations of the lower-mass and higher-mass peaks, respectively. The top two panels indicate that hBH0s in the lower-mass peak have two BHs with high spins ~ 1 independently of t_d . The reason is as follows. Their progenitors can be highly spun up by tidal fields of their companion stars, since they expand to their Roche-lobe radii. Moreover, they keep their H envelopes more or less until they collapse to BHs.

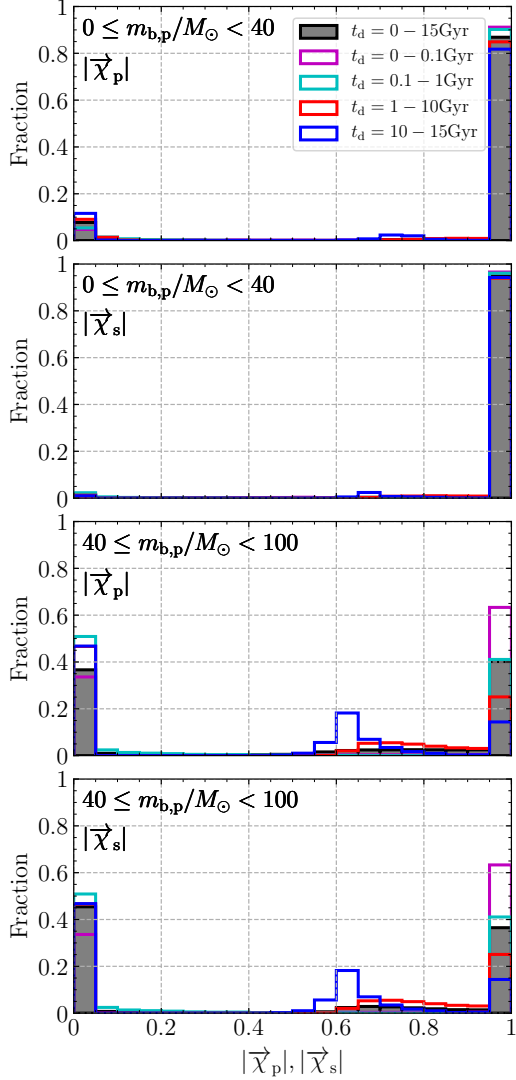


Figure 17. Spin distributions of hBH0s for each t_d in the optiq0.0a1e1 model. The panels indicate primary and secondary BH spins of hBH0 with $0 \leq m_{b,p}/M_\odot < 40$ (the top two panels) and $40 \leq m_{b,p}/M_\odot < 100$ (the bottom two panels).

On the other hand, half of hBH0s in the higher-mass peak have BHs with nearly zero spins. This is due to PPI effects. We assume BH progenitors undergoing PPI lose their spin angular momenta. The other half have high spins with $\gtrsim 0.5$, and however have smaller spins with t_d increasing. The reason for the time dependence is as follows. BH progenitors gain and lose their spin angular momenta through tidal interactions and mass transfer, respectively. As the t_d increases, binary separation becomes larger, and tidal interaction becomes weaker. Thus, a BH progenitor decreases its spin angular momentum in the net, and its BH has a lower spin. The details can be described in many studies (Kushnir

et al. 2016; Hotokezaka & Piran 2017; Piran & Piran 2020; Safarzadeh & Hotokezaka 2020). We call this relation the spin- t_d relation tentatively.

With respect to spins, the hBH0s have four subpopulations; both the BHs have high spins (~ 1), both the BHs have low spins (~ 0), and the 1st (2nd) BH has high spin (~ 1) but the other BH has low spin (~ 0). This is different from the results of Kinugawa et al. (2016c,b). In their model, the hBH0s do not have a subpopulation with the 1st BHs with high spins and the 2nd BHs with low spins. We obtain the subpopulation, since we assume BHs after PPI have zero spins.

Hereafter, we assess the dependence of these features on initial conditions of binaries (q_{\min} and a_{\min}), and single star models (stellar winds and natal kicks). First, we focus on the dependence on initial conditions.

Figure 18 shows merger rate densities of hBH0s in models with different initial conditions from the optiq0.0a1e1 model. We can find peaks at $(m_{b,p}, m_{b,s}) \sim (45M_\odot, 45M_\odot)$ in all the panels. These peaks correspond to the higher-mass peak in the optiq0.0a1e1 model. Even in the optiq0.0a2e2 and optiq0.9a2e2 models, there can be hBH0s with $t_d \leq 15$ Gyr. This is because stars with $M_{\text{ZAMS}} \sim 100M_\odot$ can expand to $\gtrsim 10^3 R_\odot$ (see Figure 1), interact with their companion stars through common envelope evolutions, and leave $45M_\odot$ BHs (see Figure 3). Consequently, the higher-mass peak in the optiq0.0a1e1 model is present regardless of different initial conditions (q_{\min} and a_{\min}).

We cannot find the lower-mass peak in the optiq0.0a2e2 and optiq0.9a2e2 model. In these models, hBH0s with $t_d \leq 15$ Gyr cannot be formed through the CE0 channel. Since the CE0 channel does not reduce binary separations, hBH0s formed through the CE0 channel have binary separations $\gtrsim 100R_\odot$. Their merging timescales through GW radiation are much larger than 15 Gyr. We can find the lower-mass peak in the optiq0.9a1e1 model for $t_d = 10 - 15$ Gyr, which is formed through the same mechanism in the optiq0.0a1e1 model. On the other hand, we cannot find the lower-mass peak in this model for $t_d = 0.1 - 1$ Gyr. Since two stars with similar masses expand on similar timescales, they fill their Roche lobes, and merge when their separation is small. Eventually, the lower-mass peak in the optiq0.0a1e1 model is sensitive to a_{\min} , and its time shift is weak against q_{\min} .

Although the presence of the higher-mass peak is insensitive to initial conditions, spin distributions of hBH0s around the higher-mass peak can be affected by initial conditions. Half of primary and secondary BHs have nearly zero spins in the optiq0.0a1e1 model, while more than half of them have nearly zero spins in the

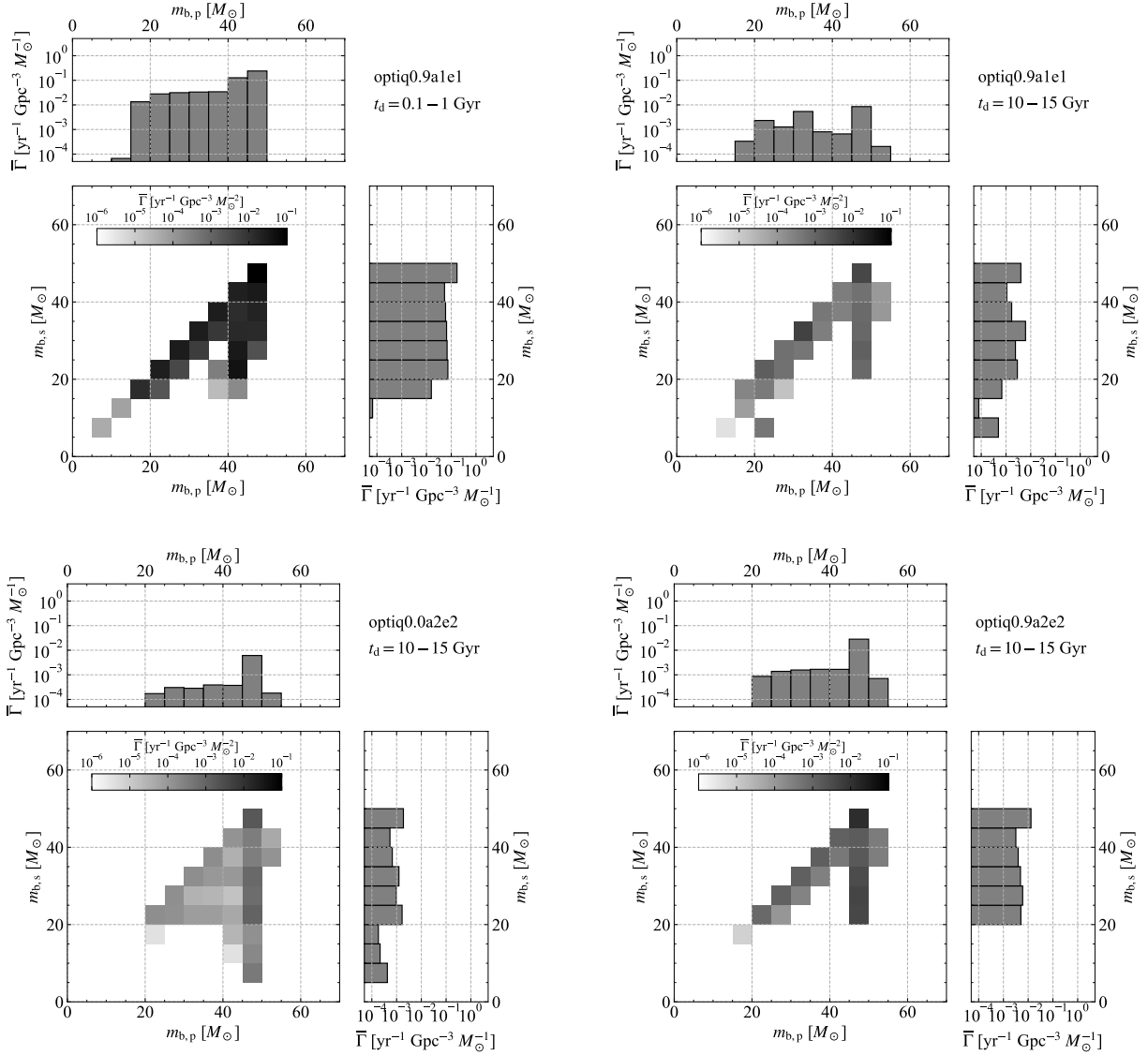


Figure 18. Merger rate densities of hBH0s. The top panels show the results of the optiq0.9a1e1 model for $t_d = 0.1 - 1$ (left) and $10 - 15$ Gyr (right). The bottom panels show the results of the optiq0.0a2e2 (left) and optiq0.9a2e2 models (right) for $t_d = 10 - 15$ Gyr.

other models, and moreover the fraction increases with time up to unity for $t_d = 10 - 15$ Gyr. This is because the CE0 channel has little contribution to the higher-mass peak in the other models. On the other hand, spin distributions of hBH0s around the lower-mass peak are similar between the optiq0.0a1e1 and optiq0.9a1e1 models if the lower-mass peak is present in the optiq0.9a1e1 model.

Next, we focus on the dependence on single star models. Figure 19 shows the merger rate densities of hBH0s in models with different single star models. We can find peaks at $(m_{b,p}, m_{b,s}) \sim (45M_\odot, 45M_\odot)$ in all the panels. These peaks correspond to the higher-mass peak in the

optiq0.0a1e1 model. Therefore, the higher-mass peak is present with or without stellar winds and natal kicks.

The kickq0.0a1e1 model has the lower-mass peak of $(m_{b,p}, m_{b,s}) \sim (30M_\odot, 30M_\odot)$ independently of t_d (see the top panels). In other words, the lower-mass peak has no time shift, unlike in the optiq0.0a1e1 model. This is because natal kicks shorten and lengthen merging timescales of hBH0s, independently of their masses. For example, if a BH progenitor gets a natal kick whose direction is the same as and opposite to its traveling direction, the resulting merging timescale becomes longer and shorter, respectively. Whether the time shift can survive or not depends on the magnitude of natal kicks. We can observe the time shift in the half-kick model, al-

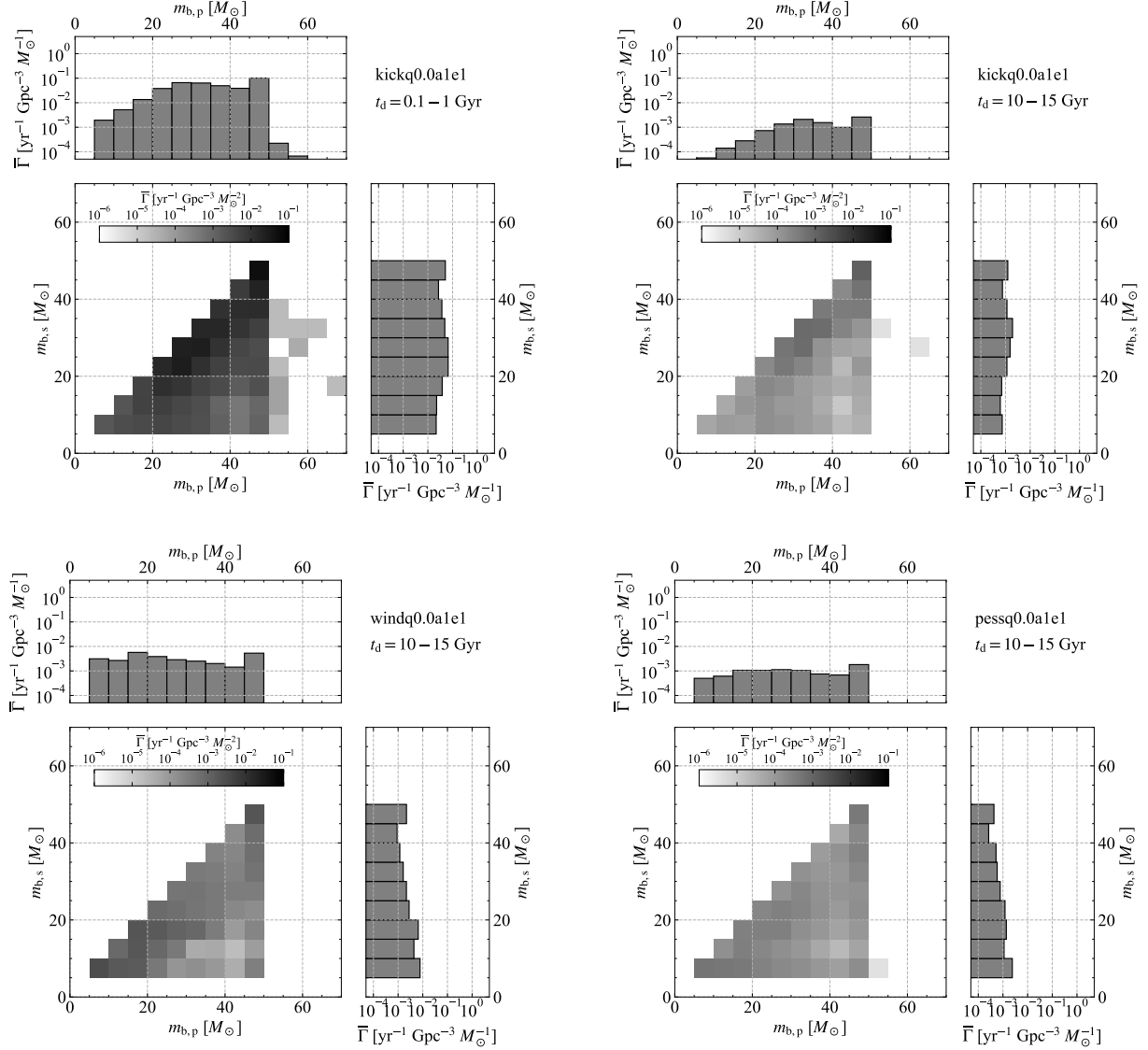


Figure 19. Merger rate densities of hBHOs. The top panels show the results of the kickq0.0a1e1 model for $t_d = 0.1 - 1$ (left) and $10 - 15$ Gyr (right). The bottom panels show the results of the windq0.0a1e1 (left) and pessq0.0a1e1 models (right) for $t_d = 10 - 15$ Gyr.

though it is less distinct than in the optiq0.0a1e1 model. If we assume $\sigma_k = 265 \text{ km s}^{-1}$ for NSs and kick velocities inversely proportional to remnant masses as in the commonly used prescription, the time shift can be seen as prominent as in the optiq0.0a1e1 model, since the kick velocities are $\sim 10 \text{ km s}^{-1}$ for BHs with several $10 M_\odot$.

Stellar winds significantly smooth the lower-mass peak, and shift it to $\sim 20 M_\odot$ (see the bottom panels). The peak shift is simply because BHs lose their masses through stellar winds. This is *not* due to stellar winds of high metallicity, $10^{-3} Z_\odot$. In the weak-wind model ($Z = 10^{-5} Z_\odot$), hBHOs have merger rate densities similar to those in the windq0.0a1e1 model. In fact, rotationally enhanced winds are responsible. If

we switch off the rotationally enhanced winds in the no-rot-wind model, we find the merger rate densities similar to those in the optiq0.0a1e1 model. It is natural that the rotationally enhanced winds have strong effects in models with $a_{\min} = 10 R_\odot$, since most of stars are effectively spun up by tidal fields of their companion stars. Eventually, the lower-mass peak is fragile against stellar winds with rotational enhancement. Although the lower-mass peak is present despite of the presence of natal kicks, its shift with t_d is erased by the natal kicks.

The distribution of spin magnitudes in the kickq0.0a1e1 model is similar to in the optiq0.0a1e1 model for both $0 \leq m_{b,p}/M_\odot < 40$ and $40 \leq m_{b,s}/M_\odot < 100$. On

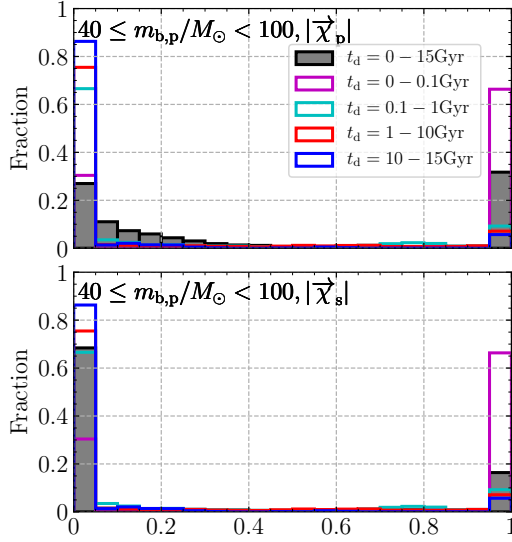


Figure 20. Spin distributions of hBH0s for each t_d in the windq0.0a1e1 model. The panels indicate primary and secondary BH spins of hBH0s with $40 \leq m_{b,p}/M_\odot < 100$.

the other hand, the fraction of hBH0s with nearly zero spins in the windq0.0a1e1 and pessq0.0a1e1 models is 2 times larger than in the optiq0.0a1e1 model for $40 \leq m_{b,s}/M_\odot < 100$ (compare Figure 20 with Figure 17). This is because stellar winds carry away spin angular momenta. We do not show spin distributions of hBH0s for $0 \leq m_{b,p}/M_\odot < 40$ in these models, since the lower-mass peak is weak.

Natal kicks can tilt BH spin vectors from binary orbit vectors of hBH0s. Figure 21 shows the tilt-angle distribution. Note that spin and binary orbit vectors are parallel and anti-parallel for $\cos \theta = 1$ and -1 , respectively. The fractions of $\theta \gtrsim 45^\circ$ and $\gtrsim 90^\circ$ are ~ 0.1 and ~ 0.01 , respectively, for both cases of $m_{b,p}$. Primary BHs have larger tilt angles than secondary BHs. Since primary BHs tend to have 1st-evolving stars as their progenitors, they have two chances to tilt their spin vectors from binary orbit vectors.

We examine mass distribution of hBH0s in “kick”, “wind”, and “pess” models with $q_{\min} \neq 0.0$ or $a_{\min} \neq 10R_\odot$. Then, in all the models, we find peaks corresponding to the higher-mass peak in the optiq0.0a1e1 model. On the other hand, there is no lower-mass peak seen in the optiq0.0a1e1 model. Most of BHs have zero spins for $t_d = 10 - 15$ Gyr. This is because they have large t_d , and because most of them are not formed through the CE0 channel. If some of them were formed through the CE0 channel, there would be the lower-mass peak.

We summarize features of merging hBH0s with $t_d \leq 15$ Gyr. In the optiq0.0a1e1 model, they have

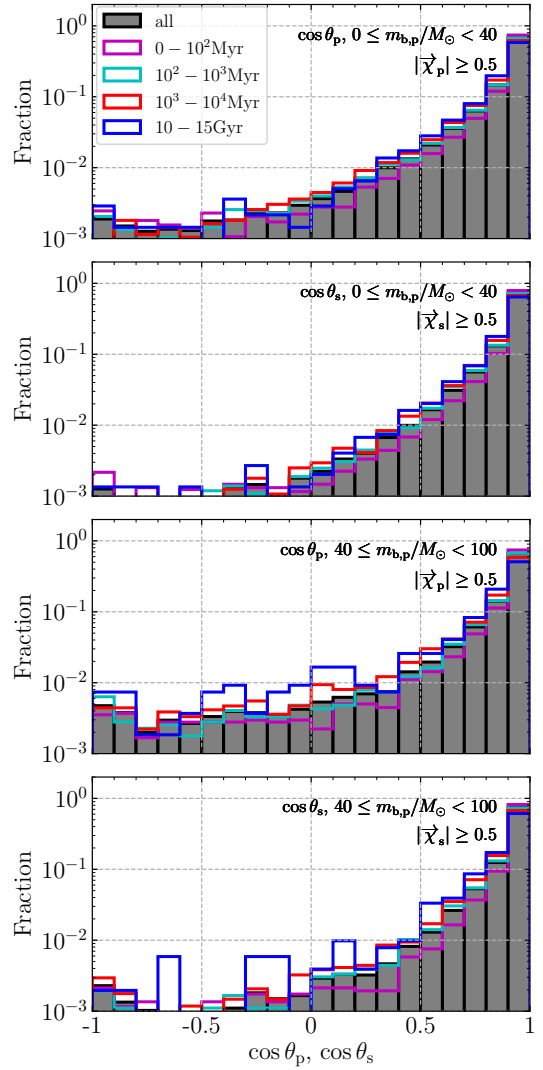


Figure 21. Distribution of angles between primary and secondary BH spin vectors and binary orbit vectors for $0 \leq m_{b,p}/M_\odot < 40$ (the top two panels), and $40 \leq m_{b,p}/M_\odot < 100$ (the bottom two panels) in the kickq0.0a1e1 model. The BHs are limited to those with $|\vec{\chi}_p| \geq 0.5$ or $|\vec{\chi}_s| \geq 0.5$.

two peaks in their mass distribution: $(m_{b,p}, m_{b,s}) \sim (45M_\odot, 45M_\odot)$ (the higher-mass peak) and $(m_{b,p}, m_{b,s}) \sim (30M_\odot, 30M_\odot)$ (the lower-mass peak). The lower-mass peak shifts from $20M_\odot$ to $35M_\odot$ from $t_d = 0.1 - 1$ Gyr to $t_d = 10 - 15$ Gyr. Half (most) of BHs belonging to the higher-mass (lower-mass) peak has significantly high spin. The higher-mass peak is present even in models with different initial conditions (q_{\min} and a_{\min}), and different stellar evolution models (stellar winds and natal kicks, while BHs around the higher-mass peak tend to have zero spins in models other than the optiq0.0a1e1 and kickq0.0a1e1 models due to small contribution of the CE0 channel. The lower-mass peak and

its t_d dependence are quite fragile. It disappears when $a_{\min} = 200R_{\odot}$ or is shifted to $\sim 20M_{\odot}$ by stellar wind effects. Stellar winds have large effects on the lower-mass peak due to the rotational enhancement, not due to the high metallicity. The time-shift feature of the lower-mass peak is erased by natal kicks.

3.3.2. Binaries with high- and low-mass BHs (hBH1s)

First, we investigate the optiq0.0a1e1 model again for the same reason in section 3.3.1. Figure 22 shows the merger rate densities of hBH1s for each t_d . There is no hBH1 with $t_d \lesssim 0.1$ Gyr. Only binaries with $r_{p,i} \gtrsim 10^2 R_{\odot}$ can form hBH1s through the CE1 channel, and their minimum t_d is ~ 0.1 Gyr. On the other hand, a binary with $r_{p,i} \lesssim 10^2 R_{\odot}$ experiences merger when the 1st-evolving star fills its Roche lobe for the reason described in section 3.3.

For $t_d = 0.1 - 15$ Gyr, the $m_{b,p}$ distribution has a plateau in $m_{b,p} \sim 130 - 180M_{\odot}$, and has a tail in $m_{b,p} \sim 180 - 200M_{\odot}$. The plateau ranges from the minimum He core mass needed for the direct collapse ($M_{c,He,DC} = 135M_{\odot}$) to the He core mass of a star with $M_{ZAMS} = 300M_{\odot}$, the maximum mass of $m_{1,i}$ in our models. The merger rate density of $\sim 130M_{\odot}$ should be larger than that of $\sim 180M_{\odot}$, since the $m_{1,i}$ distribution is top-light ($\propto m_{1,i}^{-1}$). Nevertheless, the number of stars forming $M_{c,He} \sim 180M_{\odot}$ ($m_{1,i} \sim 300M_{\odot}$) is comparable to that of stars forming $M_{c,He} \sim 135M_{\odot}$ ($m_{1,i} \sim 250M_{\odot}$). This is because the number ratio of the former star to the latter star is only ~ 1.2 . The tail is formed through stable mass transfer from the 2nd-evolving stars to the 1st BH (see Figure 12). The tail is more prominent in smaller t_d , since the 2nd-evolving stars are closer to the 1st BH, and give larger mass to the 1st BH.

The $m_{b,s}$ distribution has a peak at $25 - 40M_{\odot}$, and the peak shifts from $25M_{\odot}$ to $40M_{\odot}$ with t_d . This is the back reaction of the formation of the $m_{b,p}$ tail. As the 2nd-evolving stars, progenitors of the 2nd BHs, give larger masses to the 1st BH, they lose their masses.

We describe the three features of hBH1s: no merger for $t_d \lesssim 0.1$ Gyr, the $m_{b,p}$ distribution with the plateau and tail, and the $m_{b,s}$ distribution with the peak and its shift with t_d . Hereafter, we investigate the dependence of these features on initial conditions (q_{\min} and a_{\min}) and single star models (stellar winds and natal kicks). Actually, these features are insensitive to a_{\min} . As seen in Figure 11, hBH1s can be formed through the CE1 channel even if binaries have $a_i \gtrsim 200R_{\odot}$. On the other hand, the formation of hBH1s is seriously affected by q_{\min} . For $q_{\min} = 0.9$, hBH1s are never formed (see Figures 9 and 10). Since a binary has stars with similar masses, it cannot form one lBH and one hBH.

Natal kicks again erase t_d dependence. In the kickq0.0a1e1 model, hBH1s with $t_d \lesssim 0.1$ Gyr appear, and the time shift of the peak in the $m_{b,s}$ distribution disappears. The $m_{b,s}$ peak is always at $\sim 30M_{\odot}$. Stellar winds also affect the mass distribution. The $m_{b,p}$ distribution also has the plateau for the following reason. The 1st-evolving stars always become nHe stars regardless of the presence and absence of stellar winds due to the CE1 channel. The nHe stars lose little mass through stellar winds, since they do not exceed the Eddington limit, and are not sufficiently spun up. However, the tail disappears for the following reason. The 2nd-evolving stars are strongly spun up by the 1st-evolving star or 1st BH after the CE1 channel. Then, they lose a significant part of their H envelopes through stellar winds as seen in Figure 3. Thus, they cannot transfer their masses to the 1st BHs. The $m_{b,s}$ distribution is sensitive to the stellar winds, since the 2nd-evolving stars are spun up and lose their mass rotationally enhanced stellar winds as described above. Then, the peak of $m_{b,s}$ moves down to $\sim 20M_{\odot}$. In the other models, we find that mass distributions can be explained by simple combinations of initial conditions, natal kicks and stellar winds.

Figure 23 shows the spin distributions of BHs in hBH1s. The fraction of primary BHs with nearly zero spins increases with t_d . The fraction of $|\vec{\chi}_p| \lesssim 0.2$ reaches to ~ 1 for $t_d = 10 - 15$ Gyr. This can be also explained by the spin- t_d relation described in section 3.3.1. On the other hand, the secondary BHs have high spins ~ 1 for all t_d . This is because they are spun up by tidal fields of the 1st BHs, and keep their H envelopes.

The spin distribution is insensitive to a_{\min} for the same reason as the mass distribution. Natal kicks erase the t_d dependence, and average the distribution to that for $t_d = 0 - 15$ Gyr. This is because natal kicks shorten and lengthen t_d at random as described in section 3.3.1. Figure 24 shows the spin distributions of BHs in hBH1s in the windq0.0a1e1 model. Stellar winds largely reduce spins for both the primary and secondary BHs. Although the fraction of non-spinning BHs for $t_d = 10 - 15$ Gyr in the pessq0.0a1e1 model is smaller than in the windq0.0a1e1 due to natal kicks, the fraction is still high (~ 0.6) for both the primary and secondary BHs.

Figure 25 shows the distribution of angles between primary and secondary BH spin vectors and binary orbit vectors for hBH1s in the kickq0.0a1e1 model. The angles are formed only due to natal kicks. Comparing Figure 25 with Figure 21, we can find that spins of hBH1s are more aligned than those of hBH0s. This is not due to the small number of hBH1s, although the number of BHs in the top panel of Figure 25 is $\sim 10^3$ of 10^6 binaries,

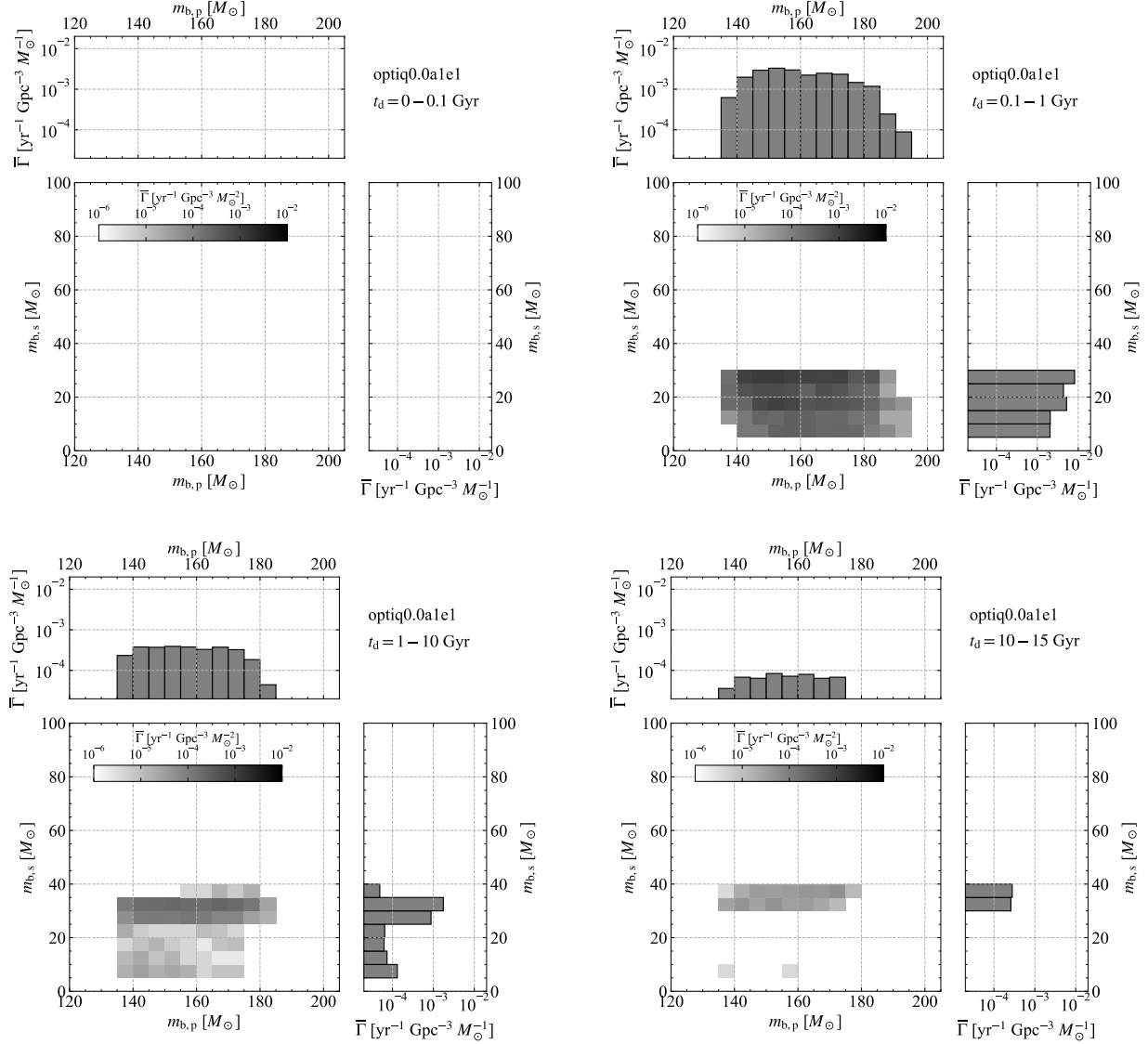


Figure 22. Merger rate densities of hBHs in the optiq0.0a1e1 model.

and that in the top panel of Figure 21 is $\sim 3 \times 10^4$ of 10^6 binaries. For example, the fraction of $\theta \gtrsim 45^\circ$ is a few 0.01 for hBH1s, while it is ~ 0.1 for hBH0s. This reason can be interpreted as follows. We can obtain the circular velocity of a BH-BH, rewriting Eq. (25) as

$$v_{\text{circ}} \propto t_{\text{GW}}^{-1/8} m_{\text{b,p}}^{-1/8} m_{\text{b,s}}^{-1/8} (m_{\text{b,p}} + m_{\text{b,s}})^{3/8}. \quad (27)$$

As seen in Eq. (27), the internal velocity of a BH-BH becomes larger with its total mass, if t_{GW} is fixed. Thus, BH-BHs with larger total masses are less sensitive to natal kicks. This is the reason why spins of hBH1s are more aligned than those of hBH0s.

We summarize features of merging hBH1s. We first see the optiq0.0a1e1 model. They merge for $t_d \gtrsim 0.1$ Gyr. The $m_{\text{b,p}}$ distribution has a plateau in 130 –

180 M_\odot and a tail in 180 – 200 M_\odot . The tail is more prominent in smaller t_d . The $m_{\text{b,s}}$ distribution has a peak shifting from 20 M_\odot to 40 M_\odot with t_d . The fraction of hBH1s with $|\vec{\chi}_p| \lesssim 0.2$ increases with t_d , and reaches to unity for $t_d = 10 - 15$ Gyr, while the fraction of hBH1s with $|\vec{\chi}_s| \sim 1$ is unity for all t_d .

The above features are changed by various effects. First, hBH1s themselves vanish if $q_{\text{min}} = 0.9$. The above features have weak dependence on a_{min} . Natal kicks erase the t_d dependence, and raise spin-orbit misalignments smaller than those of hBH0s. Stellar winds erase the tail of the $m_{\text{b,p}}$ distribution, and reduce the peak location of the $m_{\text{b,s}}$ distribution to $\sim 20 M_\odot$. Moreover, stellar winds greatly increase the fraction of hBH1s with $|\vec{\chi}_p| \sim 0$ and $|\vec{\chi}_s| \sim 0$.

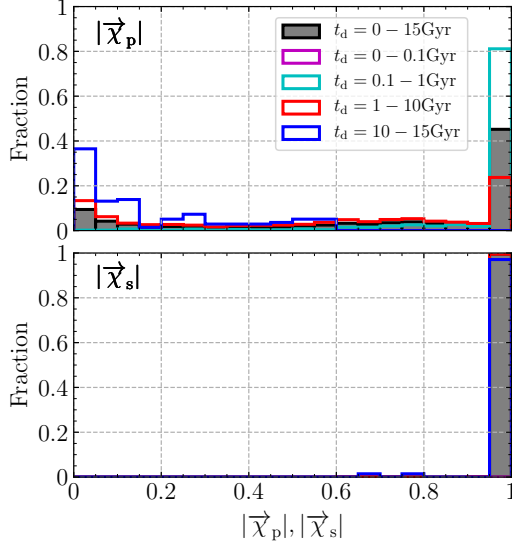


Figure 23. Spin distributions of primary and secondary BHs in hBH1s for each t_d in the optiq0.0a1e1 model.

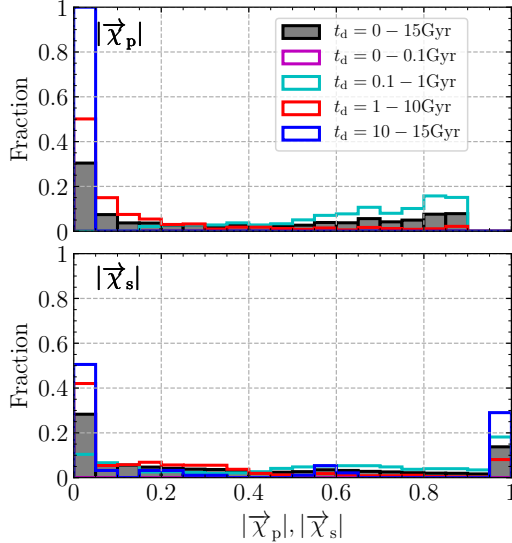


Figure 24. Spin distribution of primary and secondary BHs in hBH1s for each t_d in the windq0.0a1e1 model.

3.3.3. Binaries with two high-mass BHs (hBH2s)

We first investigate the optiq0.0a1e1 model, similarly to the previous sections. Figure 26 shows the merger rate density of hBH2s for each t_d . The 2D distribution for $t_d = 0 - 0.1$ Gyr has a triangle shape ($m_{b,p} \lesssim 180 M_\odot$), while those for $t_d = 0.1 - 15$ Gyr have a parallelogram shape ($m_{b,p} \lesssim 200 M_\odot$). Their different shapes are due to the difference between their formation channels. For $t_d \lesssim 0.1$ Gyr, they are formed through the CE4 channel (see also Figure 11). This is the reason why the $m_{b,p}$ distribution is flat in $130 - 180 M_\odot$, the same reason for the plateau of the primary BHs in

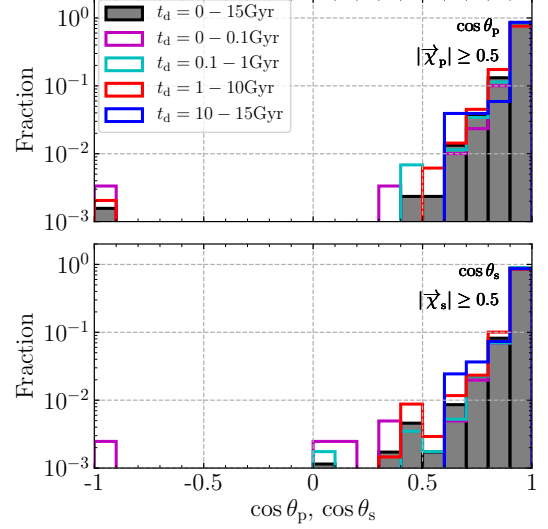


Figure 25. Distribution of angles between primary and secondary BH spin vectors and binary orbit vectors for hBH1s in the kickq0.0a1e1 model. The BHs are limited to those with $|\vec{\chi}_p| \geq 0.5$ or $|\vec{\chi}_s| \geq 0.5$.

hBH1s described in section 3.3.2. The $m_{b,s}$ distribution monotonically decreases with $m_{b,s}$. In our initial conditions, as the 2nd-evolving stars become more massive, they have less chances to have the 1st-evolving stars with $M_{\text{ZAMS}} = 250 - 300 M_\odot$ which overcome PISN. For $t_d \gtrsim 0.1$ Gyr, hBH2s are formed through the CE0 channel (see also Figure 11). This is the reason why the primary BHs can have larger masses than He core masses formed from stars with $M_{\text{ZAMS}} = 300 M_\odot$. The 2D distributions have shapes like parallelograms. This means hBH2s have two BHs with similar masses. This is because the 2nd mass transfer tends to stop when a mass ratio of the binary becomes close to unity, similarly to hBH0s around the lower-mass peak in the optiq0.0a1e1 model.

For $q_{\min} = 0.9$ or $a_{\min} = 200 R_\odot$, the mass distributions in all t_d are similar to that in $t_d \lesssim 0.1$ Gyr in the optiq0.0a1e1 model. In other words, all the hBH2s are formed only through the CE4 channel. This is because the CE0 channel does not work. As seen in Figure 11, the CE0 channel works well only when $q_i < 0.9$ (the top panel) and $a_i < 200 R_\odot$ (the left-hand side of the vertical dashed line). For $q_i \geq 0.9$, two stars fill their Roche lobes simultaneously. Then, they experience merger or common envelope evolution. They merge when they are MS stars, and they experience common envelope evolution when they are post-MS stars. Thus, they cannot undergo the CE0 channel. For $a_i \geq 200 R_\odot$, binaries can undergo the CE0 channel. However, the resulting BH-BHs have too large separations to merge for $t_d \leq 15$ Gyr,

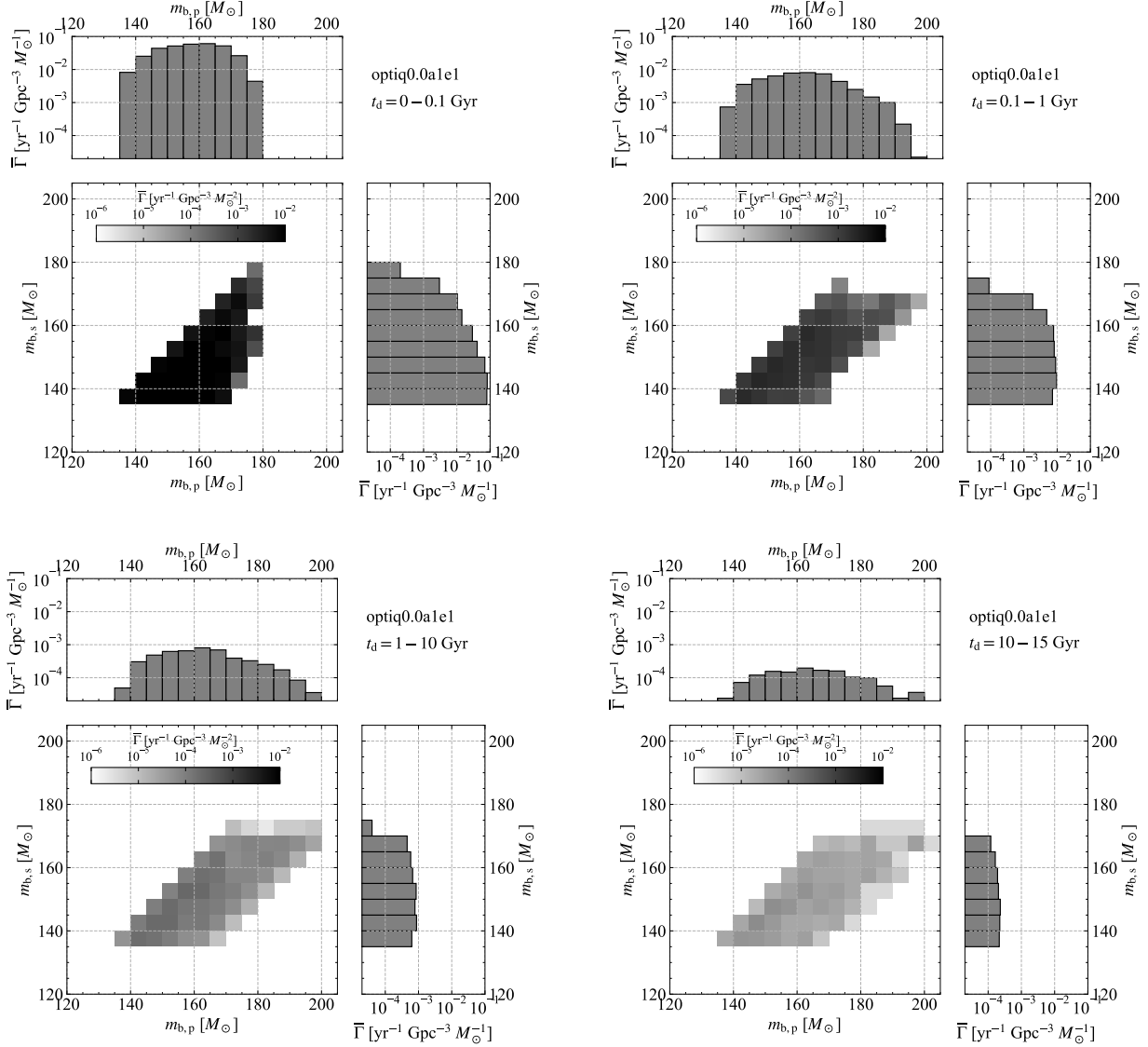


Figure 26. Merger rate densities of hBH2s in the optiq0.0a1e1 model.

since the CE0 channel does not shrink binary separations.

Natal kicks erase the t_d dependence. Thus, hBH2s formed through the CE0 channel appear for $t_d \lesssim 0.1$ Gyr, and the 2D distributions have shapes like parallelograms for all t_d . Stellar winds erase hBH2s formed through the CE0 channel. The 1st-evolving star fills its Roche lobe when it is an MS star. It is spun up, and loses large mass due to rotationally enhanced stellar winds. Since it makes a He core with smaller mass than $M_{\text{c,He,DC}} (= 135 M_\odot)$ due to the stellar winds, it experiences PISN. Thus, the shapes of the 2D distributions for all t_d are triangle-like, similar to that for $t_d = 0 - 0.1$ Gyr in the optiq0.0a1e1 model. This is the same if both of natal kicks and stellar winds are

taken into account (i.e. the pess models). The mass distributions in models with different initial conditions and single star models can be understood as simple combinations of the effects described above.

Figure 27 shows the spin distribution of primary and secondary BHs of hBH2s in the optiq0.0a1e1 model. The fraction of BHs with high spins decreases with t_d because of the spin- t_d relation. A large number of BHs have low spins, ~ 0.2 for $t_d = 10 - 15$ Gyr. Note that their spins are non-zero. Since they are formed through the CE0 channel, they can retain their H envelopes and spin angular momenta until their collapses.

Different initial conditions make the spin distribution smaller, especially for $t_d = 10 - 15$ Gyr. Figure 28 shows the spin distribution of hBH2s in optiq0.0a2e2 model.

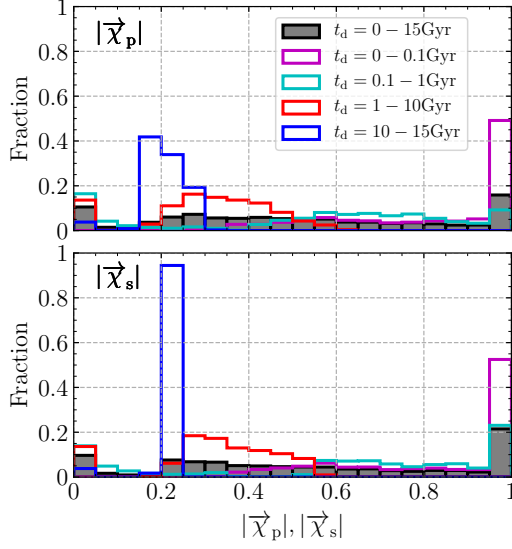


Figure 27. Spin distributions of hBH2s for each t_d in the optiq0.0a1e1 model.

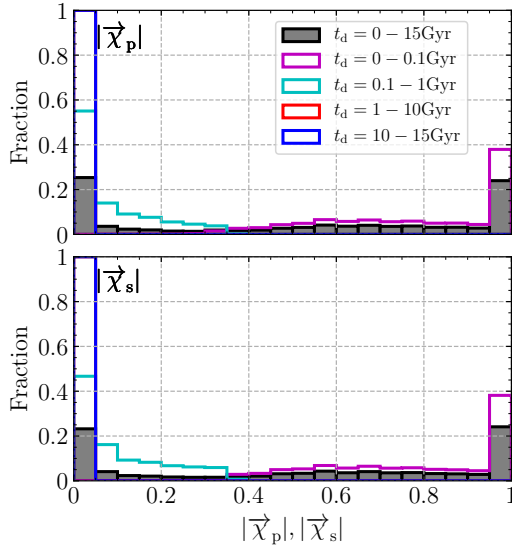


Figure 28. Spin distributions of hBH2s for each t_d in the optiq0.0a2e2 model.

Most of primary and secondary BH spins are zero for $t_d = 10 - 15$ Gyr in contrast to those in the optiq0.0a1e1 model. This is because hBH2s for $t_d = 10 - 15$ Gyr are formed only through the CE4 channel. Note that the corresponding hBH2s in the optiq0.0a1e1 model are formed dominantly through the CE0 channel. Since the CE4 channel carries away H envelopes of progenitors of both primary and secondary BHs, the resulting BHs have lower spins than BHs formed through the CE0 channel.

Natal kicks erase the t_d dependence of the spin distribution, and the spin distribution for each t_d is similar

to that for $t_d = 0 - 15$ Gyr. Stellar winds decrease spins of both the primary and secondary spins. Most of BH spins are zero for $t_d = 10 - 15$ Gyr. When both of initial conditions and single star models are different from the optiq0.0a1e1 model, we can interpret the spin distributions as simple combinations of the effects described above.

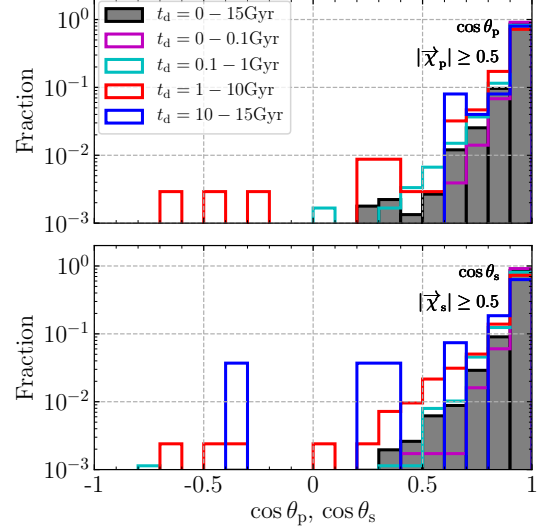


Figure 29. Distribution of angles between primary and secondary BH spin vectors and binary orbit vectors for hBH2s in the kickq0.0a1e1 model. The BHs are limited to those with $|\vec{\chi}_1| \geq 0.5$ or $|\vec{\chi}_2| \geq 0.5$.

Natal kicks raise spin-orbit misalignments of hBH2s. We show in Figure 29 the distribution of the misalignments. The misalignments are clearly weaker than those of hBH0s (see Figure 21) because of their larger internal velocities as discussed in section 3.3.2. However, the misalignments appear similar to those of hBH1s (see Figure 25). There can be two reasons. First, the difference between internal velocities of hBH1s and hBH2s is smaller than the difference between internal velocities of hBH0s and hBH1s. Second, the numbers of hBH1s and hBH2s are small, $\sim 10^3$ of 10^6 binaries.

We summarize the features of hBH2s. In the optiq0.0a1e1 model, they are formed through the CE0 and CE4 channels. The CE4 and CE0 channels are dominant for $t_d = 0 - 0.1$ and $0.1 - 15$ Gyr, respectively. Thus, the mass distribution is limited to He core masses in $130 - 180 M_\odot$ for $t_d = 0 - 0.1$ Gyr, while it extends to $\sim 200 M_\odot$, since BHs keep their H envelopes. The 2D mass distributions have a triangle-like shape for $t_d = 0 - 0.1$ Gyr, and parallelogram-like shapes for $t_d = 0.1 - 15$ Gyr. Primary and secondary BH spins decrease with t_d due to the spin- t_d relation, and they have only ~ 0.2 for $t_d = 10 - 15$ Gyr. If initial conditions are

different or stellar winds are switched on, hBH2s formed through the CE0 channel vanish. Their mass distributions for all t_d have triangle-like shapes, similar to those for $t_d = 0 - 0.1$ Gyr in the optiq0.0a1e1 model. BH spins decrease with t_d , and most of them are zero for $t_d = 10 - 15$ Gyr. Natal kicks erase the t_d dependence, and raise spin-orbit misalignments smaller than those of hBH0s, and similar to those of hBH1s. Mass and spin distributions with different initial conditions and single star models can be interpreted as simple combinations of their effects.

4. IDENTIFICATION OF POP. III BH-BHS

We discuss possibility to identify Pop. III BH-BHs by the current and future GW observatories. In section 4.1, we compare our results with previous events of BH-BH mergers, and present clues to identify Pop. III BH-BHs if Pop. III BH-BHs are contained in previous and near-future events detected by the current GW observatories. In section 4.2, we examine how to find Pop. III BH-BHs by future GW observatories. Figures 14 and 15 will be helpful also in this section.

4.1. Current GW observatories

In sections 4.1.1 and 4.1.2, we discuss about hBH0s and hBH1s/hBH2s, respectively.

4.1.1. Binaries with two low-mass BHs (hBH0)

As described above, the merger rate of Pop. III BH-BHs at the present day (or $t_d \sim 10$ Gyr) is $\sim 0.1 \text{ yr}^{-1} \text{ Gpc}^{-3}$, much smaller than inferred by LIGO/Virgo observations by two or three orders of magnitude. However, the merger rate density of Pop. III BH-BHs should be largely influenced by the total mass density of Pop. III stars, which contains large uncertainties. Hereafter, we compare Pop. III hBH0's mass and spin distributions with observed BH-BHs. These distributions should not be affected by the total mass density of Pop. III stars.

Here, we focus on the lower-mass ($\sim 30M_\odot$) peak of Pop. III hBH0s. As seen in Figure 15, a high fraction of hBH0s have high χ_{eff} if the peak is present. Since this peak is unique to Pop. III hBH0s, it can be a clue to identify Pop. III BH-BHs. We do not mention the higher-mass ($\sim 45M_\odot$) peak despite that it is present regardless of different initial conditions (q_{min} and a_{min}) and different stellar evolution models (stellar winds and natal kicks). This is because it is also predicted for Pop. I/II hBH0s.

We compare the $m_{b,p}$ distributions for $t_d = 10 - 15$ Gyr with observed BH-BHs. From GW observations, Abbott et al. (2020d) have inferred that the merger rate

density has a global maximum at $7.8^{+2.2}_{-2.1} M_\odot$. No model in this paper indicates such a global maximum as seen in Figures 16, 18, and 19. Pop. III binaries may not cover all BH-BHs observed by the current GW observatories.

We examine whether Pop. III binaries can explain a possible subcomponent of currently observed BH-BHs. Here, we focus on a peak at $30 - 40M_\odot$ in the merger rate density shown by GW observations (Abbott et al. 2020d). If we increase the total mass density of Pop. III stars by $30 - 100$ times, Pop. III merger rate density at the lower-mass peak (see Figure 16) can be matched with observed BH-BH merger rate density around at $\sim 30M_\odot$ ($\sim 0.3 \text{ yr}^{-1} \text{ Gpc}^{-3} M_\odot^{-1}$). However, most of observed BH-BHs have $\chi_{\text{eff}} \lesssim 0.4$ (Abbott et al. 2020d), while most of Pop. III hBH0s around at the lower-mass peak have $\chi_{\text{eff}} \sim 1$. It may be difficult to claim that the observed $30 - 40M_\odot$ peak is formed from Pop. III hBH0s. Note that BH spins can depend on models of tidal interaction and mass transfer (Kinugawa et al. 2020a).

Hereafter, we assess whether Pop. III hBH0s can explain rare events discovered in the first half of the third observing run by LIGO and Virgo. The rare events are GW 190412, GW 190814, and GW 190521.

GW 190412 has $m_{b,p} \sim 30M_\odot$, $m_{b,s} \sim 8M_\odot$, $\chi_{\text{eff}} \sim 0.28$, and $|\vec{\chi}_p| \sim 0.31$ (Abbott et al. 2020a). Some studies have pointed out that the secondary BH may have high spin, and the primary BH may not have high spin (e.g. Olejak et al. 2020; Safarzadeh & Hotokezaka 2020). On the other hand, reanalysis by Zevin et al. (2020) have supported that the primary BH is a spinning BH. In either case, Pop. III hBH0s in our results cannot explain this event, since Pop. III hBH0s with $m_{b,p} \sim 30M_\odot$ should have high spins (but see Kinugawa et al. 2020a).

Our supernova model is the rapid model in which BHs in the lower-mass mass gap are not formed. Thus, our models have no hBH0 like GW 190814 that contains a $2.6M_\odot$ compact object (Abbott et al. 2020c). Kinugawa et al. (2020c) have chosen a supernova model with the lower mass gap, and have suggested that GW 190814-like events can happen under Pop. III environments.

GW 190521 has $m_{b,p} \sim 85M_\odot$ and $m_{b,s} \sim 66M_\odot$ (Abbott et al. 2020b). Unfortunately, our models cannot form mass combinations like GW 190521 as seen in Figure 8 (but see Farrell et al. 2020; Kinugawa et al. 2020b; Safarzadeh & Haiman 2020; Liu & Bromm 2020b; Tanikawa et al. 2020b). However, GW 190521 may be interpreted as a BH-BH with hBH and lBH (Fishbach & Holz 2020; Nitz & Capano 2020). We discuss about the possibility that GW 190521 may be a Pop. III hBH1 in Section 4.1.2.

We summarize this section. We compare Pop. III hBH0s with observed BH-BHs. Even if we match the merger rate density of Pop. III hBH0s with that of observed BH-BHs by increasing the Pop. III formation rate by two or three orders of magnitude, Pop. III hBH0s cannot explain a global maximum at $\sim 8M_{\odot}$ in observed BH-BHs. The $\sim 30M_{\odot}$ peak of Pop. III hBH0s may not be consistent with that of observed BH-BHs, since Pop. III hBH0s have much higher spins than observed ones. GW 190412 and GW 190814 are unlikely to be Pop. III hBH0s according to our Pop. III models.

4.1.2. Binaries including hBHs (hBH1 and hBH2)

María Ezquiaga & Holz (2020) have shown that the current GW observatories are most sensitive to BH-BHs with the total masses of $\sim 200M_{\odot}$, which is similar to the total masses of hBH1s and hBH2s. Hence, we discuss about properties of Pop. III hBH1s and hBH2s, and their difference from others. We focus on the characteristic features of Pop. III hBH1 and hBH2 weakly depending on initial conditions (q_{\min} and a_{\min}) and stellar evolution models (stellar winds and natal kicks), as described in Figure 15.

First, we compare Pop. III BH-BHs with those in globular clusters (GCs) (Rodríguez et al. 2019; Kimball et al. 2020), nuclear star clusters (NSCs) at galactic centers (Antonini & Rasio 2016; Belczynski & Banerjee 2020), open clusters (OCs) (Di Carlo et al. 2020a; Banerjee 2019), and triple and quadruple systems (TS and QS, respectively) (Fragione et al. 2020). In these scenarios, hBHs grow through stellar or BH mergers. Since these mergers should not be frequent, the ratio of hBHs to IBHs should not be high. Thus, the ratio of hBH2s to hBH1s should be much smaller than the Pop. III ratio. Many discoveries of hBH1s and hBH2s can distinguish Pop. III ones from the other ones. Moreover, Since GC- and NSC-origin ones involve BH mergers, most of them should have high χ_{eff} . On the other hand, at least half of Pop. III ones have low χ_{eff} .

Gas accretion can increase BH masses up to the mass range of hBHs (e.g. Roupas & Kazanas 2019). This should make hBHs highly spinning. Thus, hBH1s and hBH2s in this scenario should have high χ_{eff} . On the other hand, at least half of Pop. III hBH1s and hBH2s have low χ_{eff} . Thus, they can be identified from those formed through gas accretion.

We compare our BH-BHs with Pop. III BH-BHs formed dynamically (Liu & Bromm 2020a). Their BH-BHs have $m_{\text{b,p}} \gtrsim 250M_{\odot}$ in contrast to our BH-BHs with $m_{\text{b,p}} \gtrsim 130M_{\odot}$. This is because each BH evolves as a single star, and do not lose its mass through binary interactions, such as mass transfer, common envelope,

and rotationally enhanced stellar winds. Their BH-BHs should have high χ_{eff} different from Pop. III BH-BHs, since it gets extra mass through gas accretion. Eventually, by hBH masses and spins, we can distinguish whether Pop. III BH-BHs are formed through binary evolution or dynamical interaction.

Mangiagli et al. (2019) have examined merger rates of Pop. I/II hBH1s and hBH2s. Their merger rates are $\sim 10^{-2} \text{ yr}^{-1} \text{ Gpc}^{-3}$, comparable with merger rates of Pop. III hBH1s and hBH2s we estimate. It may be difficult to distinguish Pop. III hBH1s and hBH2s from Pop. I/II ones if we confine ourselves to discussing about merger events in the current universe. Although Mangiagli et al. (2019) have not presented detail properties, such as $m_{\text{b,p}}$, $m_{\text{b,s}}$, $\vec{\chi}_{\text{p}}$, and $\vec{\chi}_{\text{s}}$ distribution, these properties may be similar among Pop. I/II/III hBH1s and hBH2s, since all of them are formed through binary evolution.

Liu et al. (2019) (see also Liu et al. 2020b) have discovered a $70M_{\odot}$ BH in LB-1, and have raised the possibility that massive BHs can be formed more easily than previously thought (Groh et al. 2020; Belczynski et al. 2020b). Then, Pop. I/II hBH1s and hBH2s may be also formed more easily. However, there are many opposite opinions against the presence of a $70M_{\odot}$ BH in LB-1 (Irrgang et al. 2020; Simón-Díaz et al. 2020; El-Badry & Quataert 2020b,a; Yungelson et al. 2020; Abdul-Masih et al. 2020; Eldridge et al. 2020; Tanikawa et al. 2020a; Bodensteiner et al. 2020). Thus, we do not take into account the possibility here.

Finally, we discuss about GW 190521. Fishbach & Holz (2020) and Nitz & Capano (2020) have suggested that GW 190521 may be a hBH1. Nitz & Capano (2020) have also indicated that the heavier BH is most likely to have high spin magnitude, and large spin-orbit misalignment ($\gtrsim 90^\circ$). Pop. III hBH1s are difficult to explain the spin features of GW 190521. If we include BH natal kicks, hBHs in hBH1s can have high spins even in the current universe, since BH natal kicks relaxes the spin- t_{d} relation. However, their spin-orbit misalignments are $\lesssim 60^\circ$ (see Figure 25). We have to adopt $\sigma_{\text{k}} \gg 265 \text{ km s}^{-1}$ for BH natal kicks in order to form Pop. III hBH1s with spins as large as GW 190521.

We summarize this section. Pop. III BH-BHs with hBHs (hBH1s and hBH2s) can be identified from those formed through stellar or BH mergers in GCs, NSCs, OCs, and TS/QSs, or through gas accretion by the ratio of hBH1s to hBH2s and hBH spins. On the other hand, it is difficult to distinguish between Pop. III and Pop. I/II BH-BHs. Although GW 190521 may consist of hBH and IBH similar to Pop. III hBH1s, the spin-orbit misalignment of GW 190521 cannot be explained

by Pop. III hBH1s, unless we adopt BH natal kicks with $\sigma_k \gg 265 \text{ km s}^{-1}$.

4.2. Future GW observatories

Future ground-based GW observatories, such as Einstein telescope (Punturo et al. 2010; Maggiore et al. 2020) and Cosmic explorer (Reitze et al. 2019), can detect hBH0s at the high-redshift universe. Moreover, future space-borne GW observatories, such as DECIGO (Kawamura et al. 2006), may observe hBH1s and hBH2s at the high-redshift universe. In this section, we discuss about the t_d dependence of Pop. III hBH0s, hBH1s, and hBH2s, and suggest clues to identify Pop. III BH-BHs from other BH-BHs.

First, we state a unique feature to Pop. III BH-BHs, which are common with Pop. III hBH0s, hBH1s, and hBH2s. Since Pop. III stars are formed much earlier than Pop. I/II stars, Pop. III BH-BHs can be observed at the higher-redshift universe (say $z \sim 10$) than Pop. I/II BH-BHs ($z \sim 2$, when stars are most actively formed (Madau & Dickinson 2014)). If Pop. III BH-BHs dominate observed BH-BHs contrary to our results, the BH-BH merger rate density should have $\Gamma \propto t_d^{-1}$ beyond $z \sim 2$ regardless of initial conditions and stellar models (see Figure 9).

Pop. III hBH0s have two time-evolving features in the optiq0.0a1e1 model (see also Figure 14):

- Time evolution of the lower-mass peak in BH mass distribution from $20M_\odot$ to $35M_\odot$.
- High fraction of high effective spins (~ 1) around at the lower-mass peak.

These features can be strong evidence for the presence of Pop. III BH-BHs, even if Pop. III BH-BHs are not dominant GW sources. This t_d dependence is quite different from BH-BHs formed in other places. Santoliquido et al. (2020) do not find the cosmic evolution of mass distributions of BH-BHs formed through binary evolution and open clusters. Although BH-BH masses can evolve if GC-origin BH-BHs are dominant, their masses should decrease with time, since more massive BHs join in BH-BHs and merge at an earlier time (e.g. Tanikawa 2013).

Pop. III hBH1s and hBH2s have two time-evolving features in the optiq0.0a1e1 model (see also Figure 14):

- Decreasing of the maximum $m_{b,p}$ with t_d for hBH1s.
- Larger maximum $m_{b,p}$ mass for $t_d \gtrsim 0.1 \text{ Gyr}$ than for $t_d \lesssim 0.1 \text{ Gyr}$ for hBH2s.

These features can be clues to identify Pop. III hBH1s and hBH2s. Since the Pop. III formation epoch is much earlier than those of NSCs, GCs, OCs, TC/QCs, and Pop. I/II binaries, the Pop. III BH mass evolves earlier.

We summarize this section. The time evolution of the merger rate densities of hBH0s, hBH1s, and hBH2s can be a clue to identify Pop. III BH-BHs. If Pop. III BH-BHs are dominant, the BH-BH merger rate density keeps $\Gamma \propto t_d^{-1}$ beyond $z \sim 2$ regardless of initial conditions and stellar models. For an ideal condition (i.e. the optiq0.0a1e1 model), the time evolution of BH mass distributions can be clues to identify Pop. III BH-BHs. Pop. III hBH0s have lBHs with larger mass for larger t_d , and with high spin ~ 1 . The maximum $m_{b,p}$ mass of Pop. III hBH1s and hBH2s evolves earlier than those of other scenarios. No other scenario has suggested such time evolution.

5. DISCUSSION

5.1. Chemically homogeneous Pop. III stars

So far, we assume that Pop. III stars have small stellar rotations at their ZAMS times. However, they can have large stellar rotations. In fact, poloidal magnetic field around Pop. III stars is weaker than the turbulent field and toroidal field (Sharda et al. 2020). Thus the magnetic braking effect to spin down the protostar could be inefficient. Furthermore, the abundant Nitrogen in EMP stars suggests that the Pop III stars are fast rotators (e.g. Choplin et al. 2019). If they have large stellar rotations at their ZAMS times, they can switch on CHEs (e.g. Yoon et al. 2012, for Pop. III stars). Here, we make two simple models for Pop. III binary evolutions under CHEs, and estimate BH-BH merger rates. In the first model, we assume that a whole star evolves to a nHe star without stellar wind mass loss, and that a binary does not change its orbit without any interactions, such as tidal interaction, mass transfer and common envelope. The assumption of no binary interaction can be justified by the fact that the stars enter into CHEs due to their initial rotations (not due to tidal spinup), and do not expand so much. Such a resulting nHe star experiences supernovae and PPI/PISN described in section 2.1, and leaves NS, BH, or no remnant. Since a nHe star with $\lesssim 10M_\odot$ and $45 - 65M_\odot$ loses a part of its mass at supernova, the binary orbit should be changed. However, we ignore this effect for simplicity. In the second model, we assume that a star evolves to a nHe star, losing 30 % of its ZAMS mass due to stellar winds, which is roughly consistent with results of Yoon et al. (2012). We adiabatically change binary orbital parameters through the stellar winds so that the binary period is inversely proportional to square of the total mass, and the eccentric-

ity is constant. The nHe star experiences supernovae in the same way as the first model, and the supernovae do not change the binary orbital parameters.

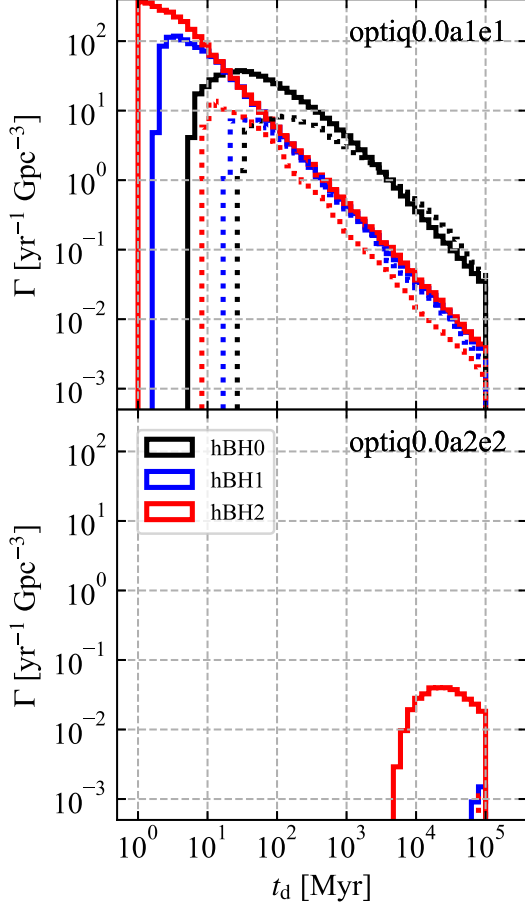


Figure 30. Merger rate densities of Pop. III hBH0s, hBH1s, and hBH2s as a function of t_d when all the Pop. III stars experience CHEs with initial conditions of the optiq0.0a1e1 and optiq0.0a2e2 models (the top and bottom panels, respectively). Solid and dashed curves indicate the first and second models, respectively.

Figure 30 shows merger rate densities of Pop. III hBH0s, hBH1s, and hBH2s as a function of t_d when all the Pop. III stars are CHEs. If $a_{\min} = 10R_{\odot}$, the hBH0, hBH1, and hBH2 merger rates for the CHE case are comparable to, or more than those for the non-CHE cases in the present-day universe ($t_d = 10 - 15$ Gyr). Since we ignore stellar mergers before stars collapse to BHs, we overestimate the merger rates for $t_d \lesssim 0.1$ Gyr.

However, binaries forming BH-BHs with $t_d \sim 10$ Gyr have much larger semi-major axes than nHe star radii, and thus they should not experience stellar mergers before their members collapse to BHs. Thus, the merger rates for $t_d \sim 10$ Gyr should be correct. If $a_{\min} = 200R_{\odot}$, hBH0s and hBH1s never merge at any time. If we take into account stellar wind mass loss, even hBH2s have no chance to merge for $t_d \leq 15$ Gyr. This shows that a_{\min} plays a crucial role if Pop. III stars have large stellar rotations, and enter into CHEs. Here, we stop discussing about CHEs. It is beyond of the scope of this paper to determine a_{\min} and whether Pop. III stars enter into CHEs or not.

5.2. Sensibility to λ_{CE}

We set $\lambda_{\text{CE}} = 1$ in section 3. However, λ_{CE} is quite uncertain, and Klencki et al. (2020) have shown λ_{CE} can be 0.01. For the optiq0.0a1e1 and optiq0.0a2e2 models, we change λ_{CE} to 0.1 and 0.01, and perform binary population synthesis calculations. Figure 31 shows their merger rate densities. We can find that λ_{CE} has small effects on the merger rates of hBH0s and hBH2s in the optiq0.0a1e1 models (see also Figure 9). This is because a significant part of hBH0s and hBH2s in these models are formed through the CE0 channel not involving common envelope evolution. On the other hand, hBH1s in all the models, and hBH0s and hBH2s in the optiq0.0a2e2 models are drastically decreased with λ_{CE} decreasing. This is because they are formed through channels involving common envelope evolution. Klencki et al. (2020) have also reported that common envelope evolution is harder to take place than previously thought, when a donor star is massive ($\geq 40M_{\odot}$), and a BSG star. If so, the dependence on λ_{CE} would become more strong.

5.3. BHs in the PI mass gap

In section 3, we obtain BHs in the PI mass gap, however their masses are at most $\sim 55M_{\odot}$. We examine initial conditions and single star models in which BHs with $\sim 80M_{\odot}$ emerge. Note that the possible maximum mass of BHs in the PI mass gap is $\sim 85M_{\odot}$ in our single star model (see Figure 3). We modify the optiq0.0a1e1 model, and prepare the following initial conditions. We extend the maximum semi-major axis from $2000R_{\odot}$ to 10^5R_{\odot} , and account for natal kicks with $\sigma_k = 50 \text{ km s}^{-1}$. We call this parameter set “PI-mass-gap” model.

Figure 32 shows merger rate densities of Pop. III BH-BHs as a function of t_d in the PI-mass-gap model. The merger rate densities of hBH0s, hBH1s, and hBH2s are similar to those in the optiq0.0a1e1 model (see black curves in the upper panels of Figure 9). We can find BH-BHs with BHs in the PI mass gap. Their merger

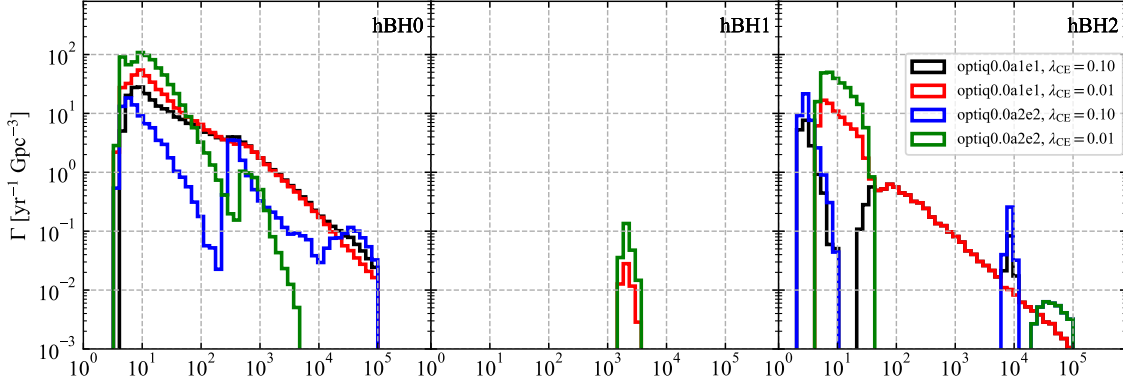


Figure 31. Merger rate densities of hBH0, hBH1, and hBH2 as a function of the delay time in the optiq0.0a1e1 and optiq0.0a2e2 models, where we set $\lambda_{\text{CE}} = 0.1$ and 0.01 . The left, middle, and right panels indicate the merger rate densities of hBH0s, hBH1s, and hBH2s, respectively.

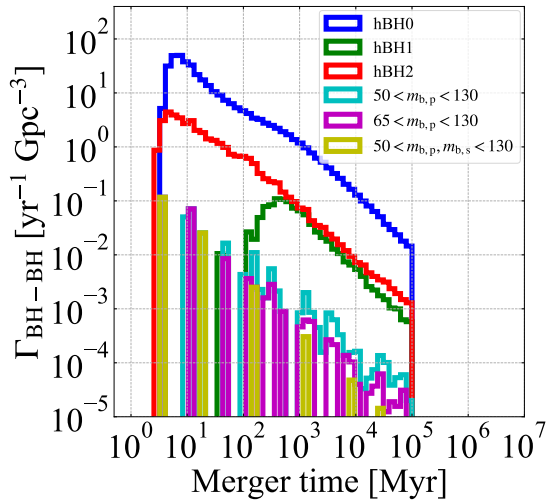


Figure 32. Merger rate densities of Pop. III BH-BHs as a function of t_d in the PI-mass-gap model. Here, the maximum mass of 1BHs is defined as $50M_\odot$, and the minimum mass of hBHs is defined as $130M_\odot$.

rate densities of $m_{b,p} > 50M_\odot$ and $m_{b,p} > 65M_\odot$ are $\sim 10^{-4} \text{ yr}^{-1} \text{ Gpc}^{-3}$ for $t_d = 10 \text{ Gyr}$. Even Pop. III BH-BHs with two BHs in the PI mass gap are present, although their merger rate is quite small. Among the main 16 model, the kickq0.9a2e2 model has the most BH-BHs with BHs in the PI mass gap. The merger rate density of $m_{b,p} > 50M_\odot$ is comparable to that of the PI-mass-gap model. On the other hand, the merger rate density of $m_{b,p} > 65M_\odot$ is much smaller than that of the PI-mass-gap model. Actually, the number of the BH-BHs is too small to calculate the merger rate density. In contrast to the main 16 models, the PI-mass-gap model can have plenty of BH-BHs with BHs in the PI mass gap ranging from $50M_\odot$ to $85M_\odot$.

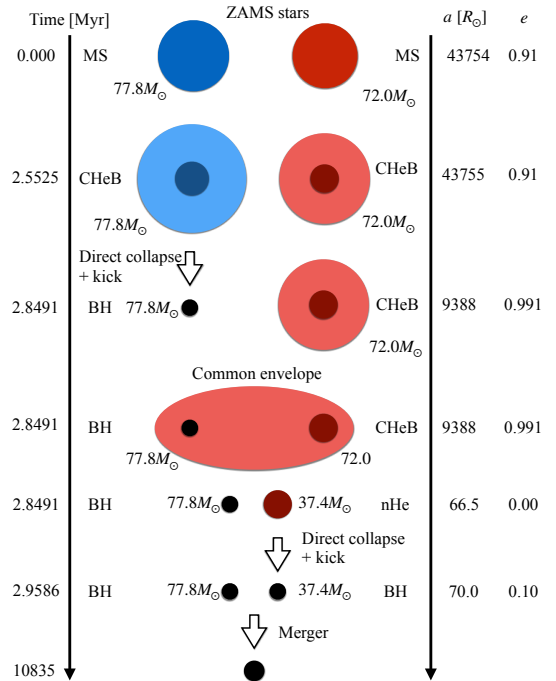


Figure 33. Example binary evolution leading to a BH-BH containing a BH in the PI mass gap.

We draw a schematic picture of a formation channel for BH-BHs with BHs in the PI mass gap in Figure 33. There are two key points. First, the two stars do not fill their Roche lobes until the 1st-evolving star collapses to the 1st BH. Thus, the 1st-evolving star keeps its H envelope, avoids PPI/PISN effects owing to its small He core with $< 45M_\odot$, and leaves a BH in the PI mass gap (see also Figure 3). Note that the 1st-evolving star is mildly spun up by the tidal field of the 2nd-evolving star, however it loses little mass even if we consider rotationally enhanced stellar winds. Second, a natal kick exerted on the 1st BH makes the binary eccentricity ex-

tremely high (~ 0.99), since the natal kick velocity is comparable to the orbital velocity of the binary. Then, the 2nd-evolving star expands, touches the 1st BH, and drives common envelope evolution. These two points finally make compact BH-BHs.

The PI-mass-gap model can form BH-BHs whose masses are similar to GW 190521's masses. However, their merger rate density of $\sim 10^{-4} \text{ yr}^{-1} \text{ Gpc}^{-3}$ is much smaller than GW 190521-like one $\sim 10^{-1} \text{ yr}^{-1} \text{ Gpc}^{-3}$ (Abbott et al. 2020b). If we increase the total Pop. III mass density in the local universe by 3 orders of magnitude, we can match their merger rate density with the observed one. However, as a side effect, the merger rate densities of hBH0s, hBH1s, and hBH2s are also increased to $\sim 10^2$, ~ 10 , and $\sim 10 \text{ yr}^{-1} \text{ Gpc}^{-3}$. These are not consistent with the observed merger rate density of hBH0s, and the upper limit of the merger rate densities of hBH1s and hBH2s derived by María Ezquiaga & Holz (2020). We conclude that the PI-mass-gap model cannot explain GW 190521-like events.

5.4. Pop. III hierarchical triple and quadruple systems

Sugimura et al. (2020) have shown possibility that Pop. III stars can be usually born as stable multiple systems. There may be many interesting respects in stable multiple systems: the formation of BHs in the PI mass gap (Fragione et al. 2020; Tanikawa et al. 2020a), excitation of binary eccentricity through Kozai-Lidov mechanism (Kozai 1962; Lidov 1962), and so on. However, initial conditions of Pop. III multiple systems are much less clear than those of binary stars. We will study Pop. III multiple systems as GW sources in future.

6. SUMMARY

We perform binary population synthesis calculations to obtain the merger rate density of Pop. III BH-BHs by means of the BSE code with extensions to very massive Pop. III stars. Our BSE code has several novel features. The extensions enable us to follow Pop. III stars up to $300M_{\odot}$, which include stars overcoming PISN and leaving BHs above the PI mass gap. We take into account PPI/PISN effects for binary population synthesis of Pop. III stars. We implement rotationally enhanced stellar wind into our BSE code. In our BSE code, natal kicks tilt BH spin vectors from binary orbit vectors, and the angles can be recorded. We use our BSE code, and investigate properties of Pop. III BH-BHs, and their dependence on single star models (natal kicks and stellar winds), and initial conditions (the minimum mass ratio q_{\min} and the minimum binary separation a_{\min} , see Section 2.3).

We can categorize Pop. III BH-BHs into three sub-populations: hBH0s, hBH1s, and hBH2s (see Figure 8).

This is because the PPI/PISN effects make the PI mass gap between $\sim 50 - 130M_{\odot}$. Provided that the mass density of Pop. III stars is $\sim 10^{13}M_{\odot} \text{ Gpc}^{-3}$, the merger rates of hBH0s and the sum of hBH1s and hBH2s are $\sim 0.1 \text{ yr}^{-1} \text{ Gpc}^{-3}$ and $\sim 0.01 \text{ yr}^{-1} \text{ Gpc}^{-3}$, respectively (see Figure 9). These merger rates are independent of single star models and initial conditions. Since Pop. III BH-BHs have several formation channels, initial conditions have small effects on their merger rates (see Figure 11). The natal kicks we adopt have velocities comparable to or smaller than internal velocities of Pop. III BH-BHs, and thus they do not affect much the merger rates. Pop. III stars lose their H envelopes through common envelope evolution as well as stellar winds. The presence of stellar winds has minor effects on Pop. III BH masses.

We summarize features of Pop. III hBH0s (see also Figures 14 and 15). The merger rate density of Pop. III hBH0s has the higher-mass ($\sim 45M_{\odot}$) and lower-mass ($\sim 20 - 35M_{\odot}$) peaks in the optiq0.0a1e1 model. The lower-mass peak shifts from $\sim 20M_{\odot}$ to $\sim 35M_{\odot}$ with t_d . Most of BHs in the lower-mass peak have high spins. Although the lower-mass peak is unique to Pop. III hBH0s, it is fragile against initial conditions and stellar evolution models. The characteristic feature of the lower-mass peak is that BHs around the peak have high spins if the peak is present.

Although their merger rate may be much smaller than inferred from the LIGO/Virgo observations, we could identify Pop. III hBH0s from observed BH-BHs, in an ideal case where the initial conditions are similar to the optiq0.0a1e1 model. The clue is the lower-mass peak, and highly-spinning BHs around at the lower-mass peak. Future GW observatories may detect conclusive Pop. III BH-BHs, a group of BH-BHs with high spins, and with peaks which shift from light to heavy with t_d . The above discussions can be also seen in Section 4.1.1.

We describe characteristic features of Pop. III hBH1s and hBH2s weakly depending on initial conditions (q_{\min} and a_{\min}) and stellar evolution models (stellar winds and natal kicks) as seen in Figures 14 and 15. The rate ratio of Pop. III hBH2s to Pop. III hBH1s is $\gtrsim 0.1$. Both of Pop. III hBH1s and hBH2s have two features: (i) $m_{b,p} \gtrsim 130M_{\odot}$, and (ii) a high fraction of low effective spins ($\lesssim 0.2$).

Pop. III hBH1s and hBH2s can be discovered soon by the current GW observatories. The above features can be clues to identify Pop. III hBH1s and hBH2s from others. Future GW observatories should find their merger rates are clearly $\propto t_d^{-1}$ beyond redshift of ~ 2 if Pop. III hBH1s and hBH2s dominate BH-BHs in this mass range. We make detail discussions in Sections 4.1.2 and 4.2.

Pop. III BHs in the PI mass gap can merge if Pop. III binaries have initial semi-major axes of $\sim 10^4 R_\odot$, and BHs have natal kicks of $\sim 50 \text{ km s}^{-1}$ (see Figure 33). However, their merger rate is smaller than that of GW 190521-like BH-BHs inferred by GW observations by 3 orders of magnitude. If we match their merger rate with the observed merger rate of GW 190521-like BH-BHs, the total merger rate of Pop. III BH-BHs exceeds the total merger rate of observed BH-BHs. Thus, this formation process is not appropriate for the formation of GW 190521-like BH-BHs.

In the worst scenario, the merger rates of Pop. III hBH0s, hBH1s, and hBH2s can be nearly zero (see Figure 30). The worst scenario is realized if the two following conditions are satisfied at the same time. First, Pop. III stars form only wide binaries with separations of $\gtrsim 100 R_\odot$, which is plausible, since Pop. III stars expand to $\sim 100 R_\odot$ in their protostellar phases. Second, Pop. III stars have enough fast rotations to excite CHes from the beginning time, which is supported by the theoretical study of Pop III star formation as well as the observation of EMP stars. In order to assess whether

these conditions are satisfied, or not, we need extremely high-resolution and long-term hydrodynamical simulation of Pop. III star formation. Such simulations should consider chemical evolution, radiative transfer, magnetic fields, and so on, and would be computationally prohibitive at the current state. We expect that computational technology rapidly evolves to achieve the above simulations, or that conclusive detections of Pop. III BH-BHs conversely rule out the worst scenario.

Aside from the worst scenario, we can expect that Pop. III hBH1s and hBH2s can be detected within a few years. Conversely, the non-detection would mean that the number of Pop. III stars overcoming PISNe is quite small. Thus, we may constrain the Pop. III IMF in the mass range $\gtrsim 100 M_\odot$ in the near future.

We thank the anonymous referee for helpful comments. AT thanks Tilman Hartwig and Christopher Berry for fruitful discussions. This research has been supported by Grants-in-Aid for Scientific Research (17H01101, 17H01130, 17H02869, 17H06360, 17K05380, 19K03907) from the Japan Society for the Promotion of Science.

REFERENCES

- Abbott, B. P., Abbott, R., Abbott, T. D., et al. 2016, *Physical Review Letters*, 116, 061102
- . 2019, *Physical Review X*, 9, 031040
- Abbott, R., Abbott, T. D., Abraham, S., et al. 2020a, *PhRvD*, 102, 043015
- . 2020b, *PhRvL*, 125, 101102
- . 2020c, *ApJL*, 896, L44
- . 2020d, arXiv e-prints, arXiv:2010.14527
- Abdul-Masih, M., Banyard, G., Bodensteiner, J., et al. 2020, *Nature*, 580, E11
- Abel, T., Bryan, G. L., & Norman, M. L. 2002, *Science*, 295, 93
- Amaro-Seoane, P., Audley, H., Babak, S., et al. 2017, arXiv e-prints, arXiv:1702.00786
- Antonini, F., Murray, N., & Mikkola, S. 2014, *ApJ*, 781, 45
- Antonini, F., & Perets, H. B. 2012, *ApJ*, 757, 27
- Antonini, F., & Rasio, F. A. 2016, *ApJ*, 831, 187
- Antonini, F., Toonen, S., & Hamers, A. S. 2017, *ApJ*, 841, 77
- Arca Sedda, M. 2020, *ApJ*, 891, 47
- Arimoto, M., Asada, H., & Cherry, M. e. 2020
- Askar, A., Szkudlarek, M., Gondek-Rosińska, D., Giersz, M., & Bulik, T. 2017, *MNRAS*, 464, L36
- Bae, Y.-B., Kim, C., & Lee, H. M. 2014, *MNRAS*, 440, 2714
- Banerjee, S. 2017, *MNRAS*, 467, 524
- . 2018a, *MNRAS*, 473, 909
- . 2018b, *MNRAS*, 481, 5123
- . 2019, arXiv e-prints, arXiv:1912.06022
- Barkat, Z., Rakavy, G., & Sack, N. 1967, *PhRvL*, 18, 379
- Barkov, M. V., & Komissarov, S. S. 2010, *MNRAS*, 401, 1644
- Bartos, I., Kocsis, B., Haiman, Z., & Márka, S. 2017, *ApJ*, 835, 165
- Batta, A., & Ramirez-Ruiz, E. 2019, arXiv e-prints, arXiv:1904.04835
- Belczynski, K., & Banerjee, S. 2020, *A&A*, 640, L20
- Belczynski, K., Bulik, T., Fryer, C. L., et al. 2010, *ApJ*, 714, 1217
- Belczynski, K., Bulik, T., & Rudak, B. 2004, *ApJL*, 608, L45
- Belczynski, K., Buonanno, A., Cantiello, M., et al. 2014, *ApJ*, 789, 120
- Belczynski, K., Holz, D. E., Bulik, T., & O’Shaughnessy, R. 2016a, *Nature*, 534, 512
- Belczynski, K., Kalogera, V., & Bulik, T. 2002, *ApJ*, 572, 407
- Belczynski, K., Ryu, T., Perna, R., et al. 2017, *MNRAS*, 471, 4702
- Belczynski, K., Heger, A., Gladysz, W., et al. 2016b, *A&A*, 594, A97

- Belczynski, K., Klencki, J., Fields, C. E., et al. 2020a, *A&A*, 636, A104
- Belczynski, K., Hirschi, R., Kaiser, E. A., et al. 2020b, *ApJ*, 890, 113
- Bethe, H. A., & Brown, G. E. 1998, *ApJ*, 506, 780
- Bodensteiner, J., Shenar, T., Mahy, L., et al. 2020, *A&A*, 641, A43
- Bond, J. R., Arnett, W. D., & Carr, B. J. 1984, *ApJ*, 280, 825
- Bondi, H., & Hoyle, F. 1944, *MNRAS*, 104, 273
- Bromm, V. 2013, *Reports on Progress in Physics*, 76, 112901
- Bromm, V., & Larson, R. B. 2004, *ARA&A*, 42, 79
- Callister, T. A., Farr, W. M., & Renzo, M. 2020, *arXiv e-prints*, arXiv:2011.09570
- Cameron, A. G. W., & Mock, M. 1967, *Nature*, 215, 464
- Casares, J., Jonker, P. G., & Israelian, G. 2017, *X-Ray Binaries*, ed. A. W. Alsabti & P. Murdin, 1499
- Chiaki, G., Yoshida, N., & Hirano, S. 2016, *MNRAS*, 463, 2781
- Choplin, A., Tominaga, N., & Ishigaki, M. N. 2019, *A&A*, 632, A62
- Clark, P. C., Glover, S. C. O., Klessen, R. S., & Bromm, V. 2011a, *ApJ*, 727, 110
- Clark, P. C., Glover, S. C. O., Smith, R. J., et al. 2011b, *Science*, 331, 1040
- Dayal, P., & Ferrara, A. 2018, *PhR*, 780, 1
- de Mink, S. E., Cantiello, M., Langer, N., et al. 2009, *A&A*, 497, 243
- de Souza, R. S., Yoshida, N., & Ioka, K. 2011, *A&A*, 533, A32
- Di Carlo, U. N., Giacobbo, N., Mapelli, M., et al. 2019, *MNRAS*, 487, 2947
- Di Carlo, U. N., Mapelli, M., Bouffanais, Y., et al. 2020a, *MNRAS*, 497, 1043
- Di Carlo, U. N., Mapelli, M., Giacobbo, N., et al. 2020b, *MNRAS*, 498, 495
- Dominik, M., Belczynski, K., Fryer, C., et al. 2012, *ApJ*, 759, 52
- . 2013, *ApJ*, 779, 72
- Downing, J. M. B., Benacquista, M. J., Giersz, M., & Spurzem, R. 2010, *MNRAS*, 407, 1946
- du Buisson, L., Marchant, P., Podsiadlowski, P., et al. 2020, *MNRAS*, 499, 5941
- El-Badry, K., & Quataert, E. 2020a, *arXiv e-prints*, arXiv:2006.11974
- . 2020b, *MNRAS*, 493, L22
- El Eid, M. F., & Langer, N. 1986, *A&A*, 167, 274
- Eldridge, J. J., & Stanway, E. R. 2016, *MNRAS*, 462, 3302
- Eldridge, J. J., Stanway, E. R., Breivik, K., et al. 2020, *MNRAS*, 495, 2786
- Eldridge, J. J., Stanway, E. R., & Tang, P. N. 2019, *MNRAS*, 482, 870
- Eldridge, J. J., Stanway, E. R., Xiao, L., et al. 2017, *PASA*, 34, e058
- Farrell, E. J., Groh, J. H., Hirschi, R., et al. 2020, *MNRAS*, arXiv:2009.06585
- Fishbach, M., & Holz, D. E. 2020, *ApJL*, 904, L26
- Fragione, G., & Kocsis, B. 2019, *MNRAS*, 486, 4781
- Fragione, G., Loeb, A., & Rasio, F. A. 2020, *ApJL*, 895, L15
- Fraley, G. S. 1968, *Ap&SS*, 2, 96
- Frebel, A., & Norris, J. E. 2015, *ARA&A*, 53, 631
- Fryer, C. L., Belczynski, K., Wiktorowicz, G., et al. 2012, *ApJ*, 749, 91
- Fryer, C. L., Woosley, S. E., & Heger, A. 2001, *ApJ*, 550, 372
- Fujii, M. S., Tanikawa, A., & Makino, J. 2017, *PASJ*, 69, 94
- Gandhi, P., Rao, A., Charles, P. A., et al. 2020, *MNRAS*, 496, L22
- Gandhi, P., Rao, A., Johnson, M. A. C., Paice, J. A., & Maccarone, T. J. 2019, *MNRAS*, 485, 2642
- Giacobbo, N., & Mapelli, M. 2018, *MNRAS*, 480, 2011
- Giacobbo, N., Mapelli, M., & Spera, M. 2018, *MNRAS*, 474, 2959
- Greif, T. H., Bromm, V., Clark, P. C., et al. 2012, *MNRAS*, 424, 399
- Greif, T. H., Springel, V., White, S. D. M., et al. 2011, *ApJ*, 737, 75
- Groh, J. H., Farrell, E. J., Meynet, G., et al. 2020, *ApJ*, 900, 98
- Hamann, W. R., & Koesterke, L. 1998, *A&A*, 335, 1003
- Hamers, A. S., Bar-Or, B., Petrovich, C., & Antonini, F. 2018, *ApJ*, 865, 2
- Hamers, A. S., & Safarzadeh, M. 2020, *ApJ*, 898, 99
- Hartwig, T., Volonteri, M., Bromm, V., et al. 2016, *MNRAS*, 460, L74
- Heger, A., & Woosley, S. E. 2002, *ApJ*, 567, 532
- Hirano, S., Hosokawa, T., Yoshida, N., Omukai, K., & Yorke, H. W. 2015, *MNRAS*, 448, 568
- Hirano, S., Hosokawa, T., Yoshida, N., et al. 2014, *ApJ*, 781, 60
- Hoang, B.-M., Naoz, S., Kocsis, B., Rasio, F. A., & Dosopoulou, F. 2018, *ApJ*, 856, 140
- Hobbs, G., Lorimer, D. R., Lyne, A. G., & Kramer, M. 2005, *MNRAS*, 360, 974
- Hong, J., Askar, A., Giersz, M., Hypki, A., & Yoon, S.-J. 2020, *MNRAS*, 498, 4287
- Hong, J., Vesperini, E., Askar, A., et al. 2018, *MNRAS*, 480, 5645

- Hosokawa, T., Omukai, K., Yoshida, N., & Yorke, H. W. 2011, *Science*, 334, 1250
- Hotokezaka, K., & Piran, T. 2017, *ApJ*, 842, 111
- Humphreys, R. M., & Davidson, K. 1994, *PASP*, 106, 1025
- Hurley, J. R., Pols, O. R., & Tout, C. A. 2000, *MNRAS*, 315, 543
- Hurley, J. R., Tout, C. A., & Pols, O. R. 2002, *MNRAS*, 329, 897
- Iben, I., J., & Renzini, A. 1983, *ARA&A*, 21, 271
- Inayoshi, K., Hirai, R., Kinugawa, T., & Hotokezaka, K. 2017, *MNRAS*, 468, 5020
- Inayoshi, K., Kashiyama, K., Visbal, E., & Haiman, Z. 2016, *MNRAS*, 461, 2722
- Irrgang, A., Geier, S., Kreuzer, S., Pelisoli, I., & Heber, U. 2020, *A&A*, 633, L5
- Kawamura, S., Nakamura, T., Ando, M., et al. 2006, *Classical and Quantum Gravity*, 23, S125
- Kimball, C., Talbot, C., Berry, C. P. L., et al. 2020, *ApJ*, 900, 177
- Kinugawa, T., Inayoshi, K., Hotokezaka, K., Nakauchi, D., & Nakamura, T. 2014, *MNRAS*, 442, 2963
- Kinugawa, T., Miyamoto, A., Kanda, N., & Nakamura, T. 2016a, *MNRAS*, 456, 1093
- Kinugawa, T., Nakamura, T., & Nakano, H. 2020a, *MNRAS*, 498, 3946
- . 2020b, *MNRAS*, arXiv:2009.06922
- . 2020c, arXiv e-prints, arXiv:2007.13343
- Kinugawa, T., Nakano, H., & Nakamura, T. 2016b, *Progress of Theoretical and Experimental Physics*, 2016, 103E01
- . 2016c, *Progress of Theoretical and Experimental Physics*, 2016, 031E01
- Kirihara, T., Tanikawa, A., & Ishiyama, T. 2019, *MNRAS*, 486, 5917
- Klencki, J., Nelemans, G., Istrate, A. G., & Chruslinska, M. 2020, arXiv e-prints, arXiv:2006.11286
- Komiya, Y., Suda, T., & Fujimoto, M. Y. 2015, *ApJL*, 808, L47
- Kozai, Y. 1962, *AJ*, 67, 591
- Kruckow, M. U., Tauris, T. M., Langer, N., Kramer, M., & Izzard, R. G. 2018, *MNRAS*, 481, 1908
- Kudritzki, R. P., Pauldrach, A., Puls, J., & Abbott, D. C. 1989, *A&A*, 219, 205
- Kudritzki, R. P., & Reimers, D. 1978, *A&A*, 70, 227
- Kumamoto, J., Fujii, M. S., & Tanikawa, A. 2019, *MNRAS*, 486, 3942
- . 2020, *MNRAS*, 495, 4268
- Kushnir, D., Zaldarriaga, M., Kollmeier, J. A., & Waldman, R. 2016, *MNRAS*, 462, 844
- Leigh, N. W. C., Geller, A. M., McKernan, B., et al. 2018, *MNRAS*, 474, 5672
- Leung, S.-C., Nomoto, K., & Blinnikov, S. 2019, *ApJ*, 887, 72
- Lidov, M. L. 1962, *Planet. Space Sci.*, 9, 719
- Liu, B., & Bromm, V. 2020a, *MNRAS*, 495, 2475
- . 2020b, *ApJL*, 903, L40
- Liu, B., & Lai, D. 2019, *MNRAS*, 483, 4060
- Liu, B., Meynet, G., & Bromm, V. 2020a, *MNRAS*, arXiv:2010.05824
- Liu, J., Zhang, H., Howard, A. W., et al. 2019, *Nature*, 575, 618
- Liu, J., Zheng, Z., Soria, R., et al. 2020b, *ApJ*, 900, 42
- Machida, M. N., & Doi, K. 2013, *MNRAS*, 435, 3283
- Machida, M. N., Omukai, K., Matsumoto, T., & Inutsuka, S.-i. 2008, *ApJ*, 677, 813
- Madau, P., & Dickinson, M. 2014, *ARA&A*, 52, 415
- Magg, M., Hartwig, T., Agarwal, B., et al. 2018, *MNRAS*, 473, 5308
- Magg, M., Hartwig, T., Glover, S. C. O., Klessen, R. S., & Whalen, D. J. 2016, *MNRAS*, 462, 3591
- Magg, M., Klessen, R. S., Glover, S. C. O., & Li, H. 2019, *MNRAS*, 487, 486
- Maggiore, M., Van Den Broeck, C., Bartolo, N., et al. 2020, *JCAP*, 2020, 050
- Mandel, I. 2016, *MNRAS*, 456, 578
- Mandel, I., & de Mink, S. E. 2016, *MNRAS*, 458, 2634
- Mangiagli, A., Bonetti, M., Sesana, A., & Colpi, M. 2019, *ApJL*, 883, L27
- Mapelli, M. 2016, *MNRAS*, 459, 3432
- Mapelli, M., & Giacobbo, N. 2018, *MNRAS*, 479, 4391
- Mapelli, M., Giacobbo, N., Ripamonti, E., & Spera, M. 2017, *MNRAS*, 472, 2422
- Mapelli, M., Giacobbo, N., Santoliquido, F., & Artale, M. C. 2019, *MNRAS*, 487, 2
- Mapelli, M., Santoliquido, F., Bouffanais, Y., et al. 2020, arXiv e-prints, arXiv:2007.15022
- Marchant, P., Langer, N., Podsiadlowski, P., Tauris, T. M., & Moriya, T. J. 2016, *A&A*, 588, A50
- María Ezquiaga, J., & Holz, D. E. 2020, arXiv e-prints, arXiv:2006.02211
- Marigo, P., Girardi, L., Chiosi, C., & Wood, P. R. 2001, *A&A*, 371, 152
- McKernan, B., Ford, K. E. S., & O’Shaughnessy, R. 2020, *MNRAS*, 498, 4088
- McKernan, B., Ford, K. E. S., Bellovary, J., et al. 2018, *ApJ*, 866, 66
- Mennekens, N., & Vanbeveren, D. 2014, *A&A*, 564, A134
- Nakamura, F., & Umemura, M. 2001, *ApJ*, 548, 19
- Nakamura, T., Ando, M., Kinugawa, T., et al. 2016, *Progress of Theoretical and Experimental Physics*, 2016, 093E01

- Nieuwenhuijzen, H., & de Jager, C. 1990, *A&A*, 231, 134
- Nitz, A. H., & Capano, C. D. 2020, arXiv e-prints, arXiv:2010.12558
- O’Leary, R. M., Kocsis, B., & Loeb, A. 2009, *MNRAS*, 395, 2127
- Olejak, A., Fishbach, M., Belczynski, K., et al. 2020, *ApJL*, 901, L39
- Omukai, K., & Nishi, R. 1998, *ApJ*, 508, 141
- Omukai, K., & Palla, F. 2001, *ApJL*, 561, L55
- . 2003, *ApJ*, 589, 677
- Park, D., Kim, C., Lee, H. M., Bae, Y.-B., & Belczynski, K. 2017, *MNRAS*, 469, 4665
- Petrovich, C., & Antonini, F. 2017, *ApJ*, 846, 146
- Piran, Z., & Piran, T. 2020, *ApJ*, 892, 64
- Portegies Zwart, S. F., & McMillan, S. L. W. 2000, *ApJL*, 528, L17
- Punturo, M., Abernathy, M., Acernese, F., et al. 2010, *Classical and Quantum Gravity*, 27, 194002
- Rasskazov, A., & Kocsis, B. 2019, *ApJ*, 881, 20
- Rastello, S., Amaro-Seoane, P., Arca-Sedda, M., et al. 2019, *MNRAS*, 483, 1233
- Reitze, D., Adhikari, R. X., Ballmer, S., et al. 2019, in *BAAS*, Vol. 51, 35
- Repetto, S., Igoshev, A. P., & Nelemans, G. 2017, *MNRAS*, 467, 298
- Repetto, S., & Nelemans, G. 2015, *MNRAS*, 453, 3341
- Riley, J., Mandel, I., Marchant, P., et al. 2020, arXiv e-prints, arXiv:2010.00002
- Rodriguez, C. L., Amaro-Seoane, P., Chatterjee, S., et al. 2018a, *PhRvD*, 98, 123005
- Rodriguez, C. L., Amaro-Seoane, P., Chatterjee, S., & Rasio, F. A. 2018b, *PhRvL*, 120, 151101
- Rodriguez, C. L., & Antonini, F. 2018, *ApJ*, 863, 7
- Rodriguez, C. L., Chatterjee, S., & Rasio, F. A. 2016a, *PhRvD*, 93, 084029
- Rodriguez, C. L., Haster, C.-J., Chatterjee, S., Kalogera, V., & Rasio, F. A. 2016b, *ApJL*, 824, L8
- Rodriguez, C. L., Zevin, M., Amaro-Seoane, P., et al. 2019, *PhRvD*, 100, 043027
- Roupas, Z., & Kazanas, D. 2019, *A&A*, 632, L8
- Rydberg, C.-E., Zackrisson, E., Lundqvist, P., & Scott, P. 2013, *MNRAS*, 429, 3658
- Safarzadeh, M., & Haiman, Z. 2020, *ApJL*, 903, L21
- Safarzadeh, M., & Hotokezaka, K. 2020, *ApJL*, 897, L7
- Samsing, J. 2018, *PhRvD*, 97, 103014
- Samsing, J., Askar, A., & Giersz, M. 2018, *ApJ*, 855, 124
- Samsing, J., & Ramirez-Ruiz, E. 2017, *ApJL*, 840, L14
- Santoliquido, F., Mapelli, M., Bouffanais, Y., et al. 2020, *ApJ*, 898, 152
- Sasaki, M., Suyama, T., Tanaka, T., & Yokoyama, S. 2016, *Physical Review Letters*, 117, 061101
- Schauer, A. T. P., Drory, N., & Bromm, V. 2020, *ApJ*, 904, 145
- Sesana, A. 2016, *PhRvL*, 116, 231102
- Sesana, A., Gair, J., Mandel, I., & Vecchio, A. 2009, *ApJL*, 698, L129
- Sharda, P., Federrath, C., & Krumholz, M. R. 2020, *MNRAS*, 497, 336
- Silsbee, K., & Tremaine, S. 2017, *ApJ*, 836, 39
- Simón-Díaz, S., Maíz Apellániz, J., Lennon, D. J., et al. 2020, *A&A*, 634, L7
- Skinner, D., & Wise, J. H. 2020, *MNRAS*, 492, 4386
- Spera, M., Mapelli, M., & Bressan, A. 2015, *MNRAS*, 451, 4086
- Spera, M., Mapelli, M., Giacobbo, N., et al. 2019, *MNRAS*, 485, 889
- Stacy, A., Bromm, V., & Loeb, A. 2011, *MNRAS*, 413, 543
- Stacy, A., Greif, T. H., & Bromm, V. 2012, *MNRAS*, 422, 290
- Stahler, S. W., Palla, F., & Salpeter, E. E. 1986, *ApJ*, 302, 590
- Stevenson, S., Vigna-Gómez, A., Mandel, I., et al. 2017, *Nature Communications*, 8, 14906
- Stone, N. C., Metzger, B. D., & Haiman, Z. 2017, *MNRAS*, 464, 946
- Sugimura, K., Matsumoto, T., Hosokawa, T., Hirano, S., & Omukai, K. 2020, *ApJL*, 892, L14
- Susa, H. 2013, *ApJ*, 773, 185
- . 2019, *ApJ*, 877, 99
- Susa, H., Hasegawa, K., & Tominaga, N. 2014, *ApJ*, 792, 32
- Suzuki, T. K. 2018, *PASJ*, 70, 34
- Tagawa, H., Haiman, Z., Bartos, I., & Kocsis, B. 2020a, *ApJ*, 899, 26
- Tagawa, H., Haiman, Z., & Kocsis, B. 2020b, *ApJ*, 898, 25
- Takahashi, K., Sumiyoshi, K., Yamada, S., Umeda, H., & Yoshida, T. 2019, *ApJ*, 871, 153
- Takahashi, K., Yoshida, T., & Umeda, H. 2018, *ApJ*, 857, 111
- Takahashi, K., Yoshida, T., Umeda, H., Sumiyoshi, K., & Yamada, S. 2016, *MNRAS*, 456, 1320
- Tanaka, S. J., Chiaki, G., Tominaga, N., & Susa, H. 2017, *ApJ*, 844, 137
- Tanikawa, A. 2013, *MNRAS*, 435, 1358
- Tanikawa, A., Kinugawa, T., Kumamoto, J., & Fujii, M. S. 2020a, *PASJ*, 72, 39
- Tanikawa, A., Kinugawa, T., Yoshida, T., Hijikawa, K., & Umeda, H. 2020b, arXiv e-prints, arXiv:2010.07616
- Tanikawa, A., Suzuki, T. K., & Doi, Y. 2018, *PASJ*, 70, 80

- Tanikawa, A., Yoshida, T., Kinugawa, T., Takahashi, K., & Umeda, H. 2020c, MNRAS, 495, 4170
- Tarumi, Y., Hartwig, T., & Magg, M. 2020, ApJ, 897, 58
- The LIGO Scientific Collaboration, the Virgo Collaboration, Abbott, R., et al. 2020, arXiv e-prints, arXiv:2010.14533
- Tout, C. A., Aarseth, S. J., Pols, O. R., & Eggleton, P. P. 1997, MNRAS, 291, 732
- Trani, A. A., Spera, M., Leigh, N. W. C., & Fujii, M. S. 2019, ApJ, 885, 135
- Umeda, H., & Nomoto, K. 2002, ApJ, 565, 385
- VanLandingham, J. H., Miller, M. C., Hamilton, D. P., & Richardson, D. C. 2016, ApJ, 828, 77
- Vassiliadis, E., & Wood, P. R. 1993, ApJ, 413, 641
- Venumadhav, T., Zackay, B., Roulet, J., Dai, L., & Zaldarriaga, M. 2020, PhRvD, 101, 083030
- Vink, J. S., & de Koter, A. 2005, A&A, 442, 587
- Vink, J. S., de Koter, A., & Lamers, H. J. G. L. M. 2001, A&A, 369, 574
- Wang, C., Jia, K., & Li, X.-D. 2016, MNRAS, 457, 1015
- Webbink, R. F. 1984, ApJ, 277, 355
- Willems, B., Henninger, M., Levin, T., et al. 2005, ApJ, 625, 324
- Wong, T.-W., Valsecchi, F., Fragos, T., & Kalogera, V. 2012, ApJ, 747, 111
- Woosley, S. E. 2017, ApJ, 836, 244
- Woosley, S. E., Blinnikov, S., & Heger, A. 2007, Nature, 450, 390
- Yang, Y., Bartos, I., Haiman, Z., et al. 2019, ApJ, 876, 122
- Yoon, S. C., Dierks, A., & Langer, N. 2012, A&A, 542, A113
- Yoon, S. C., Woosley, S. E., & Langer, N. 2010, ApJ, 725, 940
- Yoshida, N., Omukai, K., & Hernquist, L. 2008, Science, 321, 669
- Yoshida, T., Takiwaki, T., Kotake, K., et al. 2019, ApJ, 881, 16
- Yoshida, T., Umeda, H., Maeda, K., & Ishii, T. 2016, MNRAS, 457, 351
- Yungelson, L. R., Kuranov, A. G., Postnov, K. A., & Kolesnikov, D. A. 2020, MNRAS, 496, L6
- Zackay, B., Dai, L., Venumadhav, T., Roulet, J., & Zaldarriaga, M. 2019, arXiv e-prints, arXiv:1910.09528
- Zevin, M., Berry, C. P. L., Coughlin, S., Chatziioannou, K., & Vitale, S. 2020, ApJL, 899, L17
- Ziosi, B. M., Mapelli, M., Branchesi, M., & Tormen, G. 2014, MNRAS, 441, 3703